Investigations into the links between the generation of X-rays in X-ray Computed Tomography and shifts in extracted areal surface texture parameters

Jonathan Stephen Slocombe

A thesis submitted to the University of Huddersfield as a partial fulfilment of the requirements for the degree of Doctor of Philosophy (PhD)

Statement on Copyright

List of Publications

Work from Chapter 3 on filament degradation was presented at the 19th euspen international conference in Bilbao under the title "The effects of X-ray computed tomography filament degradation on extracted areal surface data". The author was the primary author of the conference paper and was responsible for the gathering and processing of all CT data used.

Slocombe , J., Townsend, A., Addinall, K., & Blunt, L. (2019). The effects of x-ray computed tomography filament degradation on extracted areal surface texture data. European Society for Precision Engineering and Nanotechnology, Conference Proceedings - 19th International Conference and Exhibition, EUSPEN 2019 (pp. 346-349). Bilbao: euspen.

Work presented in Chapter 4 has been published in the international journal Surfaces Topography: Metrology and Properties Volume 10 Issue 1 "The effects of manual XCT focusing on extracted surface texture" The author was the primary author of this journal paper and was responsible for the data gathering and processing throughout the paper.

Slocombe, J., & Blunt, L. (2022). The effects of manual XCT focusing on extracted surface texture data. Surface Topography: Metrology and Properties.

Abstract

The discovery of X-rays revolutionised medical imaging, never before had a technique offered a method of non-invasively imaging the human body. X-ray computed tomography (XCT) built on this, allowing not only the imaging but the reconstruction of a scanned object into a 3D volume to be realised. For both fields the primary use in the formative years was medical imaging, for which the technologies were uniquely suited. Both however were also adopted as means of non-destructive evaluation (NDE) for engineering applications. This largely occurred for the same reasons the technologies thrived in the medical field. X-rays can be used to image the internal structure of objects without line of sight, due to their penetrative capabilities.

Both X-ray imaging and XCT are however not without drawback. Most obviously X-rays are a form of ionising radiation, this was unknown in the early years of using X-rays as a medical imaging tool and led to significant numbers of illness and fatality amongst the early pioneers. Another issue highlighted by early research into X-rays and XCT was the low resolution and long processing times. Whilst between the first X-ray to the first use of XCT these had both improved, the issues remain prevelant.

Today XCT has been adopted into a wide range of industrial engineering disciplines, including porosity analysis and metrology. Current research in these fields works to develop specialist methods and parameters to further advance XCT's usefulness as a tool for the non-destructive analysis. The use of XCT in fields such as metrology, has led to the need to establish traceability and an understanding of error sources in XCT. Traceability is the ability to trace measurements taken back to a pre-existing standard. For most metrology applications this standard is the meter. Current research has highlighted that extracted areal surface texture parameters show a level of variation not seen in other measurement methods.

This thesis investigates how instability in several key processes of the generation of X-rays may propagate through to extracted areal surface texture parameters taken using XCT. The filament is a key component in the generation of X-rays and a consumable that requires changing on a semi-regular basis to ensure continued function of the XCT. Responsible for the emission of electrons that are used to generate X-rays it is superheated to allow for thermionic emission to occur, this causes its degradation over time. Theoretically as the cross-sectional area of a part emitting electrons is altered so with the electron beam emitted. This is investigated with several studies assessing if a pattern could be established between the filament's age and extracted parameter results. It is shown that no pattern could be established though variation in extracted surface parameters is seen throughout the filament's life, with larger jumps present if the filament is changed.

The changing of a filament is a procedure after which the machine requires refocusing, this process is investigated, and it is shown that by refocusing the machine without changing the filament a similar variation to that noted after a filament change is achieved. To quantify this a method of measuring the focal spot of a XCT is required, several methods were considered and one selected as a base from which a novel method was developed. The novel method was developed to allow for the measurement of the focal spot alongside a surface artefact.

The method proved viable returning data in line with literature and existing methods. The thesis presents work showing the development of this method and its application in measuring both the machine's focal spot and a surface artefact simultaneously. Measured focal spot diameter is shown to shift and links to the variation noted in areal surface texture parameters are presented.

The work shown in this thesis was carried out to investigate how variables inherent to XCT propagate into extracted areal surface texture parameters, the methods developed are applicable to any cone

beam XCT with little alteration. Results presented show that users of cone beam XCT should take into consideration the effects of variation in the XCT process when performing non-destructive evaluation. The work also highlights the need for further work in developing XCT for surface metrology.

Table of Contents

List of figures

List of tables

Acknowledgements

Whilst a PhD is the culmination of a single person's work, mine would not have been possible without a number of people who have helped, supported and pushed me towards (and over) the finish line. Many thanks to Professor Liam Blunt who has guided me throughout my studies and without whom none of this would have been possible. I would also like to acknowledge the UK's Engineering and Physical Sciences Research Council (EPSRC) funding of the EPSRC Future Advanced Metrology Hub, The University of Huddersfield, and the Centre for Precision Technologies.

Karl, Joey, Hannah, Katie, and Chris, thank you for livening up the department and making lunch breaks a thing to look forward to. Without you all I don't think I would have made it through Covid which so rudely interrupted us all!

Thank you to all those who have put up with my stress during the final stages of my studies, especially the team at Venn St, who have had to been told far too much information on X-rays and surface metrology since we all started working together.

And finally, Michelle who after supporting me throughout my undergraduate degree decided she would be fine if I went back to university and did it all over again. You have looked after me (and all our pets) through a house move and a global pandemic, quite honestly, I'd be utterly lost without you.

1. Introduction

1.1. "On a new kind of ray"

From the first radiographs taken by Wilhelm Rontgen using a Crookes tube (Figure 1-1), the potential of X-rays as an analytical tool has been abundantly clear.
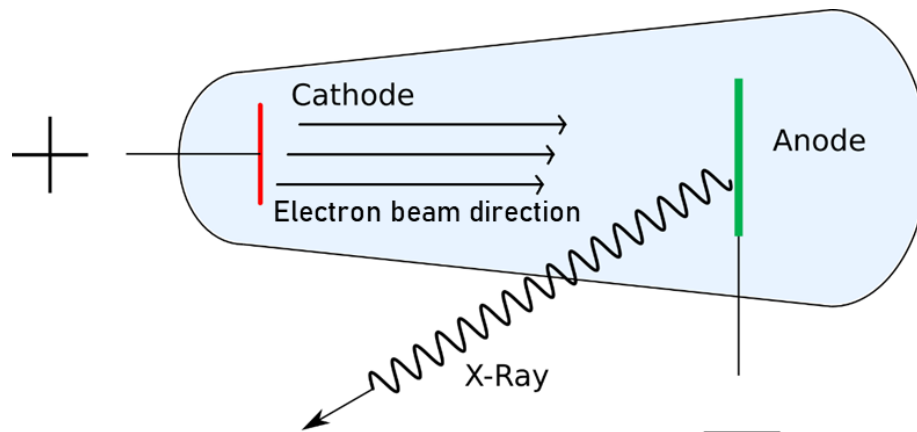
Figure 1-1 Basic functionality of a Crookes tube, as used by Rontgen during his discovery

Prior to December 1895 scientists had no way to "non-destructively" analyse an object that could not be seen in the detail Rontgen's discovery allowed. Though it can be argued the first years of studying the new rays were anything but non-destructive given the lack of understanding of the medical effects of ionising radiation. Rontgen's work itself came about by accident, as he noted that when experimenting with barium platinocyanide coated paper held in a vacuum, it was observed that samples of the film not held within a vacuum some 2 meters away from the experiment location were seen to glow. Cathode rays were know to only travel short distances in air, with further experimentation Rontgen was able to confirm that the cathode tube was the source of the plates discolouration. Shortly after this, he produced the first X-ray of a human, producing the X-ray image of his wife's hand shown in Figure 1-2.
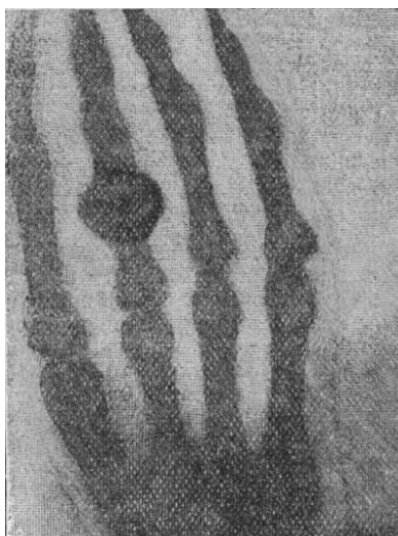
Figure 1-2 (left) The x ray image presented in the work of Rontgen (Roentgen, 1896) (right) Wilhelm Rontgen (British Institute of Radiology, 2022)

It is undoubtably true that Roentgen was not the first to produce X-rays under laboratory conditions, many of these early tubes were likely emitting X-rays and work published by Ukrainian-born physicist Ivan Pawlowich Puluj noted that photographic plates would blacken when exposed to his "Puluj's

tube", a form of Cathode ray tube (Mayba, Gaiua, Kyle, & Shampo, 1997). Roentgen was however the first to demonstrate an understanding of the new phenomena.

On January 1st 1896 Rontgen wrote to a selection of his colleagues to inform them of his discovery, his paper "On a new kind of rays" clearly shows that he believed that the new rays were of significant scientific interest. Over the following weeks and months developments were made at such a rate as has rarely been matched in any period of research history. In his published paper an afterword states that "Professor Roentgen's discovery brings to a close a most interesting chapter in the history of electricity" (Roentgen, 1896).

1.2. "A most interesting chapter in the history of electricity"

The "most interesting" period referred to above arguably starts with the discovery of thermionic emission, a key process in not only Roentgen's Crookes tube but in X-ray generation to this day. Thermionic emission is the process were by electrons are emitted from an electrically conductive material into a nonconductive free space, this was first noted by Alexandre-Edmond Becquerel in 1853 (Becquerel, 1853). Becquerel, a 2nd generation physicist whose family have gone on to have a rich history of published work had already been the first to observe the photovoltaic effect at age 19 (Becqurel, 1839). The work presented to the Academy of Sciences titled "*Research on the transmission of electricity through gases at high temperatures*", is accepted as the first know instance where thermionic emission was observed. Through all early work on the topic of thermionic emission the term electron is not used, though it was understood an emission was taking place, the electron was not identified until 1897 by J.J. Thomson (J.J.Thomson, 1897). Becquerel never expanded much on this discovery which allowed it to be independently "rediscovered" not once but twice, first by Frederick Guthrie in 1873 (Guthrie, 1873) and again more famously by Thomas Edison in 1880 who was investigating why the lamp filaments in his incandescent bulbs were failing. Upon returning from a trip to the United States during which time he observed a demonstration of thermionic emission by Thomas Edison, William Henry Preece began to work to "thresh out" the theory behind Edison's discovery. Using a collection of samples provided by Edison, Preece concluded that the Edison effect (Thermionic Emission) was a result of an arc between the carbon filament and the metal plate within the bulb. Preece erroneously assumed the arc was made of carbon particles in beam lines passing across the space from negative to positive (Preece, 1884). Upon reflection in later work by Sir Ambrose Fleming, who had worked as a consultant for the Edison Electric Light Company at the time of Preece's work, he stated that it was now understood the arc was made of negative electrons which were, as discussed, unknown at the time of Preece's experiments (Flemming, 1934). Fleming is credited with the invention of the thermionic valve, a key component in early radio, radar and telephone networks among others. The theory behind these valves uses the phenomenon of thermionic emission to function and they share a common ancestor withs the Crookes tube in the Geissler tube (Figure 1-3).

Figure 1-3 Geissler tubes of various designs, (Harrison, 2014)

Giessler tubes were an early vacuum tube that themselves were thought of nothing more than a novelty by most and were made in complex shapes and with a variety of colours.

The development of Crookes tubes from Geissler's original novelties and a more rounded understanding of Becquerels Thermionic emission were key Roentgen's discovery of the new waves.

1.3. X-rays

The new rays Roentgen had discovered he named X-strahl or X-rays due to their unknown nature, X-rays we now understand to be a form of electromagnetic radiation where the wavelength can vary from 10nm to 0.01nm. Their place in the electromagnetic spectrum can be seen in the Figure 1-4 below.
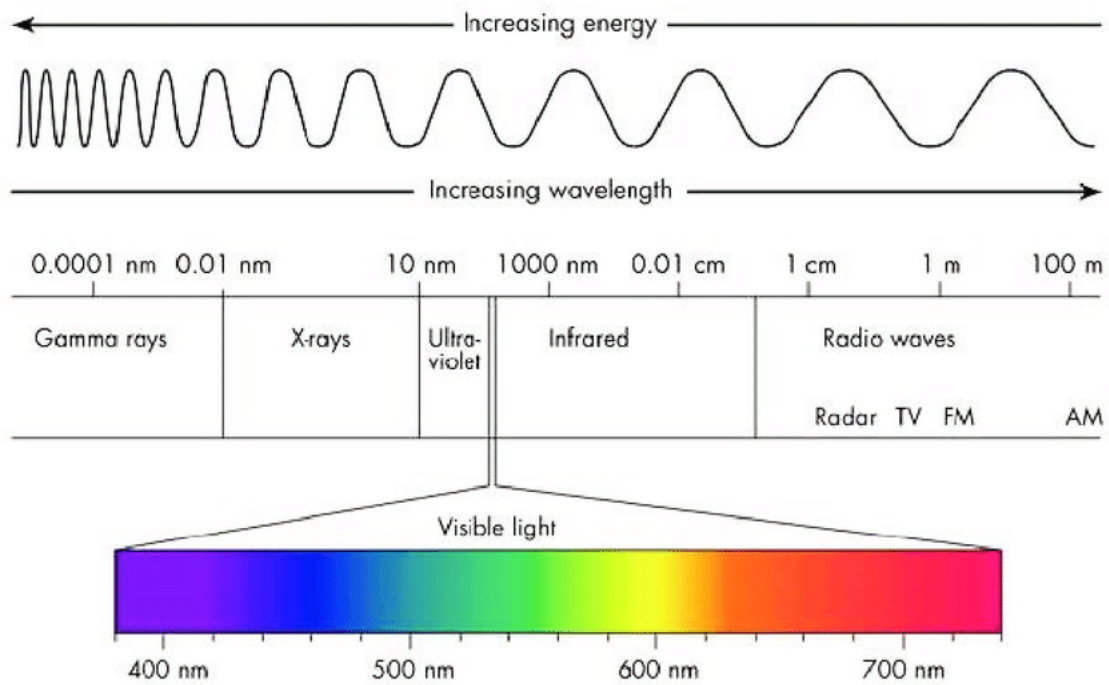
Figure 1-4 the electromagnetic spectrum as understood today. Taken from (Secades, O'Connor, Brown, & Walpole, 2014)

There are today several key understandings concerning X-rays that were not know to Rontgen, such as the fact that cathode rays are electron beams and the interactions of these rays with the target in the tube resulting in the production of his X-rays. There are now understood to be two common methods by which X-rays can be generated, characteristic X-ray emission and bremsstrahlung.

1.4. Characteristic x-ray emission

Characteristic emission occurs when upon an electrons collision with a target material, an excitation of ionic states results in an electron leaving the inner shell, the resultant void is quickly filled by an electron from an outer shell. The transition from outer to inner shell results in the emission of an X-ray photon. The energy of the emitted X-ray is equal to the difference in ionizing energies of the electrons involved in the transition. This process can be seen in Figure 1-5 (Microscopy Australia, 2014)
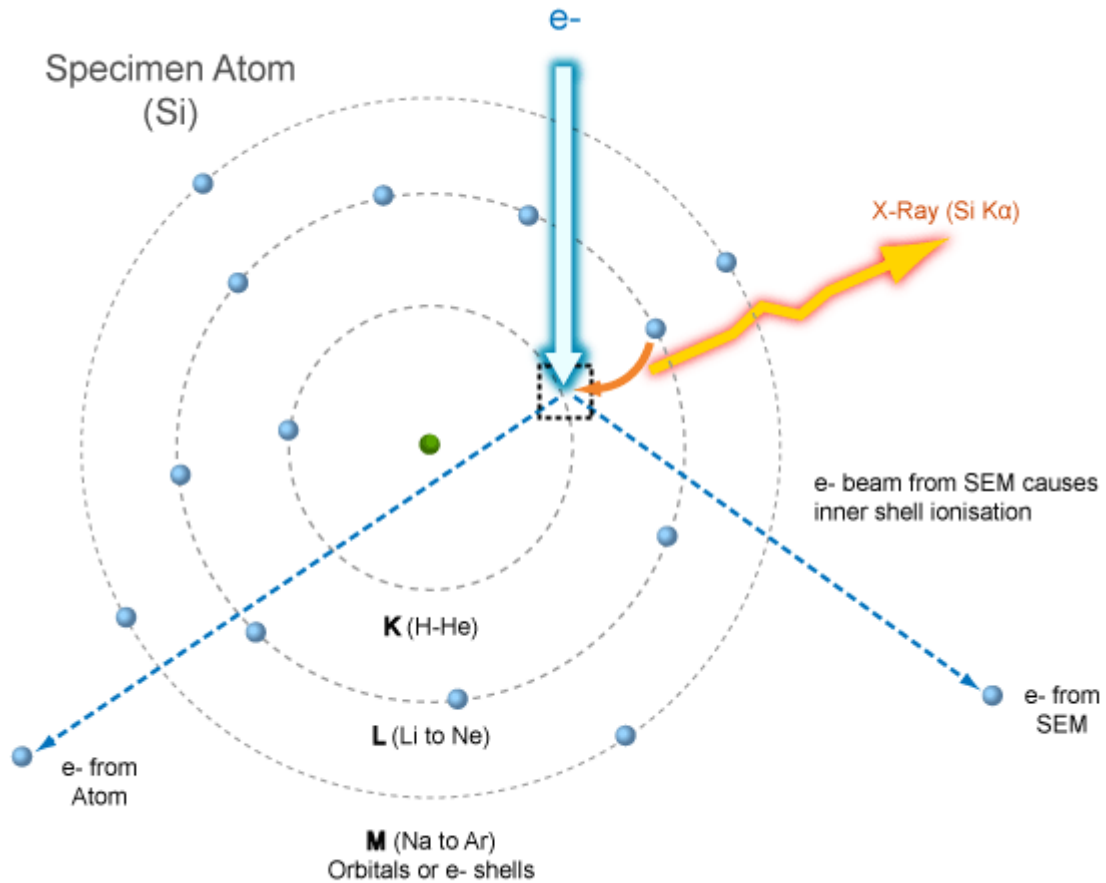
Figure 1-5 diagram showing the process of characteristic X-ray production (Microscopy Australia, 2014).

1.5. Bremsstrahlung

Bremsstrahlung X-rays are again caused by the interaction of electron beams with a target material, this form of X-ray radiation is however generated by a decelerating electron, this deceleration is due to its interaction with a target material. During this interaction where some of the energy lost by the electron whilst decelerating is converted into X-rays. As the energy of the x-rays is directly gained from the electron beam it is impossible for the X-rays to have a higher energy level than that of the primary electron beam. This limit is known as the Duane-Hunt limit (Microscopy Australia, 2014).

1.6. Processes resulting in X-ray attenuation

In early research, it was not only the generation of the newly discovered X-rays that was not understood but the interaction of the rays with the surrounding environment. These interactions are now better understood and are broken into several distinct interactions, coherent scattering, Compton scattering, pair production, the photoelectric effect and photodisintegration.

1.6.1. Coherent scattering

Sometimes also knowns as Thomson or Rayleigh scattering, Coherent Scattering is an effect where X-ray photons interact with and excite an entire atom of the they are subject passing through. The atom then releases an X-ray photon of identical wavelength to the incoming X-ray but in a different direction. (Miroslaw & Fournier, 2007)

1.6.2. Compton scattering

Compton scattering occurs when an X-ray photon interacts with an electron in the outer shell of the target material, which absorbs some of the photon's energy. An X-ray photon of the remaining energy is then scattered, exiting the nucleus in a random direction this process was first noted by Arthur Compton. (Compton, 1923)

1.6.3. Pair Production

In pair production, a high energy photon (E>1.02MeV) will interact not with an electron but the strong electric field surrounding the nucleus. The interaction leads to the photon undergoing a change of state resulting in the production of an electron and positron. The electron once emitted is quickly re absorbed however the positron combines with a neighbouring electron in a process known as annihilation radiation. This results in the two particles being converted into X-ray photons with traveling at 180 degrees to one another with energy equivalent to half that of the initial photon (Meroli, 2022).

1.6.4. Photoelectric effect

For the photoelectric effect, a photon interacts with an inner shell electron and is completely absorbed, resulting in an ionised atom. The higher the atomic number of the atom the higher energy X-ray can be absorbed. The electron is then emitted as a Photoelectron producing a characteristic X-ray. (Muibbullah & Ikuma, 2019)

1.7. Photodisintegration

This is the absorption of X-ray photons of particularly high energy levels by the nucleus resulting in the emission of a subatomic particle. This process similar to pair production, will only occur at higher energy levels (E>10MeV) (Clayton, 1983).

1.8. The rapid development of X-rays in medicine and imaging

Following the discovery of X-rays by Roentgen he wrote to scientific colleagues on Januarys 1st 1896 to inform them of his discovery, upon reflection it is clearly evident that the significance of the new rays was not lost on Roentgen as Becquerels observations of thermionic emission had been. With his writings he sent sample radiographs to showcase the new phenomena. On January 8th Alan Archibald Campbell-Swinton had replicated Roentgen's method and taken his own radiographs of a selection of random objects seen in Figure 1-6 (Mould, 2018).
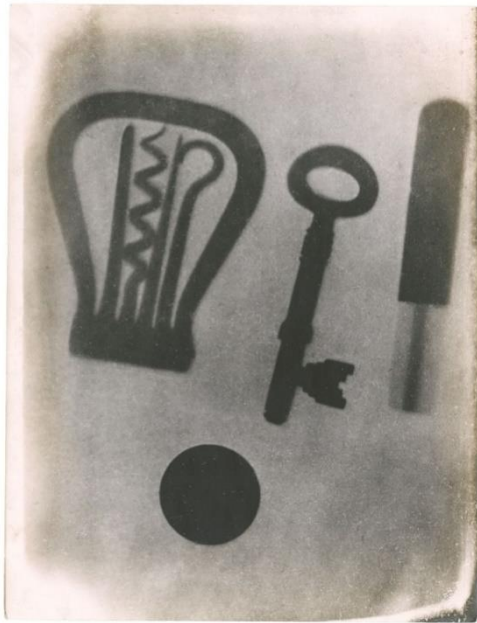
Figure 1-6 Early radiograph taken by Campbell-Swinton a selection of objects inside a calico pocket (Mould, 2018)

There was almost an immediate response from the medical community of the day, with the first radiograph taken under clinical conditions by John Hall-Edwards on January 11th, 1896, (Meggit, 2008). Soon after Gustav Kaiser and Eduard Haschek had taken the first medically indicated radiograph. The Radiograph of a hand showed damage to the patient's middle phalanx (Giacomuzzi, Springer, Stohr, & Schreder, 1998). By January 17th the first angiogram had been taken (European Society of Radiology, 2013) though this was taken post-mortem and the method would not become common until much later. Before the end of the month fluoroscopy, live imaging using X-rays, had been demonstrated by both Enrico Salvioni and Thomas Eddison (Otha W. Linton, 1995).

On January 23rd Roentgen gave a lecture on X-rays at the Würzburg Physical Medical Society which concluded with a demonstration X-ray of Prof. Albrecht von Kölliker the society president, who suggested the phenomena should be named Roentgen rays. The name given to them today was coined by Roentgen himself who designated the new rays X-Strahl due to the unknown nature of the rays.

By the end of the year X-rays were being used in medicine, specialised Crookes tubes developed specifically for X-ray generation were in mass production and patents were in place relating to developments of X-ray tubes (Glasser, 1993) (Russo, 2017). The rapid development of this new field of research through 1896 would continue for some years at a similar pace, as it seemed that the new rays had potential to be applicable across a range of scientific and engineering disciplines and this was not lost on the scientists of the time. It should be recognised that many of these early pioneers would

come to pay medically for their work, due to the lack of understanding of the effects of long periods of exposure to X-rays.

1.9. XCT a new kind of use

Roentgen's discovery led to the use of his X-rays in a range of fields and developments continued increasing the safety, speed and range of uses of the X-rays allowing pioneers such as Marie Curie to advance the field further and further. Radiographs however had limitation in that they were only 2D. Modern XCT (X-ray computed tomography) is the use of radiography allowing for the 3D mapping of objects, this is facilitated by stitching many individual radiograph images into a single 3D model using the intensity value of a given pixel to determine the edge of the object, various forms of data can then be taken from these models allowing for in-depth analysis of the original part.

Whilst a common procedure in medicine, XCT is now being used more frequently than ever in engineering as a method of non-destructive testing and whilst the infancy of this can be seen as far back as the early 1980's, new methods are being developed ever expanding the applications list of XCT (Reimers & Goebbels, 1983) (Townsend, Pagani, Scott, & Blunt, 2017). The penetrative nature of X-ray waves allows for internal or otherwise hidden details to be revealed without the need for destructive testing. Across a range of fields including non-destructive evaluation (Reimers & Goebbels, 1983), porosity analysis (Wevers, 2012) through to internal dimensional measurements (Chahid M. , et al., 2020), new techniques have been pioneered allowing engineers un-paralleled methods of evaluation and whilst XCT may not currently be able to compete with traditional methods in regards to traceability, its benefits are undeniable.

A recent development of note to the present study is the use of XCT to gather areal surface data from inaccessible locations, in line with existing standards ISO (International Standards Organisation). These methods, first published by Dr Andrew Townsend at the University of Huddersfield, have, when compared to areal measurements of the same additively manufactured surface been found to be within an acceptable degree of accuracy for most uses (Townsend, Pagani, Scott, & Blunt, 2017). This development further expands the known advantages of XCT over traditional metrology methods which require line of sight to or contact with the region of interest.

With any developing technology it is important not only to explore the benefits and new possible uses but to also measure and understand the limits of the process and any possible sources of inaccuracy, XCT technologies are no different in this. The core focus of the present research is to assess how errors at various points throughout the process of X-ray generation affect the extracted surface data gathered using the techniques pioneered by Townsend et al.

1.10.   Thesis Structure

The present thesis consists of 7 chapters and an appendix, chapter 1 is a brief introduction to the subject area. A summary of each subsequent chapter is included.

1.10.1. Chapter 2-Literature review

Chapter 2 is a review of current literature on the subject of XCT. The first section details the operating principles and functionality of XCT, including know error sources and user inputs. After this a discussion of the development of XCT as a tool of industry is carried out. The emergence of XCT for metrology both dimensional and surface is discussed, with advances in both fields analysed. Finally, a discussion of an investigation into the traceability and more in-depth discussion of errors is outlined to assess the use of XCT's as a metrology tool.

1.10.2. Chapter 3-The effects of variation and degradation of XCT emitter filaments

This chapter focuses on studies building on the work of Townsend et al, which showed that there was surface roughness variation when a filament change occurred. Townsend previously noted this variation, but further investigation into the cause was outside his study scope. The chapter covers work done to further investigate the noted phenomena. Investigations were carried out focusing on whether a pattern could be found when observing areal surface texture parameters extracted from XCT scans taken using different emitter filaments. Concurrently investigations were completed to observe the changes noted by Townsend were due to a drift in results that correlated with the degradation of the filament. The results of this work were presented at the 19th EUSPEN international conference. Investigations were also carried out into factors surrounding the filament such as its surface condition and material composition.

1.10.3. Chapter 4- The effects of manual focus variation on extracted areal surface texture parameters

The work presented in Chapter 3 led to the conclusion that the difference between a filament may not be due to the filament but its installation. Consequently, this chapter covers the subject of installation of the filament. During the time these investigations were carried out, several new methods of surface data extraction from XCT were developed, these are compared in this chapter. A repeatability study of the method selected for surface extraction going forward is carried out. The chapter covers the method used to alter machine focus, with results being compared to those given in Chapter 3. The work presented in this chapter was published in the international journal Surface Topography Metrology and Properties.

1.10.4. Chapter 5- Development of a novel method for measuring XCT focal spots

To quantify the possible link discovered in Chapter 4 a method of measurement of machine focus was required. Various existing methods of measuring an XCT focal spot are compared for benefits in this section. A novel method is outlined using an existing method as a starting point. The method is automated and proves to give comparable results to existing standards whilst considering a larger data range and removing a possible source of human error. The method also allows for the concurrent scans of a separate calibrated dimensional artefact to be taken.

1.10.5. Chapter 6- Investigating the link between focal spot dimensions and extracted surface texture parameters

Chapter 6 uses the procedure developed in the previous chapter to establish whether there is a direct correlation between focal spot geometry and extracted areal surface texture parameters taken using XCT.

1.10.6. Chapter 7-Conclusions

Chapter 7 Includes an overview of all studies completed and compares them against the original aims of the project. Each chapter's results are summarised with the significance of the results discussed. The major conclusions of the research are presented referencing the experimental results. The focus of future work in the field is discussed with future objectives being set

1.11. The Overall research aim restatement

The research aims of the present study is to demonstrate how uncontrolled variables in the process of X-ray generation for XCT may cause X-ray variation which propagates through to extracted surfaces and the areal surface texture parameters generated from them. Further to these correlations seen between identified variables and results should be further investigated as to establish possible methods of control or correction.

1.12.   Overall research objectives

The following objectives are the primary goals of the research project and the outcome of all the work described will be compared against the objectives at the conclusion of the work.

- Identify uncontrolled variables in X-ray generation for cone beam XCT reviewing current literature to identify possible unknown sources of variation.
- Separate the variables into logical groups allowing for the development of studies to investigate any effects on end results (areal surface texture parameters), where possible variables should be isolated, but it is accepted by the author this may not always be achieved.
- Design and develop test methods for each variable starting at the beginning of the X-ray generation process and working through to complete surface data results.
- Quantify, whether identified X-ray variables introduce shifts in surface parameter results that correlate with a measurable change in the variable, discussing where the variation introduced may prove significant.
- Where possible, identify and develop possible methods of controlling or correcting for error sources

2. Literature review-XCT

The 1979 Nobel prize in physiology or medicine was awarded to a pair of scientists, Allan M Cormack and Godfrey N Hounsfield. The award was given for the development of computer assisted tomography (Nobel Prize Outreach, 2022). A decade earlier Hounsfield had drafted a project proposal that would lead to the development of the modern XCT. This was based on the theoretical principle of how a computer program could recreate a matrix (Beckman, 2006). 3 years after the Hounsfield project proposal, the first clinical use of the XCT occurred, on 1st October 1971, when a scan was taken of a patient's frontal lobe, this first XCT scan can be seen in Figure 2-1. The operating surgeon was quoted as saying "it looks exactly like the picture". Whilst not adopted quite as rapidly as Roentgens discovery in the late 19th century The importance of Hounds fields work like Roentgens is undeniable.
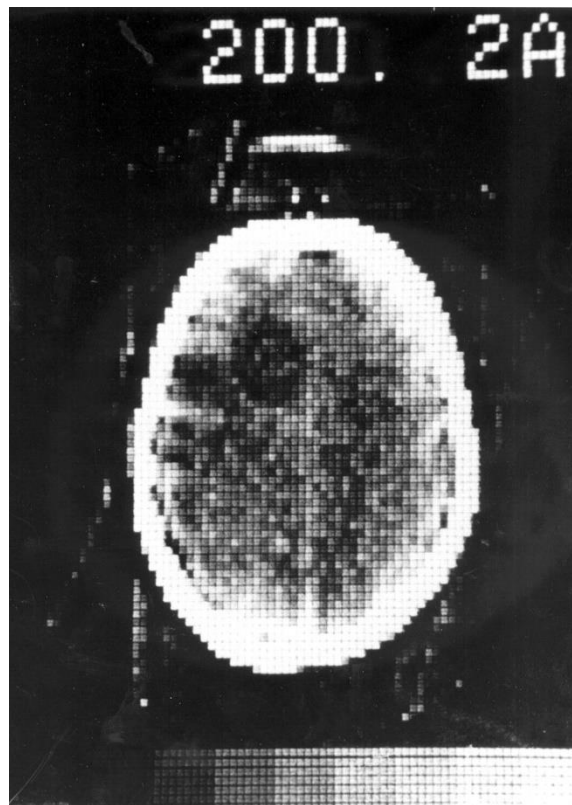
Figure 2-1 First clinical scan taken using Hounsfield's prototype EMI scanner. Taken from (Beckman, 2006)

Early scans such as that seen in Figure 2-1 were of an extremely low resolution, and processing times of the original EMI scanner were around 7 Minutes for a single slice (Beckman, 2006). Comparing the image above to those taken using a modern XCT such as the Nikon XT-H 225 with a minimum effective pixel size of 127 μm, it is clear how far the field has come. 50 years later XCT is not only an integral part of medical imaging but has also been adopted widely in many fields of engineering (Smith, Bills , Addinall, & Blunt, 2021) (Wells J. , 2009).

2.1. Early development of XCT for industrial application

The development of XCT as an industrial process for analysis began not long after the development of Hounsfield's medical imaging EMI, with some of the first imaging being completed by Sweeny at Lawrence Livermore labs in 1974 (Lawrence Livermore Labs, 1974). This early work was expanded upon by Kruger et. Al who in 1977, began a R&D program to expand XCT for non-medical applications (Kruger & Cannon, 1978). This early work was like that of Hounsfield still limited by pixel size, of which

approximately 1mm resolution could be achieved (Reimers, Gilboy, & Goebbels, 1984). Though it was found that features such as cracks of 100 μm could be imaged by lowering the attenuation in a pixel by enough that the grey level difference was noticeable. It was also in 1977 that Surrey University also began investigations into the industrial use of photon tomography. Starting with a medical scanner of the day, studies led to the development of a "tomographic scanning system for industrial applications" (Gilboy, Foster, & Folkard, 1982). Elliot et. al. reported on the use of X-ray tomography for the analysis of extremely small samples (Elliot & Dover, 1982). Elliot et. al.'s work observed a tropical freshwater snail using an X-ray beam 15 μm in diameter and a pixel size of 12x12 μm, this was achieved using a tube at 25 kV and 0.95 mA. The paper acknowledges that a limiting factor was the low power of X-ray sources available and states there would be a "great advantage in using a very much more powerful synchrotron source".

A summary of the application of X- and gamma ray tomography to non-destructive evaluation (NDE) from 1984 notes that current medical machines produce X-rays of insufficient power (~70keV) to adequality image high density material common in industrial applications. It goes on to discuss recent advances in medical imaging with machines using tube voltages more than 400kV. Not dissimilar to what would be considered a "high" power machine today (Gilboy W. , 1984). The paper expands to discuss practical limitations of the technology such as time and resolution. Whilst no doubt these have both improved in modern times, the limiting factors of XCT remain constant. It is also worth noting, that the resulting images taken using XCT is not only parameter but likely machine dependent. Though in recent years XCT has been shown to have consistency across machines by Townsend et al. who's interlaboratory study aimed to show consistency of measurement across multiple machines. (Townsend, Radu, Bills, & Blunt, 2017). This round robin study used machines based at four institutions to measure two artefacts' whilst able to show a level off repeatability this was reliant on the use of mathematical correction, highlighting that issues remain concerning the traceability and repeatability of the subject.

When observing the early application of XCT, it clear that its use as an analytical tool was clear from its conception. The adoption of XCT as a method of industrial non-destructive testing was relatively widespread from its introduction. This is demonstrated in Figure 2-2, which showcases a range of scans taken shortly after its adoption as a method of NDE.
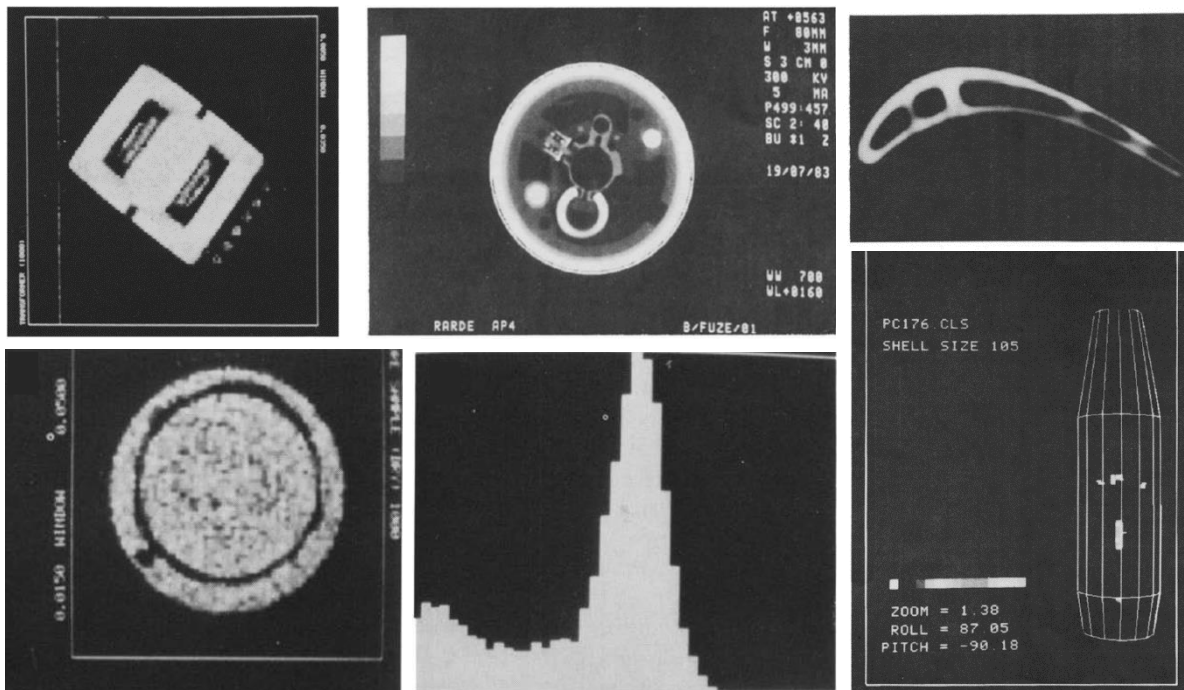
Figure 2-2 shows a range of fields that adopted early XCT tomography, (clockwise from top left) Mains adaptor, 50mm fuse housing, High temperature turbine blades, porosity analysis of a 105mm shell, histogram of simulated porous rock core seen in next image, Simulated porous rock core (Gilboy W. , 1984).

Only a few years after Hounsfield's work was it already being adopted for basic porosity and fracture analysis and whilst the development of quantifiable method of extraction of metrological data were still some ways away, like Roentgen's discovery in 1895, the adoption of the technology was rapid. Whilst greatly improved, the issues noted by the early adopters such as power, resolution and repeatability remain key areas of study in the current literature.

2.2. Modern X-ray functionality

To understand how the variables in the XCT workflow effect areal surface texture data extracted from a scan, it is important to first highlight the operating principles and fundamental workings of a modern machine. The Nikon 225 XT-H (Figure 2-3) is a modern multipurpose industrial XCT with a maximum power of 225 W, a detector size of 1,536 x 1,920 pixels and a minimum pixel size of 127 µm (Nikon,

Figure 2-3 Nikon XTH 225 (Nikon, 2022)

2022). It also offers a range of target options these are discussed in further detail in section 2.2.2.2. This machine is used thoroughly throughout the author's work and is a perfect example of a "typical" modern cone beam XCT system.

Specialist metrology XCT systems that make considerations for measurement accuracy and traceability were considered for use in the project. However, it was decided to use the non-specialist more widely utilised machine for the present study. The majority of XCT in industrial environments are likely all-purpose machines that whilst capable of metrology and surface analysis will also be used for a large variety of NDE purposes.

The Nikon machine is a typical arrangement for a modern electron tube XCT and functions as such. The key functions can be split down into three main processes, X-ray generation, interaction of X-rays with an artefact and detection or X-rays. There are sub processes to each which are discussed in more detail below.

Alongside the hardware, software suites play a key role in surface extraction and due to the unique methods of operation, XCT requires several bespoke software packages to compile the individual radiographs into a 3D model. The software suites remove noise and artefacts, determine the surface of the measured artefact, and allow for the conversion and export of data to one of a number of file formats, which can be tailored to suit user needs.

2.2.1. Basic XCT working principles

When a scan is initiated, electrons are emitted from a filament held within the X-ray tube, this emission results from the passage of electrical current and is due to thermionic emission, the phenomenon first noted by Becquerel in 1853 (Becquerel, 1853). The electron beam is accelerated down the tube by a potential difference across the tube, much like Crookes early tubes used by Roentgen during his discovery of X-rays (Roentgen, 1896). This electron beam impacts the target material interacts with the atoms in the target along its path. Only 1% of all the electron beam energy will be emitted as X-rays, the rest being lost primarily as heat. The interactions at the target, can be of several types, as discussed in section 1.6, and some of these interactions will lead to the production of X-rays. The X-rays are emitted out the tube in the direction of a sample to be analysed, in the case of most industrial XCT the sample is held on a rotating stage, though this is not a requirement and stationary samples with rotating generation and detection units such as those in medical XCT equipment are also viable. The emitted X-rays pass through the sample which will absorb an amount of the photons as they penetrate the sample material. The rate of absorption is governed by the Beer Lambert law (Equation 2-1).

$$A = \epsilon l c$$

Equation 2-1

Where

A is the absorbance

ϵ is the absorptivity of the sample material

l is the length of the path taken by a penetrating beam

c is the molar concentration

Once the X-ray beam has passed through any sample material present, the beam continues travelling towards a detector. Detectors are panels of a set size that function by measuring the attenuation

levels of X-rays per pixel, each pixel is then assigned a grey value for that image based on the attenuation level.

This process is shown above in Figure 2-4, the X-ray source (a) produces the cone beam of X-rays (b). This beam passes through the artefact (c) and into the detector (d). Once a full image has been taken of the sample, the arrangement is rotated by a given amount and the process repeated. Once a sample has been analysed over 360 ° the radiographs are combined using filtered back projection, to produce a 3-D grey scale volume from the 2D collected images. The 3-D model is a representation of the scanned samples and includes any detail that can be resolved by the XCT machine used. The level of detail obtained is dependent on the machine, with some modern machines claiming sub-micron accuracy (AXT PTY Limited, 2021). Alongside the XCT machine another governing factor of the scan's accuracy is the so-called voxel size, this is primarily determined by the location of an artefact in the machine, though other factors can influence voxel size.
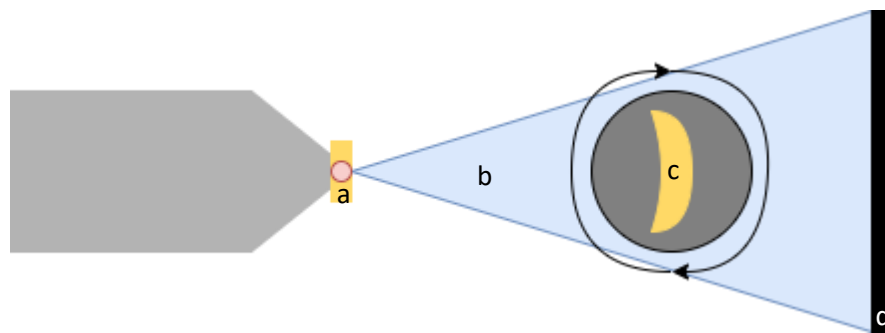
Figure 2-4 diagram of a typical cone beam XCT arrangement.

From the 3D model, data can be extracted for use in a range of NDE applications. Whilst XCT is most commonly thought of as a medical procedure, it is now commonly utilised in industry for tasks such as porosity analysis, forensic analysis, and both dimensional and surface metrology (Tawfik, 2021) (Addinall, Townsend, & Blunt, 2019) (Kruth, et al., 2011) (Townsend, Pagani, Scott, & Blunt, 2017).

2.2.2.   X-Ray generation process

The Nikon 225 XT-H (Figure 2-3) is a cone beam XCT that uses a standard electron gun with a 225kV micro focus reflection target. Cone beam XCT's are named as the X-rays are generated from a "single point" and spread out in a conical geometry from this point (Figure 2-4). This point is a spot of a focused electron beam on a target material, the reflection target in this case. The focal spot of an electron tube is determined by the dimensions of the tungsten coil, the construction of the focusing cup and the location of the filament within the cup, in general a smaller focal spot will produce a sharper X-ray image though a more concentrated spot will also damage the target material quicker (Dowdy, Murray, & Christensen, 1990). The process of generating and focusing this electron beam consists of multiple stages and is the most crucial part of X-ray generation as the characteristics of this beam determine the "quality" of the X-rays generated.

Cone beam XCT machines typically function with a setup as can be seen in Figure 2-5, the electron gun and detector remain stationary at a system specific geometry/distance. The artefact to be scanned is then placed on a rotary stage between the source and detector. The artefact is the rotated in steps taking a projection at each angle position.
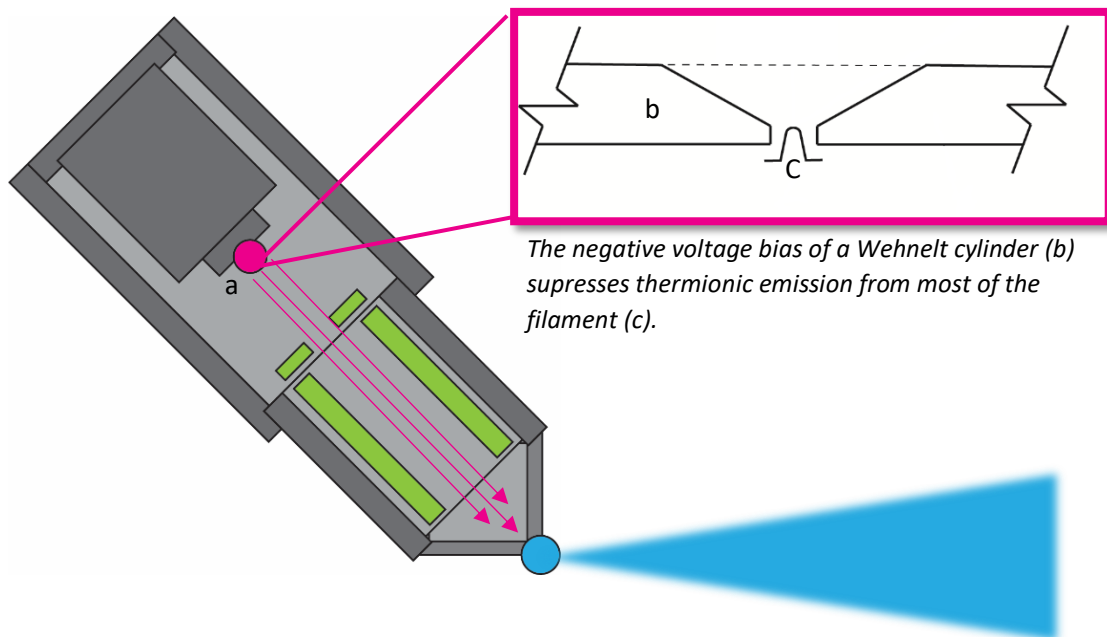
The negative voltage bias of a Wehnelt cylinder (b) supresses thermionic emission from most of the filament (c).

Figure 2-5 shows the arrangement of the filament (a) within the vacuum tube with a reflection targe electron tube, the direction of the electron beam and X-ray cone are indicated.

Electron guns such as those found in cone beam XCT are, in principle, extremely similar to the original Crookes tubes used by Roentgen. There is still an anode and a cathode, suspended in a low-pressure chamber, though the process has been heavily refined. These refinements have been because of not only improvements in technology allowing for more efficient and powerful systems, but also through improvements in the understanding of ionising radiation and a need to improve the safety of these machines. In a modern electron gun such at that found in a typical XCT, the vacuum in the chamber is of a much lower pressure than those in the original Crookes tubes. The lower vacuum means less interactions occur between the electron beam and gasses in the chamber. The lower pressure also will increase filament's useful life as oxidisation will not occur in the vacuum. The process of electron beam generation starts with the thermionic emission of electrons from the surface of a superheated filament, commonly made of tungsten. The heating is controlled via varying an electrical current across the filament. The emission is controlled by a focusing cup or Wehnhelt cylinder (Figure 2-5) which acts as a convergent electrostatic lens. The cylinder is negatively biased to prevent emission of electrons from the surface across the body of the filament. The tip of filament protrudes through a hole in this cylinder. This tip is the source of the electron beam, and the cylinder is shaped such that emission from this area is not supressed but accelerated away from the materials surface.

The electrons once emitted from the filament are accelerated towards the anode, in this case the target material where upon impact X-ray generation will occur. The Nikon 225 XT-H as standard, is equipped with a 225kV micro focus reflection single material target. The target material like the filament is tungsten. Though other target materials can be used dependant on user requirement, some machines even allow for the installation of multi material targets, increasing the adaptability of a system.

2.2.2.1. Electron tube target material

Target material selection is dependent on usage, the suitability of a material as a target is governed by two factors, its atomic number, and the energy of its electrons (Sprawls, Physical Principles of Medical Imaging, 1995). A higher atomic number leads to more efficient Bremsstrahlung production. Tungsten is commonly used due to its high atomic number of 74. Tungsten is also a favourable material due to its stability at high temperatures and low rate of sublimation (the rate of vaporisation of the material at its surface) (Planter & Sessoms, 1973). These factors lead to tungsten being an ideal choice due to the high energy X-rays it can produce alongside the low rate of wear to the target surface. Other materials commonly used can be seen in Table 2-1 below.

Table 2-1 shows commonly used anode materials for X-ray generation.

Anode Material	Atomic Number	Application
Copper (Cu)	29	Diffraction examinations – alongside tungsten it is one of the most common target materials.
Molybdenum (Mo)	42	Suitable for examination of metal alloys with atomic numbers between those of titanium to zinc, also commonly used in mammography.
Rhodium (Rh)	45	Used as a second anode in mammography, for denser tissue.
Cobalt (Co)	27	Often used in place of a copper anode when observing ferrous samples to prevent fluorescent radiation.
Iron (Fe)	26	Suitable for ferrous samples were Co or Cr tubes are not suitable/available.
Chromium (Cr)	24	Suitable for complex organic substances.
Tungsten (W)	74	Most commonly used target material in micro-CT.

The target material is typically held in a copper mounting, copper is chosen due to the beneficial properties of dispersing the heat generated by the process, approximately 1% of the electron beam energy is released as X-rays the rest is lost (Sun, Brown, & Leach, 2011).

2.2.2.2.   Electron tube target types

There are several common types of X-ray target. The Nikon 225 can use either a reflection or transmission target, but other types are utilised such as a rotating target and it also possible to use synchrotrons to generate X-rays but with different methods to the first 3 targets. A reflection target as shown in Figure 2-6, provides the advantage of better heat dispersion, thus permitting higher powers and shorter measurement times.
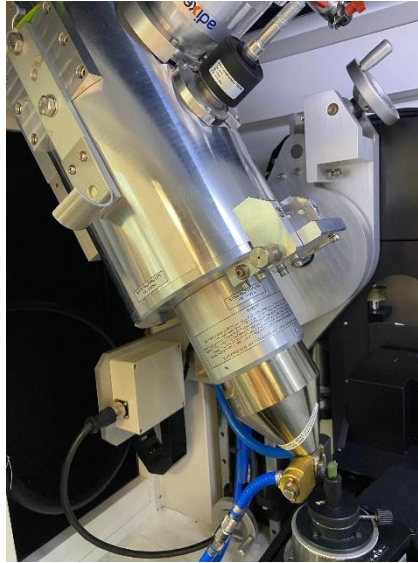
Figure 2-6 reflection target fitted to an Nikon XTH 225

As electrons travel down the tube and impact the target the X-rays produced are reflected at an angle towards the artefact as seen in Figure 2-5. The shortcomings of the system are a lowered resolution when compared to a transmission target, due to the difference in focal spot size.

Transmission targets (Figure 2-7 and Figure 2-8) function by generating X-rays that penetrate though the target, parallel to the direction of the electron beam. As the electron beam transmits through the target material most of the beam energy is lost as heat, transmission targets do not offer the same level of heat dispersion as comparable systems. This results in limits to the tubes power; however, they do offer higher resolutions as smaller focal spots can be achieved.
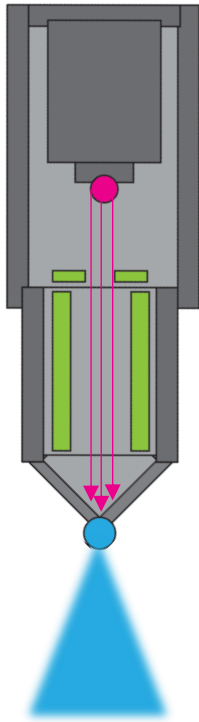
Figure 2-8 Transmission target function, the direction of the electron beam and x-ray cone are parallel.

Figure 2-7 transmission target for Nikon XTH 225.

Finally rotating targets (Figure 2-9) rotate, preventing a single point being the focus of the beam for too long, lowering the heating effect and reducing damage to the targets surface during use. Like the reflection target, this method dissipates heat better than a transmission target and thus allows higher
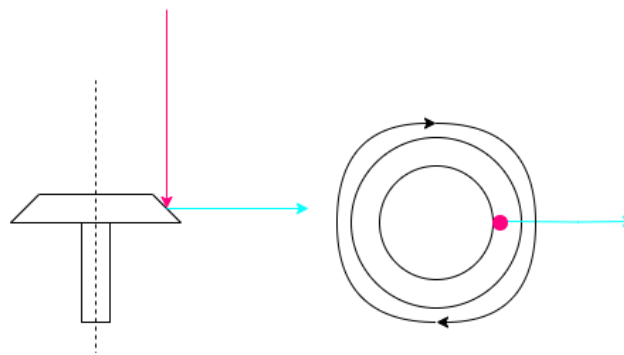
Figure 2-9 shows how a rotating target functions with the electron beam striking the rotating target, the direction of X-ray emission is indicated.

power X-rays to be produced. The use of a rotating target also spreads wear, meaning pitting is less likely to occur, this in turn will lessen the effect of focal spot drift due to a damaged target.

2.2.2.3. *Comparison of electron tube and Synchrotron x-ray sources*

Multiple studies comparing the effectiveness of synchrotron electron sources to conventional methods of x-ray generation have been conducted (Kastner, Harrer, Guillermo, & Oliber, 2010) (Sun, Ng, & Reis, 2018). Synchrotrons are advantageous as sources of x-ray radiation as they produce a nearly parallel beam of a high brilliance. This leads to a lower number of artefacts, improves contrast and resolution, and can lead to faster scan times. In Kastner et al, a comparison of μXCT sub-μXCT and synchrotron methods is carried out. Kastner refers to the small focal spot size XCT machines commonly found in industrial use with focal spots that vary in size but a generally between 1-200 μm.

Micro focus XCT or sub μ in Kastners work achieve sub-micron resolution at the cost of higher beam power. In the work, a range of steel and aluminium artefacts are assessed, the use of multiple materials allows the investigation of possible scattering and increased artefacts. It is concluded that μXCT provides the lowest level of detail, sharpness, and resolution of the three with synchrotron being the best performer. Images in the work display the clear advantage in resolution and detail of achieved by synchrotrons. Synchrotron methods do however fall back on the requirement of space and are expensive when compared to electron tube sources. The work of Sun et al again compares synchrotrons accuracy to that of conventional XCT imaging. The artefacts assessed being a range of aortic stents with the work concluding that the level of accuracy achieved by synchrotrons is much higher.

2.2.3. X-ray detectors

Detection of X-rays is the final hardware centric process in an XCT, almost everything post detection is software based. In Roentgens initial experiments detection was achieved by exposing a barium cyanide coated screen, this glowed when exposed to the X-ray photons. More recently detection is carried out using a variety of digital detection methods.

There are two main categories of X-ray detectors used in micro-CT energy integrating detectors (EID) and energy discriminating photon counting detectors (PCD) (Badea, 2021). ISO standard 15708 further divides EID detectors into two distinct groups: scintillation and ionisation detectors (International Standard Orgnsitation, 2002) Scintillation detectors currently make up the majority of those in use in modern micro-CT.

2.2.5.1. *Scintillator detectors*

Scintillation can be defined as the ionisation of transparent material, these detectors convert the high energy X-ray photons into a lower energy, in the range of visible light. The lower energy photons are detected using a photodiode. These detectors are advantageous when working with low intensity X-rays (Thompson, et al., 2009) (Sun, Brown, & Leach, 2011). The conversion of the X-ray beams to light photons is accomplished using a thin film transistor in combination with a scintillator plate and an array of photodiodes. This converts the detected photons to a digital readout that then forms the radiograph.

The Nikon 225 XT-H has an EID detector with a size of 1,536 x 1,920 pixels and a pixel size of 127 μm. X-ray detection takes place by converting the energy transported by the X-ray radiations into forms that can be detected visually or electronically. In a modern detector this takes place as the X-ray photons are absorbed by the detector material, the energy transfer being because of the ionisation of the detector material. "The number of ionizations N per photon is proportional to the energy E of the absorbed photon and depends on the average energy e necessary to produce an electron–ion pair in the detector material" (Kramar, 2017). This is mathematically described in Equation 2-2.

$$N = E/e$$

The statistical scatter of the number of ionisations per photon determines the energy resolution, as a higher number of ionisations indicates a higher energy X-ray has interacted with the scintillator. This relationship makes it possible to separate the radiation absorbed by the detector to different energies, giving a range of intensity values dependent on the density of the objects the X-rays have passed through. This is calculated using Equation 2-3, where σ is the statistical scatter and N is taken from Equation 2-2. F is the Fano factor, the measure of dispersion of a probability distribution caused by the fluctuation of electrical charge in a detector (Fano, 1947).

$$\sigma = \sqrt{(F \times N)}$$

The use of scintillation detectors also allows for high spatial resolution and fast acquisition times.

2.2.5.2.   Direct semiconductor detectors

Direct conversion detectors were developed in the 1970s using a photo conductive material typically amorphous selenium (Paulus, 1980) (Polischuk, et al., 1999), that converts absorbed photons into electronic charges (Noel & Thibault, 2004). Photoconductivity is an optical and electric phenomenon where a materials conductivity is altered due to the absorption of radiation. As X-ray photons interact with the amorphous selenium electron hole pairs are created resulting in an electrical current due to a bias in voltage (Chotas, Dobbins, & Ravin, 1999). The surface of the detector is constantly subject to a uniform electrical charge meaning as the amorphous selenium interacts with X-rays these are registered due to the change photoconductivity allowing a current. Direct semiconductor detectors are advantageous as the result in lower noise and avoid the losses that can occur using indirect X-ray detectors. In general, they produce sharper images with less noise, though acquisition times can suffer.

2.3. User Defined Inputs

When setting up a scan of a new artefact, the user of an XCT has a range of inputs that can be altered to optimise the radiographs that go onto to produce the 3D model. These parameters range from altering the time taken to capture a radiograph, moving the artefact within the scanning chamber, or altering the power of the electron beam. The user can analyse the effects of altering the inputs using two outputs, both constantly available to the user.

When setting up a scan the user has two methods of analysing the effectiveness of the given parameters, a live feed image of the artefact being analysed, and a corresponding histogram (Figure 2-10). The user must use a combination of these two outputs to optimise the scanning parameters.
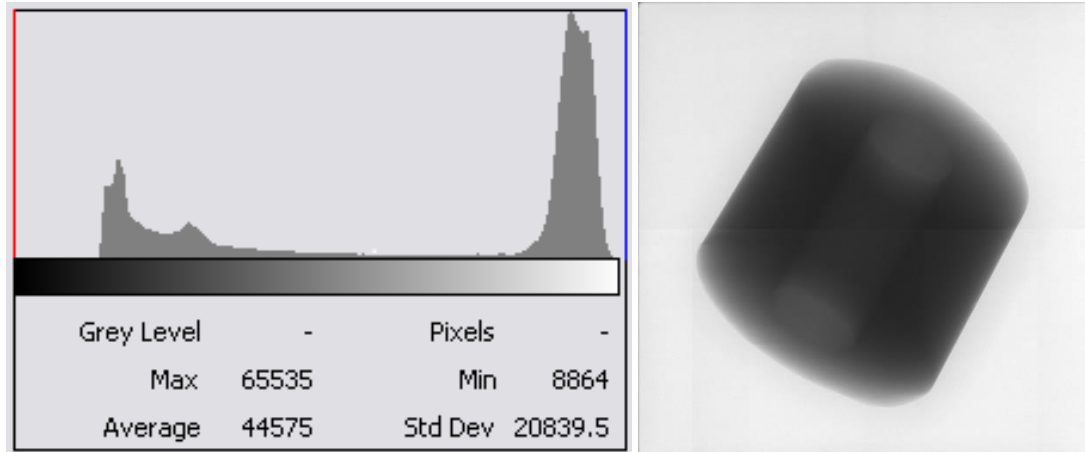
Figure 2-10 live image as displayed on Nikon XTH 225 with corresponding histogram. Each peak correlates with a material the tallest (a) being the air and (b) the artefact, in this case a section of a firearms barrel.

Work is being done in this field to develop more quantitative methods of optimising these settings, with the use of image analysis software on radiographs taken prior to a scan's initiations proving promising (Chahid Y. , et al., 2020).

2.3.1. Electron Beam Parameters

The properties of an X-ray beam cannot be influenced directly. As the X-rays are produced by the interaction of an electron beam with a target as discussed in section 2.2.2. The parameters effecting the electron beam can however been altered to control the intensity of the X-rays produced. This is achieved by using a combination of the accelerating voltage (kV) and the current across the filament determined by adjusting the wattage (W) on a Nikon XTH 225.

2.3.1.1.   Tube voltage

The tube voltage in an electron tube refers to the voltage that is used to accelerate the negatively biased electrons away from the filament, acting as a cathode. This potential difference causes the electrons to accelerate down the vacuum tube through a series of focusing apparatus and into the target. As it impacts the beam, one of a few interactions between the electrons from the beam and the electrons in the target may occur, these interactions are discussed in section 1.6. By increasing the voltage, the speed of the electrons in the beam increases, effectively decreasing the photon wavelength and the spectrum of produced X-rays. The speed of an electron subjected to 1 V of accelerating potential difference is approximately 600 km/s (University of Oxford Department of Physics, 2022). This is calculated using a derivation of Equation 2-4.

$$qV = \frac{1}{2}mv^2$$

Equation 2-4

Where q is the charge of a single electron, V is the accelerating voltage, m is the mass of the electron and v is the electrons velocity. It should be noted this equation does not consider the change in the relativistic mass of electrons as the approach the speed of light (Einstein, 1905). The theoretical results for speed of an electron in a Nikon XTH225 operating at maximum voltage are shown in Table 2-2.

Table 2-2 shows theoretical speed of an electron at a range of accelerating voltages. calculated using Equation 2-4

Accelerating voltage (V)	1	225000
Theoretical electron speed (m/s)	600000	282842712

The spectrum of X-ray produced by the electron tube is affected by this tube voltage, with the maximum X-ray energy (KeV) of the spectra being equal to the peak electrical voltage applied across the tube (Nickoloff & Berman, 1993). When observing the image and histogram, increases to the tube voltage will present with a brighter image across all sections. This will result in all histogram peaks moving to the right, potentially lowering the contrast if the voltage is set too high. Lower tube voltages will present as a decrease to the brightness, again if set too low this may lower image contrast.

2.3.1.2.   Power

The focal spot size of an XCT is proportional to the power, for a Nikon XTH 225 using a reflection target operating under 7 W, focal sizes of less than 5 μm can commonly be achieved. At higher powers, focal spot size will increase drastically, a Nikon XTH 225 running at maximum power will have a focal spot diameter approximately 225 microns in diameter. Maintaining a small focal spot will allow for higher resolutions scans to be achieved. However, this not always viable, as large dense artefacts are not uncommon in industrial applications.

Similar to voltage, when adjusting the power input of the XCT, the image intensity will shift, with higher powers increasing the brightness of all parts of the image causing a shift in the histogram that mirrors this. Likewise lower powers will result in the image dimming and again a shift in the histogram will occur. Power and tube voltage should be altered in tandem to optimise the image quality. For the Nikon XTH 225 used throughout the authors work scanning parameters should aim for intensity values in the 60000 range for background and 10000-15000 for material. These should be achieved using lower values in order to optimise image quality. When shifting the power, the user is controlling the intensity of the X-rays emitted, without altering the wavelength, as is done when changes are made to tube voltage (Sigl & Quinn, 1980).

On the Nikon XTH 225 when using a reflection target, if the power is increased over 10W the machine should be put into auto defocus mode. This setting purposefully defocuses the electron beam to prevent the damage to the target at higher powers, Figure 2-11 shows examples of this damage.
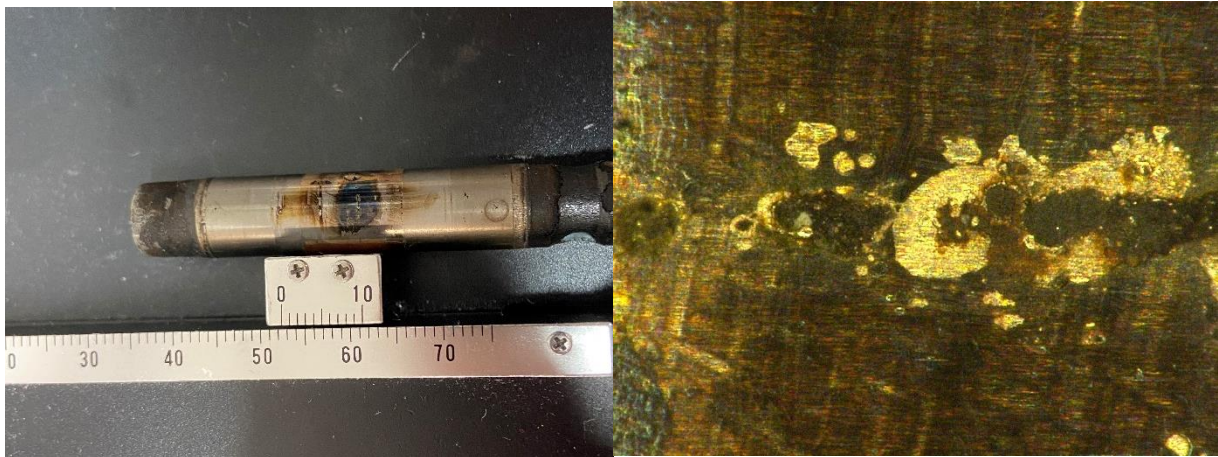
Figure 2-11 damaged tungsten section of a multi-material XCT target at 1 X (left) and 200 X (right) high mag image taken using a Keyance optical microscope.

A damaged target can affect the focal spot and thus any scans taken using that target. Single material targets can be rotated to allow for a different area of the target to be used, and this should be carried out occasionally as part of the standard maintenance cycle of the machine. If using multi material targets the user should make sure the target is rotated such that the preferred material as discussed in section 2.2.2.1 is in the correct position.

2.3.2. Exposure timing

Exposure timing is a user-controlled input that controls the period of time that the XCT will take a radiograph at each projection angle. For the Nikon XTH 225 this ranges from 134 ms to 4000 ms. Similar to an everyday camera as exposure time increases the number of photons interacting with the detector increases. In a camera this leads to a brighter image, this is mirrored in an XCT. If an image is already bright, a high exposure time can lead to a "white out". This can be seen in Figure 2-12 where an artefact is imaged at 250 ms, 1000 ms and 4000 ms exposure without adjusting other inputs to compensate for the longer exposure. When balancing the image and histogram for an optimum radiograph, the trade-off for using longer exposure is that scans will take longer. As a result, whilst using low power and voltage at a trade for a longer exposure, may seem favourable it is not always practical.
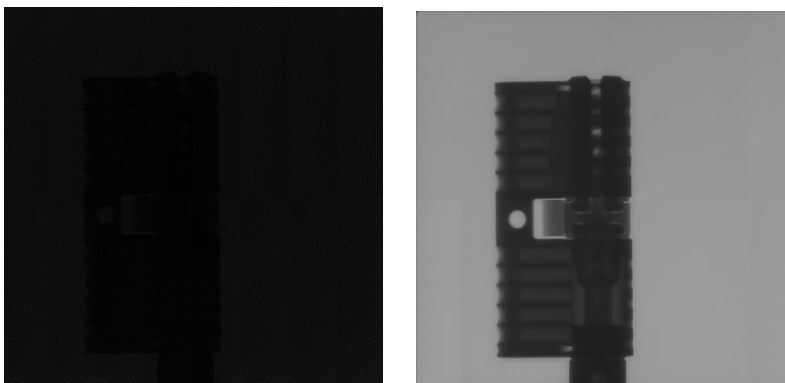
Figure 2-12 underexposed (left), "good" exposure (centre) and overexposed (right) radiographs of the same part (a lock mechanism)

2.3.3. Magnification

Magnification in an XCT, refers to the distance between the X-ray source and the centre of rotation of the artefact stage. The magnification achievable is limited primarily by the size of the area of the work piece being imaged. There are several considerations that a user must make when setting magnification such as the region of interest size and the scale of interest.

The size of the region of interest relates to how large an area is of interest to the user. A large region of interest will require the artefact be further away from the source as the cross-sectional area of the X-ray cone beam, increases as it approaches the detector. The region of interest of a single scan cannot exceed the area at the minimum magnification of the machine, though if this is the case, various methods can be used to image the entire part without additional user input. Batch scans and helical scans allow for large parts to be imaged at appropriate magnifications. Batch scans complete a normal rotary scan then move to a second scanning location and another complete set of scans are acquired using identical parameters. Helical scans move the artefact in the Y axis during the scan to increase the size of ROI that can be scanned.

The scale of interest relates to the level of detail the user is interested in. Depending on this the level of magnification required can be set. As discussed above the beam of a cone beam XCT increases in surface area as it approaches the detector. The closer an artefact is to the source the large percentage of the beam it will interact with. Any feature on the artefact in the beam will influence a larger number of X-rays, this will propagate as covering a greater area on the detector as the beam spreads. The greater the number of detector pixels covered by a feature the higher resolution the representation of the feature in the final scan will be. This is shown when observing the voxel size of a 3D model. Voxels are 3D pixels that make up models generated by XCT; smaller voxels allow for a higher level of detail. Voxel size is governed by the size of a feature compared to the area it covers on the detector. The effect of how an objects position in the CT effects it's both scale or interest and the viable region of interest size is shown in Figure 2-13.

High resolution - Smaller region of interest

Low resolution - Larger region of interest
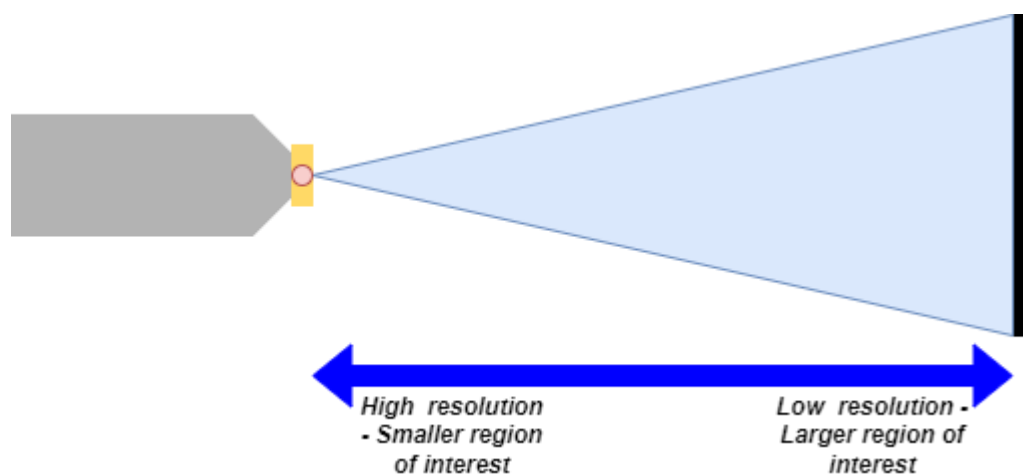
Figure 2-13 shows how the region of interest and resolution are affected by location in XCT chamber.

2.3.4. Filtration

Beam hardening is a systematic error common when using XCT to image artefacts made of dense materials, this is further discussed in 2.4.3. To reduce the number of low energy electrons that are responsible for the beam hardening phenomena, filtration can be introduced. Filtration is the use of a thin piece of material, commonly copper, installed at the x-ray source window. The thickness of the strip can vary from 100 μm to over 5 mm. The selection of a filter material is related to the K-absorption edge, this is defined as the "abrupt increase in the photoelectric absorption of x-ray

photons observed at an energy level just beyond the binding energy of the k-shell electrons of the absorbing atom." (Murphy, 2020). Aluminium is a very common filter in medical imaging due to its low K value 1.6 keV, for industrial users, copper is preferred with its higher K-absorption edge of 8 keV.

Users should consider filtration when increasing tube voltage. As the tube voltage increases the thickness of a required filter should also increase. Penetration of a dense material requires increased voltages. To filter out the lower energy X-rays generated by the tube at high voltages a filter should be used.

2.4. Systematic error sources in XCT

There are several common sources of systematic errors in XCT. These errors relate to a variety of the sub-systems within the XCT such as the X-ray tube, detector or possibly the artefact being imaged. This section covers the major error sources that have been identified as having a clear effect on results gathered using industrial XCT.

2.4.1. Focal Spot Stability and Beam Drift

Beam drift is the phenomenon influenced by certain factors during the operation of the XCT, chiefly among these is the thermal expansion of the X-ray tube during use. It is defined as an error as shifting of the spatial stability of the X-ray focal spot. As noted previously for sufficient thermionic emission from a emitter filament, high temperatures must be achieved, when using a tungsten filament these can commonly exceed 2000 K. In addition to this various section of the vacuum tube such as the electron optics also will increase the heat energy in the system. The extreme temperatures will cause the expansion of elements of the X-Ray tube, this heating can even lead to damage to the target in the machine due to overheating (Sprawls, X-Ray Tube Heating and Cooling, n.d.)

As the tube expands the electron beam focal spot may drift (Sun, Brown, & Leach , 2012). The positional stability of the focal spot has the potential to affect both 2D radiograph and 3D CT measurements. As such, methods of measuring spot stability have been developed (Vogeler, Verheecke, Voet, Kruth, & Dewulf, 2011). Vogeler et. al. demonstrated a method for measuring the positional drift of the beam in an XCT machine using a hole plate, as source temperature is highlighted as a cause of beam drift, temperature probes were fitted to the source for these experiments. Radiographs of the plate were taken regularly over several hour-long heating cycles of the source.

Results show that the position of the holes in the radiograph drifts upwards with heating, with temperature probes indicating the thermal expansion of the source in primarily in the beam axis. The authors go on to suggest a method for correction of these issues in 2D radiographs, though a method for correction in 3D XCT is not presented. A control group of data, with a source allowed to heat to an equilibrium prior to taking radiographs may have allowed the authors to better the significance of the noted drift.

The heating phenomenon can be somewhat counteracted by the implementation of cooling systems, or rotating target materials which disperse the heat over a wider area and analysis and work has been carried out focusing on reducing focal spot shift as demonstrated by Steffen and Froeba. (Steffen & Froeba, 2011). Who again used thermals sensors mounted inside of the tube. This was also shown by Ferrucci et al. who measured spot drift over a period of 2 hours with external cooling of the source (Ferrucci, Leach, Giusca, Carmignato, & Dewulf, 2015). Their paper, which demonstrates various geometric inaccuracies, shows the results of a study where focal spot drift and the thermal extension of the gun are measured. The uncooled tube results show both spot drift and thermal expansion of around 30 μm, whilst with externally cooled tube is demonstrated to have a much lower level of drift. The results of this are shown in Figure 2-14. It is clear from the lack of variation in y when comparing the two data sets that external cooling is a significant contributor to achieving a stable beam spot.
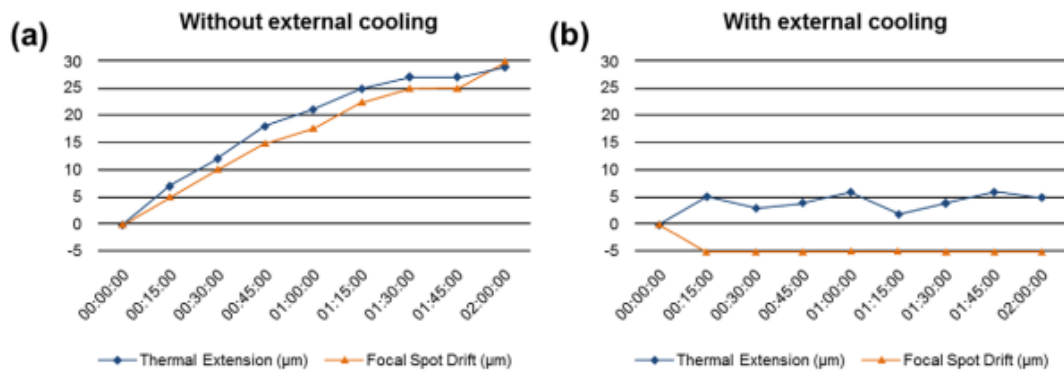
Figure 2-14 graphical results from Ferrucci et al's experiments on the effects of cooling on focal spot stability with (a) showing the results of no external cooling and (b) showing results with external cooling applies. Taken from (Ferrucci, Leach, Giusca, Carmignato, & Dewulf, 2015)

The authors also suggest that the use of systems where the x-ray tube is mounted in such a way that the target is bolted to the machines frame, thus resulting in thermal expansion of the tube having less effect on the target drifting.

Several methods exist for the quantification of focal spot stability in literature and now accepted into standards such as those detailed in BS EN:12543 of the Siemens star method developed by Probst et. al. (BSI, 1999) (Probst, et al., 2019). The methods presented in the standards are discussed further in Chapter 5 as they are considered for use as the basis for development of a novel method of focal spot measurement.

The method detailed by Probst et al. at KU Leuven uses a Siemens star (Figure 2-15) to measure the focal spot geometry (Probst, et al., 2019). The method uses a sinogram acquired by looking at the edge spread function of a siemens star pattern comprising of 120 stripes.
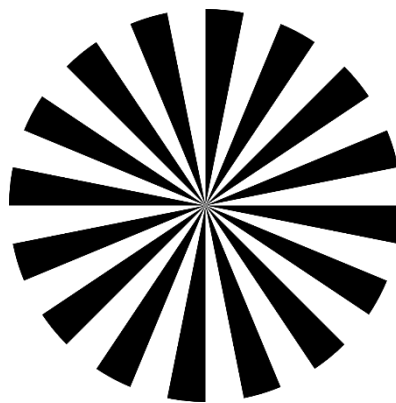
Figure 2-15 example siemens star pattern (SSP)

The method collects the edge spread function along a radial path with all points equidistant in relation to the centre of the pattern, this allows the centre of the Siemens star (SSP) to be determined. By using aRTist (an X-ray simulation software) to simulate an XCT focal spot of know size the threshold value could be determined when using the Siemens star which meant the measured focal spot matched the simulated known size. This threshold value was then used in real world experiments to measure focal spot size.

For real world experimentation, an SSP of 120 stripes was fixed to the x-ray tube window as shown in Figure 2-16. 1-hour scans of the SSP were taken each consisting of 3600 individual projections. The

focal spot shape can then be generated for all images using the method. The protocol provides a novel method that requires only a single piece of equipment, an SSP of know geometry, to function and provides measurements of the focal spot with a higher precision, it also allows the user to investigate the geometry and intensity of the spot.
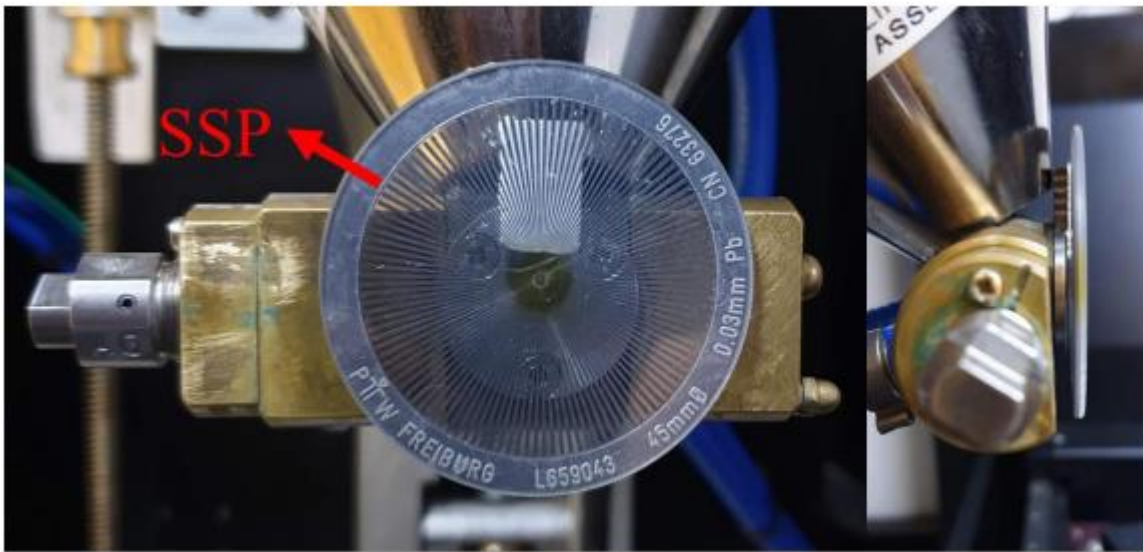
Figure 2-16 SSP attached to X-ray tube taken from (Probst, et al., 2019)

The mounting of the star shown in Figure 2-16 does appear to show the star mounted to a filter, this may have had an effect on the measured focal spot as less intense X-rays would not penetrate the filter. The work goes on to investigate the effects of various focal spots on the simulated measurements on a sphere, 3 different focal spots, one Gaussian and two non-uniform shapes are simulated, and a simulated scan of the sphere is carried out. Comparison to the original model of the sphere shows the polar regions of the sphere having greater deviation than around the equator. This deviation is more significant for the less uniform focal spots. This demonstrates the effect that beam, and focal spot drift have on measurements taken using XCT.

It is worth noting the drawback of Probst's method it would be unable to correlate the simulated results to real life data of variation of a sphere. As the SSP covers the source window it would require removing for a scan of the sphere to be taken. As shown by work done by Vogeler et al. the focal spot geometry varies significantly over the period of an hour, thus if the spot were measured prior to a scan, it is likely the spot would vary during the scan and this could not be tracked.

2.4.2.   Ring artefacts

Ring artefacts are an issue common to XCT, the artefacts (Figure 2-18) are the result of defects relating to x-ray detection. Figure 2-18 shows a severe level of ring artefacts. One of several issues relating to the detector can induce ring artefacts these include:

- Defects in the detector material
- Poor calibration of the detector
- Nonlinear behaviour of the detector materials
- Variation between detector channels, i.e. the detector is not performing uniformly
- The mechanical misalignment of the source and detector

Ring artefacts may also result from the detector's sensitivity being finite. A faulty detector pixel may also lead to the introduction of ring artefacts in any scans produced using the faulty detector. Due to the clear issues with ring artefacts, detector alignment and uniformity are key to obtaining best scanning outcomes (Yaffe & Rowlands, 1997).

Work has been undertaken to produce methods of removing ring artefacts from scans. Both prior to and post reconstruction. The pre-reconstruction removal of ring artefacts is shown by Rivers who demonstrates a method for reducing the effects of ring artefacts prior to reconstruction (Rivers, 1998). Prior to reconstruction a ring artefact will appear as a vertical stripe in the sinogram, the image from which the reconstructed slice is produced. As in sinograms it is typical for real objects in the scan to move in a sine wave defined by the object's location in reference to the centre of rotation. This allows for ring artefacts, appearing as straight lines to be easily identified and thus corrected for as shown by Rivers. The method presented by Rivers et al is based on image analysis comparing row averages to allow for the filtering of the streaks that do not follow a sine wave pattern of movement through the rotation of the scan object. Whilst effective this method is somewhat simplistic in its approach, later work by Munch et al used a method comprising of wavelet/Fourier filtering that is demonstrated by the authors to cover a range of data to correct for ring artefacts (Munch, Trtik, Marone, & Stamanoni, 2009). When comparing the two methods presented by Rivers and Munch et al. respectively, whilst Munch's method is a more thorough method that is shown effective across a range of data sets, Rivers methods' simplicity means it is easier to implement. Both methods discussed are implemented post scan, however it is now common for manufacturers of XCT machines to provide pre scan corrections where possible. As noted, one of the common sources of ring artefacts is a faulty or "dead" pixel on a detector. These dead pixels result in a false value reading consistently through the use of the detector. It is possible to quantify these dead pixels by taking unobstructed radiographs of the panel, all functioning pixels would in this case read approximately equal values, meaning a non-functioning pixel will show as a clear anomaly as seen in Figure 2-17.

Once quantified these faulty pixels can be corrected for using a method such as averaging with its neighbour pixels, though the corrected information may not be a good representation of the ground truth.
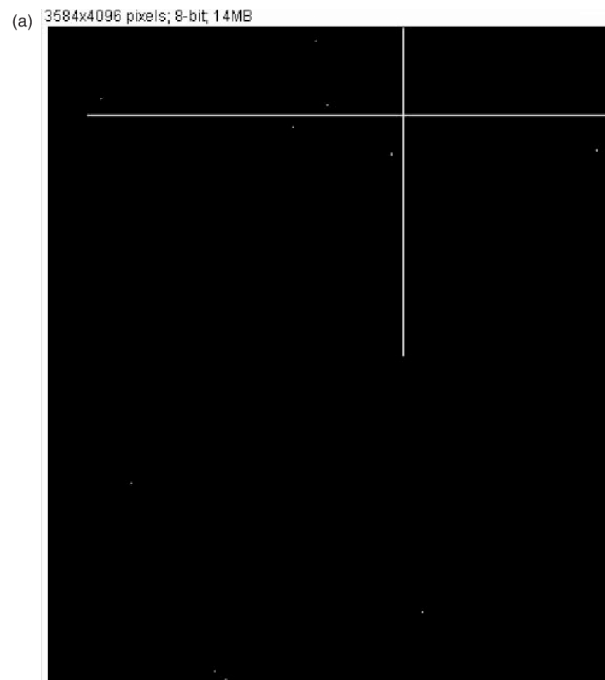
Figure 2-17 shows an example bad pixel map of a detector, the white dots represent individual bad pixels with the streaks showing dead rows or columns of pixels. Image taken from (Bosmans, Carton, Rogge, & Zanca, 2005)

2.4.3. Beam hardening

Beam hardening occurs most commonly when scanning dense materials using X-rays, the transition of the X-ray beam through the dense material results in the lower energy X-rays absorption. As the reconstruction algorithms of XCT assume the absorption of X-rays is dependent on material not the level of individual X-ray photons. This disparity between the assumed uniformity of the energy of X-ray photons and the real results can lead to errors in the levels of attenuation of X-rays during the XCT scan. Artefacts from beam hardening manifest in two ways, streak artefacts and cupping artefacts. As seen in Figure 2-18. Various methods have been developed to somewhat correct this beam hardening, these can be split into the use of dual energy scans, and pre/post processing methods.
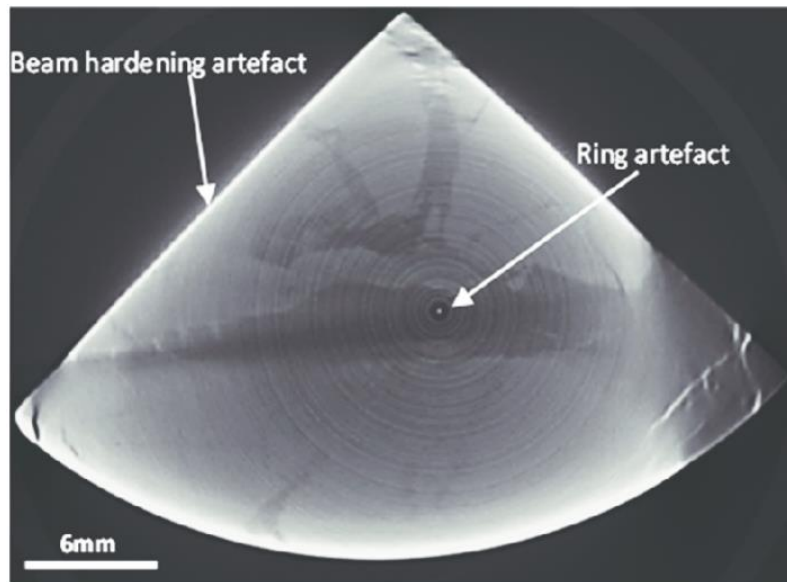
Figure 2-18 illustrates artefacts due to beam hardening and "ring artefacts".
Taken from (Bam, Miller, Becker, & de Beer, 2016)

Physical filters can be used to prefilter the X-ray beam and remove low energy photons prior their interaction with the part. Common filter materials include copper and aluminium, which can be of varying thickness's commonly ranging from less than 0.1mm up to 5mm. The filters are installed in front of the source so any emission must transit through them. This method is the most straightforward way to prevent beam hardening but is not without issue as it can lead to reductions in the signal to noise ratio.

Post detection correction of beam hardening effects can be achieved using quadratic polynomials, fitted to a data set as generated early in the development of CT by G Herman (Herman, 1979). Herman's work whilst focussing on medical analogues, shows a good analytical understanding of the issue of beam hardening and demonstrates a method of correction. This procedure is applied to images of a phantom designed to give a good analogue of a human thorax and the corrected images show a significant reduction in beam hardening. It is noted that the scanning of multi-material parts makes correction of the issue problematic as the varying attenuation coefficients increase the severity of the issue. A material focused beam hardening correction has been demonstrated more recently by Van de Casteele et al, where attenuation of materials was measured at different thicknesses using a simple wedge shape phantom (Van de Casteele, Van Dyck, Sijbers, & Raman, 2003). This allowed the linearisation of the attenuation curves of the material. Demonstrating a mathematical model for correcting for beam hardening. The method is then adapted to work on natural materials such as bone without the use of a wedge phantom, as producing the phantom in certain materials such as bone is impractical.

Several iterative methods have also been employed giving a range of methods of correction for beam hardening (Bock, Hoppe , Scherl , & Hornegger, 2007) (Van Gomple, et al., 2011). Bock et al's method uses simulated CT data to demonstrate an iterative correction model which integrates both a backward and forward projector. Using this method the authors demonstrate a good level of reduction of the beam hardening artefacts after 4 iterations, the combination of both a backward and forward projector is shown to remove both cone beam and beam hardening artefacts. In their paper Van Gomple et al describe 3 methods of iterative correction for beam hardening, all methods are used

on real world data as opposed to Bock et al whose paper limits itself to simulate CT data. The three methods are split into two categories, 2 reconstruction algorithms IGR and IFR and a pr processing method, ISP. The reconstruction algorithm methods make corrections to the data during the CT reconstruction process with IGR being gradient based and IFR using a filtered back projection. ISP is a method based on the processing of the sinogram such that the beam hardening corrections are made prior to reconstruction. All three methods require no information on the source energy spectrum, as time is saved measuring this variable. Van Gomple et al showed the 3 methods to produce good levels of correction. It is also of note that the authors state it can be favourable to sometimes use less physical filtering to prevent beam hardening in low contrast objects. Instead relying on the software corrections to remove the artefacts, whilst preserving more data that may be lost with the use of physical filters. Though this is somewhat user and use case dependant.

As noted, beam hardening is a result of variation in the flux of the x-ray beam, the use of dual energy beams as a method of correcting force this has been implemented. Dual energy methods produce radiographs with differing contrast characteristics to normal radiography, two X-ray beams of differing energy are used to facilitate this (Pettersson & Allison, 2001) (Alvarez & Macovski, 1976). Alvarez and Macovski in a paper focusing primarily on medical diagnostic imaging showed early in the development of XCT that by varying energy they were able to correct for cupping artefacts seen in images of a skull. They note that systems that focused only on beam intensity and not varying energy required alternate methods of correction. The technique is expanded upon in the encyclopaedia of medical imaging by Pettersson and Allison who note the use of dual energy methods allows for the incorporation of accurate beam hardening corrections can be incorporated into the reconstruction procedures of a dual energy scan. It should be noted however that dual energy correction can only be performed on certain CT machines and thus is a more expensive method of correction.

2.4.4. Partial Volume Artefacts

Partial volume artefacts occur in two distinct manners, firstly when a section of the object being measured partially covers a detector pixel, as this happens the pixel is receiving two different streams of x-ray photons one where the photons have travelled through free space and the other where they have passed through the material. As a typical detector will average these values leading to a region of geometric unshapness as the pixel reads a value between the material and surface.

Alternately a variation of partial volume artefacts can occur when an area of the object being measured when the limited field of view of an XCT means the object is not completely in view throughout the rotation of the scan (Abdulla, 2021).

2.4.5. Summary of systematic error sources

Work done to identify the sources of artefacts effecting XCT has found that various influencing factors can lead to artefacts and inaccuracy in XCT. The corrections whilst helpful do not eliminate all artefacts and some, such as filtering, require the user to pre-empt the presence of errors. Moving forward, work should be carried out to understand how the presence of these errors effects results extracted from XCT, although corrections may assist in preventing them, knowing the effect they have would allow for more advanced correction if necessary. Recent work by Probst et al among others highlights the focal spot as a particular region of interest, it has been shown that drift in the spot can result in variation in measurements as demonstrated by Vogeler et al.

2.5. Factors effecting scan quality

Prior to initiating an XCT scan a user must first decide on the settings of the machine, to best optimise these for a scan the user can consult the live image and the associated histogram. From these two outputs a user can alter the settings discussed in section 2.3 to best optimise the scan. Optimisation is dependent on the user requirements, several factors should always be considered, resolution, greyscale pixel intensity and image contrast alongside the geometric un-sharpness of the image.

2.5.1. Spatial resolution

Resolution is the ability of a system to measure the distance between two points. Typically, when a value for resolution is given, this corresponds to the smallest resolvable geometrical feature from an image. To calculate the resolution of an object in XCT, the magnification (M) must first be calculated. This is calculated using the distance from the source to the artefact centre of rotation (SOD) and the distance from the source to the detector (SDD), this is shown in Equation 2-5 with SSD and SOD defined in Figure 2-19.
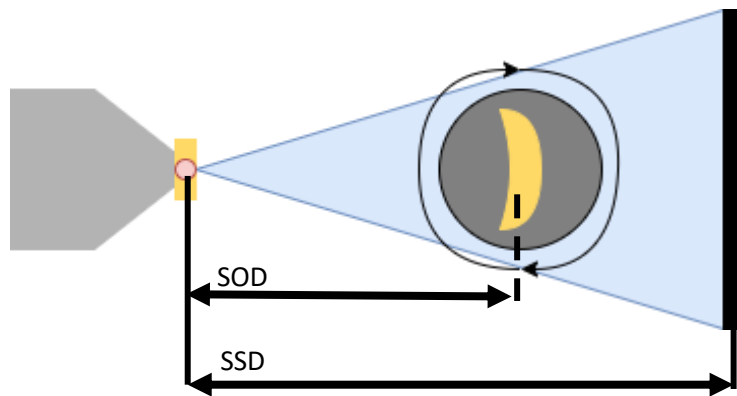
Figure 2-19 defines SDD and SOD in relation to the source, object of interest and detector

$$M = \frac{SDD}{SOD}$$

Equation 2-5

The spatial resolution can then be given as

$$\Delta X_{Obj} = \frac{\Delta Xdet}{M}$$

Equation 2-6

Where $\Delta Xdet$ is the pixel size of the detector. This allows the resolution of an XCT scan to be calculated. Under ideal conditions this is the only influencing factor governing XCT resolution. However, under real world conditions focal spot size also has a tangible effect on XCT spatial resolution. This is due to the penumbra effect, as demonstrated in Figure 2-20 comparing ideal and real-world emission of X-rays.
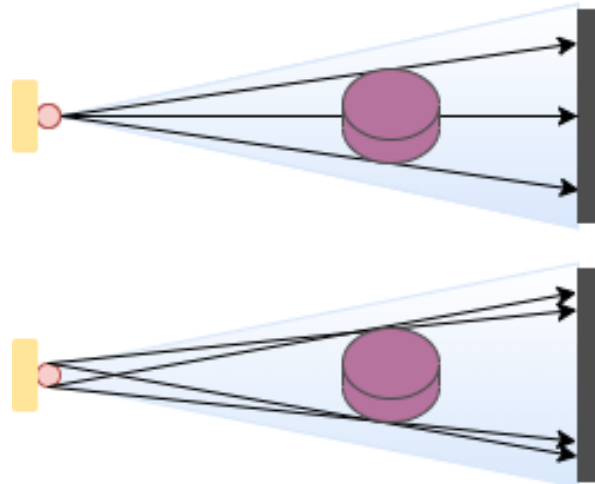
Figure 2-20 X-ray emissions form an ideal point source (top) compared to a real-world focal spot (bottom)

Under "ideal" conditions emission occurs from a single point, X-rays spread in all dimensions equally in a cone beam pattern. In reality X-rays are emitted from a 2D spot on the target, the focal spot as discussed in section 2.2.2. The focal spot is an area from which X-ray emission occurs, emission can occur from anywhere within the area. In the ideal scenario X-rays travelling through an artefact will all take the same path dependent on the angle, whereas in the real-world scenario X-rays paths differ dependent on the origin point. Around the edge of the artefact this can lead to levels of geometric un-sharpness (Sprawls, Blur, Resolution, and Visibility of Detail, 1995).

The geometric un-sharpness is caused by X-rays that interact with the same point of an artefact taking different paths. The difference between the locations where these X-rays interact with the detector causes a blurred region that it most noticeable around the edge of an artefact. As focal spot size increases the error is exacerbated.

Geometric un-sharpness (U) due to penumbra can be calculated using

$$U = f \times \left(\frac{OID}{SOD}\right)$$

Equation 2-7

Where f equals the focal spot size and OID is the distance between the artefacts centre of rotation and the detector. As discussed in section 2.2.2 focal spot size should be minimised where possible. Figure 2-21 of a sphere highlight this well as when a profile is taken across the centre of the ball bearing the intensity values across the trace show a slope at the air/material boundary instead of a more sudden change in value. At higher values the slopes gradient will decrease as the geometric un-sharpness worsens.
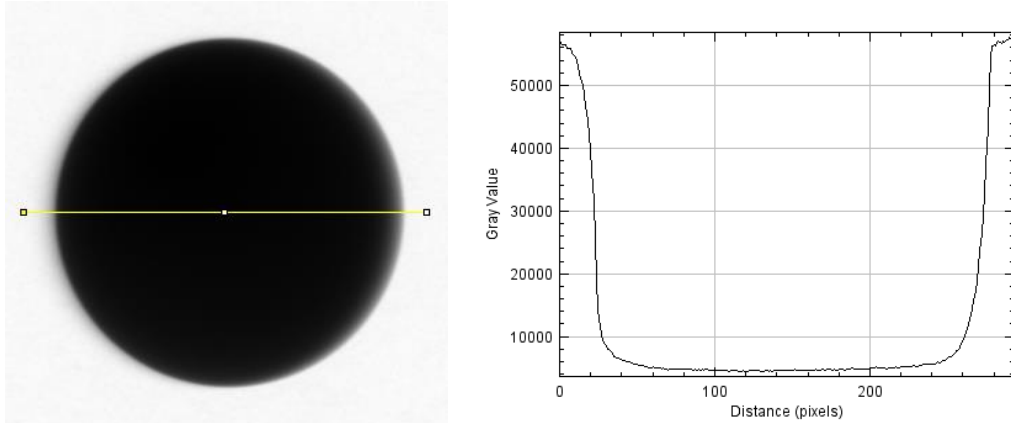
Figure 2-21 profile trace showing pixel greyscale value (right) of radiograph of sphere (left)

When dealing with radiographing more complex artefacts, if the geometric un-sharpness exceeds the space between features, detail can be lost (Figure 2-22). Two methods of assessing the resolutions attained in radiography are the contrast transfer function and the modulation transfer function. The contrast transfer function (CTF) is used to assess the ability of a system to resolve different features in a radiograph that is blurred.
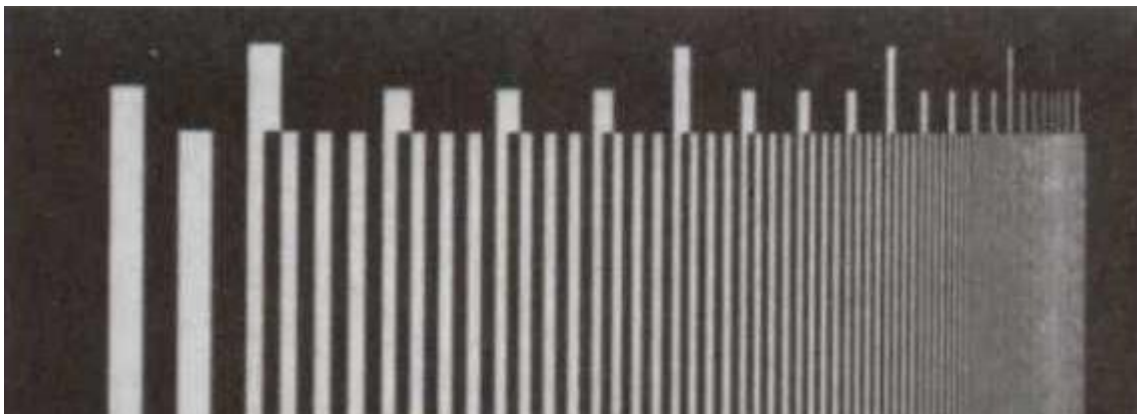
Figure 2-22 test pattern showing how detail is lost due to geometric un-sharpness, taken from (Sprawls, Blur, Resolution, and Visibility of Detail, 1995)

The modulation transfer function (MTF) is similar but describes a system's ability to image sinusoidal shapes, whereas the CTF is used to evaluate image line pairs (Sprawls, Blur, Resolution, and Visibility of Detail, 1995). When using the MTF one peak and one value make up a single cycle, with the spatial frequency being characterised by the number of cycles per mm. Compared to the CTF which measures the number of lines and spaces per millimetre see Figure 2-22. The possibility of detection of a given feature in a scan is dependent on its own size, the XCT resolution and the presence of noise.

2.5.2. Image contrast

Image contrast of an XCT system is defined as the ability to register variation in the grey scale values within the radiograph. The parameter used to quantify contrast is the signal to noise ratio (SNR).

$$SNR = \Sigma_i \frac{(x_i - x_{bg})}{\sigma_{bg}}$$

Equation 2-8

Where x_i is the region of interest pixel signal amplitude, x_{bg} is the background pixel signal amplitude and σ_{bg} is the background noise. Contrast becomes an issue when small features in a scan create a small variation in the pixel intensity of the background, this can lead to inaccurate edge detection and difficulty in separation of background from an artefact being imaged. Good image contrast will mean a wider range of grey scale values.

2.5.3. Grey scale

Grey scale in radiography is the measurement of photon intensity at a given point on a detector, typically given as a 16-bit value (0 − 65535) though 8-bit greyscale (0 − 255) can also be used. As X-ray photons pass through an object some will be attenuated as they interact with the atoms in the part. As a result, the intensity of X-ray photons will drop leading to a lower grey scale value. If no X-rays penetrate an object and the detector reads nothing the presented value will be 0, conversely if the image is oversaturated with high power x-rays the value will be the maximum 65535. Values of grey scale relate to the level of attenuation and therefore density and thickness of a part, when viewing the histogram of a radiograph or scan this is seen at the peaks. With individual peaks representing different materials or wall thicknesses present in the scan (Figure 2-23).
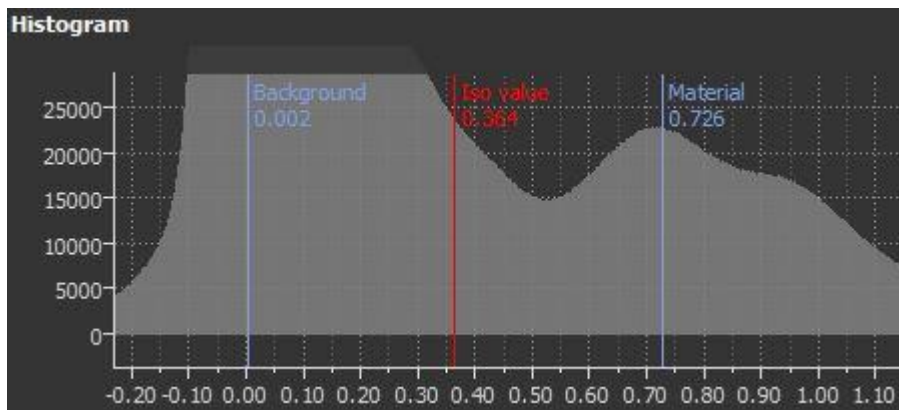
Figure 2-23 shows a histogram taken from VGStudios Max the material peak has a second smaller rise indicating the presence of a second material

The individual peaks show the presence of different materials with, in the case of Figure 2-23 case both artefacts were suspended in a super low-density foam. Work holding methods must be considered when using XCT as for certain applications the inclusion of a second material such as a work holding jig may affect scan quality.

2.6. Reconstruction

Data from an XCT does not come as a ready to use model of the scan, a process of reconstruction must be carried out, the steps of which can vary depending on the application. XCT machines do not output 3D data such as a mesh or point cloud. Typically, they produce a stack of image files, each an individual radiograph. These images are taken at set angular distances from each other over 360 degrees. The number of these images taken varies by machine, user preference and application. Reconstruction algorithms have been designed to optimise the data during reconstruction, optimisation can be defined as the removal and prevention of artefacts and noise. There is not currently a standard method governing how reconstruction algorithms are applied. As such the algorithms tend to be machine and manufacturer dependent.

Algorithms fall into one of several methodologies, Statistical reconstruction (Shepp & Vardi, 1982), algebraic reconstruction (Gordon, Bender, & Herman, 1970) or reconstruction via Fast Fourier transformation sometimes called analytical reconstruction (Janssens, 2018).

2.6.1. Statistical reconstruction

Statistical reconstruction attempts to estimate a solution accounting for both the likelihood of viewing the measured projections whilst accounting for the statistical difference between the source object and detector. It is a favourable method at low powers and is able to reduce both beam hardening artefacts and noise. Several methods of statistical reconstruction have been developed including maximum likelihood expectation maximisation (Lange & Carson, 1984) (ML-EM) and the ordered subset convex algorithm (Kamphius & Beekman, 1998). This method does result in long computation times and assumes the polychromatic spectrum of the source.

2.6.2. Algebraic reconstruction

Algebraic reconstruction methods can be separated again into two groups: Landweber and Kyrlov subspace methods. These methods share commonality in the flexibility of the procedure, allowing for geometries that deviate from convention circular or helical scan geometry, this flexibility is at the cost of higher required computation power.

2.6.3. Fourier transformation reconstruction

Fourier transforms as a method for reconstruction are based around Fourier slice theorem. This states that a 1D Fourier transformation of the projection data is equal to a slice of two-dimensional Fourier transformation of the original object at angle θ (Kak & Slaney, 1988). There are various sub methods of analytical reconstruction such as filtered back projection. The great benefit of Fourier transformations as a method of reconstruction is the rapid reconstruction times, leading to their widespread adoption in industry. The major drawback of using analytical reconstruction is the lack of flexibility compared to other methods of reconstruction. The Nikon XTH 225 used throughout the studies detailed in this work uses analytical reconstruction methods in its reconstruction software (CTPro).

2.7. Visualisation

After a scan has been reconstructed it is presented as a 3D volume made of slices of the object scanned, like with reconstruction, the exact format of this is dependent on the machinery and software used. Common visualisation software suits include VG studiomax, Avizo and Simpleware. The visualisation software will allow both analysis of the 3D volume and 2D slices in XYZ and allows users to perform advanced analysis of a scan model and prepare it for data processing. This can take the form of analysis in the software itself such as VG studio's in-built porosity analysis module. It can also mean the preparation of data for export to other specialist software, dependent on user requirements. Common features of XCT visualisation suites includes, dimensional metrology, porosity/inclusion analysis, comparison to 3D mesh and volume segmentation. It is also often the car simply viewing the reconstructed model may be enough to perform the required analysis.

2.7.1. Surface determination

A key process offered by most commonly used visualisation packages is surface determination. This key process analyses the grey scale intensity of each voxel and using one of several methods defines a surface from these values. Most methods of surface determination can be split into 2 sections, global and local determination.

2.7.1.1. *Global Determination*

Global determination uses a single grey value as a threshold applied across the entire scan, with the surface being defined by where a voxels grey scale falls in comparison to this threshold. The selected value is typically defined using one of two methods, analysis of the histogram using a determined threshold such as ISO50% of by selecting a volume in both the background and material volumes.

2.7.1.2. *Local iterative determination*

Local determination methods again start with a target value, from this a guide surface is identified. The grey scale intensity of voxels in the surrounding local region around the surface are then analysed further. The size of this local analysis region can be altered. After analysis the surface is located using the maximum grey scale value of the voxels in the reading.

2.8. Use of XCT in modern engineering

The use of XCT in modern engineering is varied, with XCT offering a novel method of NDE of artefacts that can produce detailed data about otherwise inaccessible sections of objects being scanned. Common uses for XCT in industrial settings include, failure analysis, porosity analysis, metrology (both surface and dimensional), and forensic analysis (Addinall, Townsend, & Blunt, 2019) (Tawfik, 2021) (Thompson, et al., 2017) (Ferucci, 2018).

2.8.1. Porosity

Porosity is defined as the ratio of the volume of all voids in an object to the total volume and is usually expressed as a percentage. Porosity can be beneficial or detrimental dependent on application, traditionally porosity has been analysed in one of a number of ways. These include microscopy (visible light and SEM), measuring the absorption of gas or liquids (commonly nitrogen and mercury respectively), and pycnometry.

XCT has been used for porosity analysis since very early in its adoption into industry, as previously noted in Figure 2-2. The use of XCT as a porosity analysis tool has great advantage over the established methods. XCT volumes of sufficient resolution can provide a highly detailed analysis of the pores and inclusions in an object. Not only can the overall porosity be measured but the location, size and shape can be measured and analysed. VG studios max has an inbuilt probability based porosity analysis suite that automatically detects pores and analyses them based on users' requirements, an example of this can be seen in Figure 2-24 (Wells J. M., 2007).
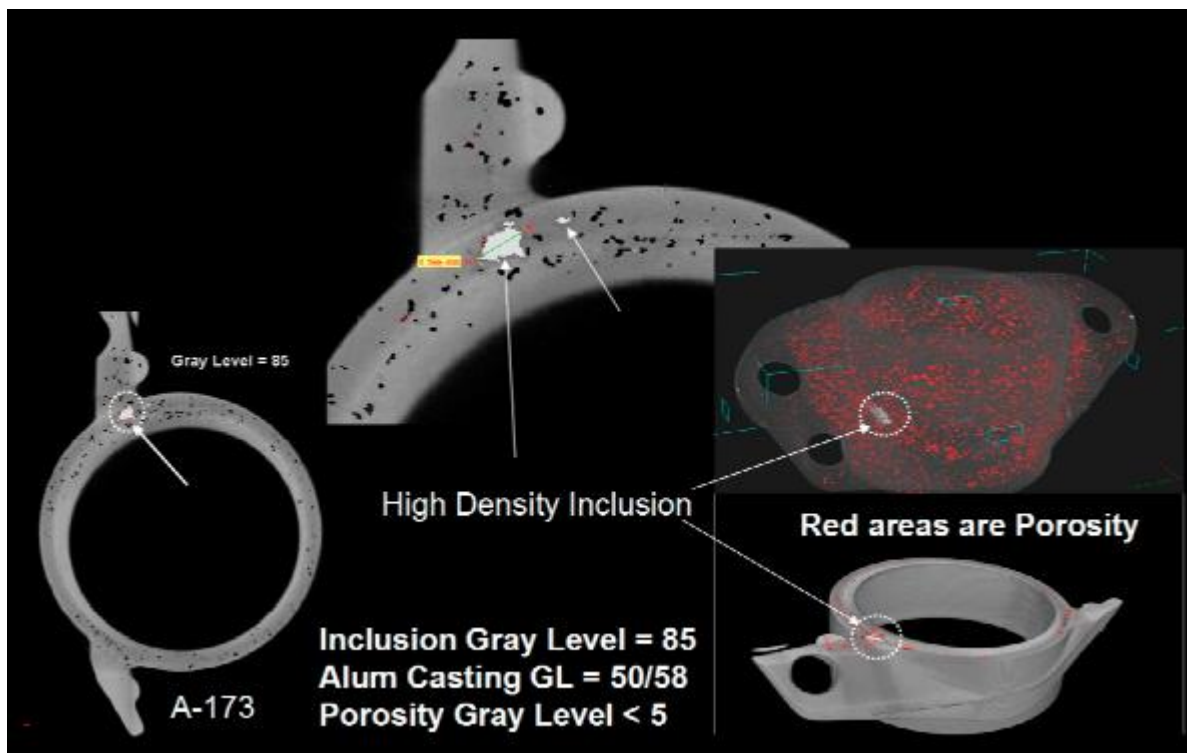
Figure 2-24 shows analysis of pours in an aluminium casting, taken from (Wells J. M., 2007)

In their work Wells was able to demonstrate in a series of aluminium alloy castings that pores of varying size were present making up approximately 1.11% of the total volume of the casting., well within typical levels for porosity in a casting. Alongside this Wells was also to demonstrate the use of the same techniques to highlight inclusions in their casting.

As the widespread adoption of powder-based AM into industry continues, part structural properties are under scrutiny. Research in the field has included both destructive and non-destructive evaluation, to best understand how to apply the new manufacturing technology. XCT as a porosity analysis tool is uniquely suited to this field as not only can detailed analysis of the porosity of parts be carried out but also dimensional assessment. Measurements on inclusions and defects such as unfused powder can also be accomplished as was demonstrated by Ahmed Tawfik (Tawfik, 2021). In his doctoral thesis, Tawfik developed inspection techniques that are capable of further categorising internal defects, these methods were developed with AM in mind, such that defects approaching the size of individual particles of AM powder could be detected. Tawfik also demonstrated that the use of ISO50, a common method of surface determination as noted in section 2.7.1.1 was less suitable than surface determination methods optimised for defect characterisation.

2.8.2. Dimensional metrology

Dimensional metrology is the traceable measurement carried out in order to quantify the physical size and geometry of a given object. XCT has recently emerged as a method in the field with some researchers hailing XCT as the next generation of coordinate measuring systems (CMS). Whilst the potential of XCT is undeniable, it is not at on the level of traceable coordinate measuring machines (CMM) which are still the gold standard of dimensional metrology. The traceability and accuracy of XCT is currently not at a level where the technology can readily replace an CMM, though establishing the traceability of XCT is a major focus of current research (Ferucci, 2018). However, XCT does have the advantageous ability to non-destructively evaluate the internal geometry of objects. Currently this feature is unique to XCT, as other methods such as contact CMMs and microscopy require direct access to the surfaces.

Use of XCT for dimensional metrology began around 1989 with the analysis of wall thickness (Mitchell, 1989). Its use as a tool for dimensional metrology continues today, though the accuracy and scope of measurements have increased greatly. In comparison the accuracy of early scans was only around 0.1mm whereas some modern machines claim sub-micron accuracy (Kruth, et al., 2011) (AXT PTY Limited, 2021). Kruth et al. discuss the application of XCT as a tool for dimensional metrology, and how it compares to the established methods of optical and tactile measurement. They highlight a key difference of XCT in that it produces an estimation of the ground truth based on an integrative characteristic, a pixels grey scale value, to produce a volume representative of the original surface. This leads to the potential for partial volume artefacts, discussed in section 2.4.4.. Kruths review also notes a variety of factors effecting accuracy of a scan including some of those discussed in sections 2.4 and 2.5..
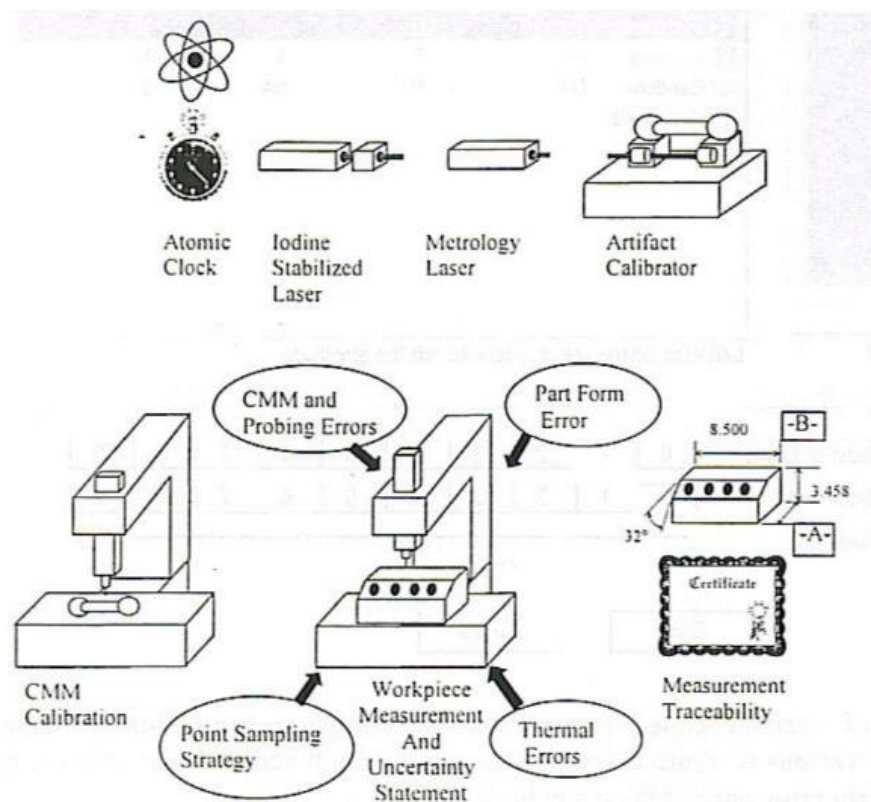
Figure 2-25 Traceability chain of a CMM, taken from (Summerhays, Baldwin, Campbell, & Henke, 2004)

As noted, traceable measurement is key to dimensional metrology. Traceability is the linking back of a measurement to a pre-defined standard. When observing the traceability of a contact CMM a clear chain can be seen back to the meter as shown in Figure 2-25. For dimensional metrology the predefined standard is the meter (m), which has been defined in several ways itself since its adoption. Since 1983 the meter has been defined as the length of the path travelled by light in a vacuum is a 1/299792458 of a second (Consultative Committee for Length, 2019). Prior to this the meter had been defined by a various methods including a set of "identical" physical bars and even as one ten millionth the distance from the equator to the north pole along a given path.

As discussed, the functioning principles of XCT are unlike any other methods of gathering dimensional metrology data, these differences in operating principles are both CT's main draw and main drawback. The penetrative capabilities of X-rays allow for new levels of non-destructive dimensional metrology

to be carried out. Though counteractively the use of X-rays as a tool for imagining and analysis of parts on a micro-level is a new relatively new application of the medium, as with any new application new obstacles are bound to occur. This has led to the traceability and calibration of XCT for metrology to be a high priority field of research for those in the field of industrial XCT. The paper Towards geometrical calibration of X-ray computed tomography systems—a review is focused on factors effecting establishing traceable measurement. (Ferrucci, Leach, Giusca, Carmignato, & Dewulf, 2015). In their paper Ferrucci et al. note that XCT has potential as a dimensional measurement tool specifically due to its ability to measure internal geometries non-destructively. Their paper then goes presents an in-depth analysis of the various factors that can influence geometric calibration. When looking at a cone beam XCT the geometry can be divided into 3 key components the X-ray source, the rotation stage, and the detector. Ferrucci et al. also demonstrate how various geometric errors can lead to shifts in XCT results. The paper notes how geometrical in accuracy in the detector can lead to errors such as those noted in section 2.4 the misalignment of the detector and source can lead to the appearance of ring artefacts. As previously noted in section 2.4.1, Ferrucci et al's 2015 paper also investigates focal spot drift, whilst not measuring it in detail, the effect of the thermal expansion is shown to cause spot drift with comparisons made between systems with and without external cooling.

Alongside the detector and source alignment the paper also investigates geometrical errors relating to the rotational stage are present and can result in errors during reconstruction and scaling. Tilt around the rotary axis or errors in radial motion around the axis are both examples of this form of error and can be seen in Figure 2-26.
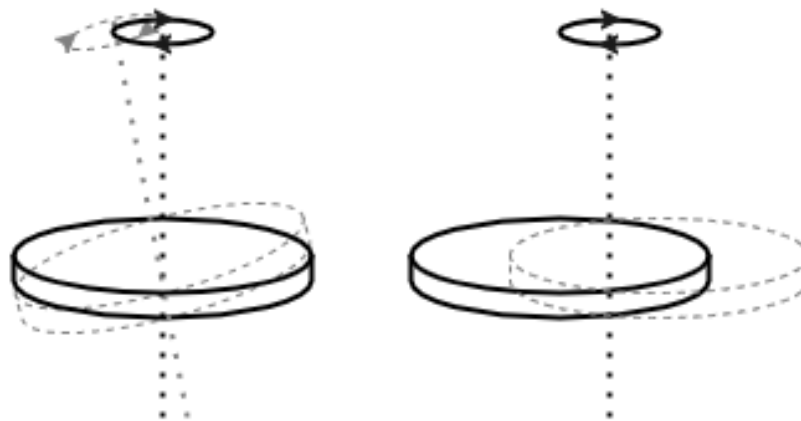
Figure 2-26 demonstrates tilt around the rotary axis (left) and errors in radial motion (right)

The authors reference work done by Kumar specifically their 2015 paper "Analysis of the effect of cone-beam geometry and test object configuration on the measurement accuracy of a computed tomography scanner used for dimensional measurement" (Kumar, Attridge, Wood, & Williams, 2011). And show images reproduced form Kumar's data.

These studies completed by Kumar et al. demonstrated how geometric errors at the source, the object and the detectors result in measurement errors of various artefacts. They authors were able to simulate errors individually at all three of these key points of the XCT, this is shown in Figure 2-27. From their results they demonstrate that geometric errors at the detector are less significant than errors of a similar magnitude at the source/ object.
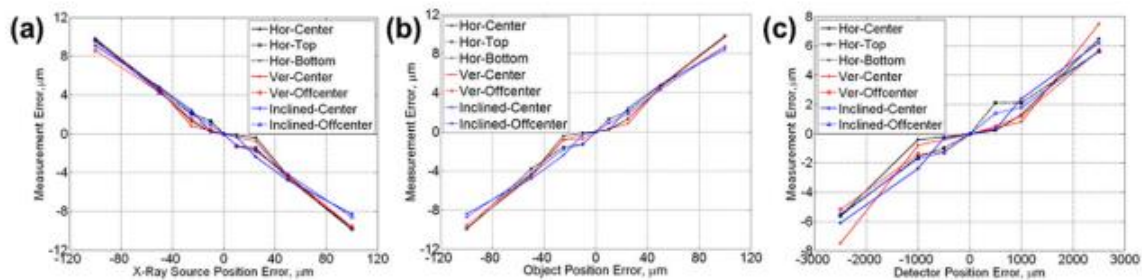
Figure 2-27 Kumars results showing how positional error at the source (a), object (b) and the detector (c) relate to measurement errors. Taken from (Kumar, Attridge, Wood, & Williams, 2011)

Another section of the same paper shows how different artefacts are affected by the positional error of the object itself. It is clear that as a result of inaccuracy in the alignment of the stage significant errors in dimensional measurements across a range of sample sizes can occur, this is shown in Figure 2-28.
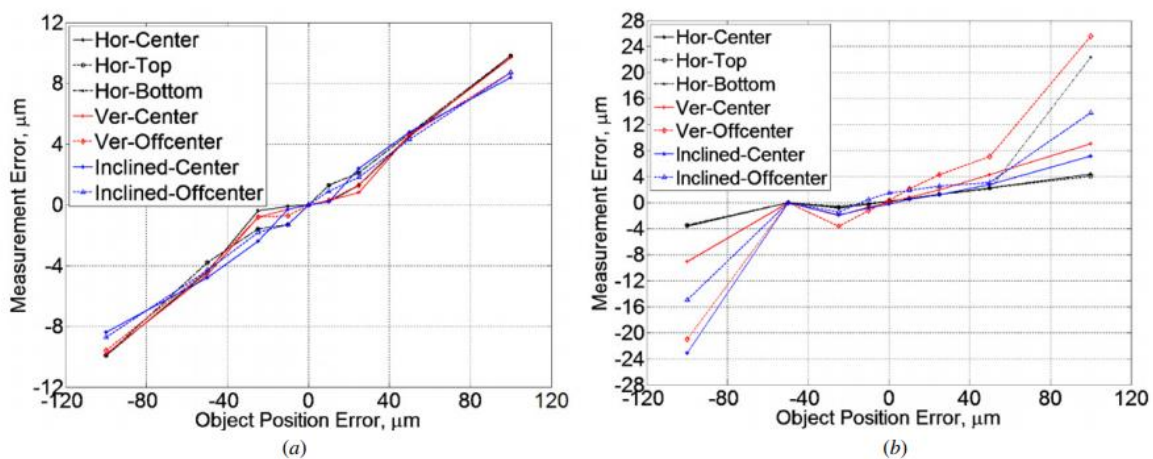
Figure 2-28 effect of object position errors for dimensional measurements of a 2mm (a) and 100mm (b) object, from (Kumar, Attridge, Wood, & Williams, 2011)

The work done by both Kumar and Ferrucci demonstrate that XCT is still in its infancy when being used as a method of dimension metrology, this is supported further when looking at the work presented in section 2.4.1 where various authors indicate that the focal spot is a particular feature that can cause error in measurements.

In the 2016 thesis "An investigation of the factors associated with the X-ray tube and their influence on dimensional measurement in micro-focus cone-beam industrial X-ray computed tomography systems" by Flay. Carried out a range of studies investigating how both the size and shape of a focal spot could influence the diameter and form error of various artefacts. They were able to demonstrate that an increase in the size of the focal spot resulted in a decreasing diameter of a spherical artefact

and found that an increasing focal spot also led to higher form error. This aligns with theory surrounding spatial resolution and the penumbra effect discussed in section 2.5.1. The author goes on to suggest that the categorisation of the focal spot should be done as part of the calibration of a system. The author concluded by suggesting future work is carried out looking at more complex samples with multiple materials or complex geometries.

When reviewing literature surrounding the use of XCT for dimensional metrology, it is clear that whilst useful work must be done to understand, categorise and solve issues, some unique to the process. When looking at section 2.4.1 in tandem with the work noted in this section, it is also clear that the focal spot is of key concern with work being completed at various institutions looking at both the measurement and effects of the focal spot.

2.8.3. Surface metrology

Surface metrology is the traceable measurement of a surface for analysis purposes. A number of parameters have been developed to categorise surfaces for different uses. These parameters can initially be split into two categories 2D profile parameters (prefixed with an R) and 3D areal parameters (prefixed with an S). Most parameters have an equivalent in the other category, for example Ra is defined as the average arithmetic mean height measured across a surface, Sa is the extension of this across a surface (British standards institute , 2012).

Profile parameters are the older category of surface measurement and typically require a significantly lower level of computation. The adoption of areal parameters marked a paradigm shift in surface measurement (Jiang, Scott, & Blunt, 2007). The advantages can be seen in Figure 2-29, where the two measurements can be seen in contrast.
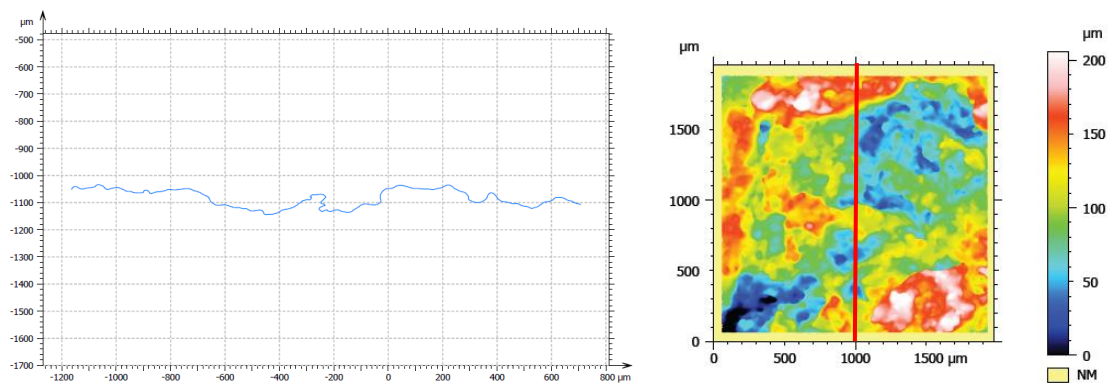
Figure 2-29 profile trace (left) and areal heigh map (right) taken from a XCT scan of an AM part. The path of the profile is *marked.*

The introduction of methods of extracting areal surface texture parameters from XCT scans of additively manufactured parts in line with existing standards governing such measurements was first demonstrated in 2017 (Townsend, Pagani, Scott, & Blunt, 2017). The procedure developed at the University of Huddersfield provided a method of data extraction where data was taken and processed as per ISO-25178 (International Organization for Standardization, 2012). This data was compared to measurements of the same metal AM surface taken using a focus variation microscope (Alicona G4), these comparisons showed little variation verifying that the results extracted from the XCT scans were viable. One point of note in this work is that during Townsends work there was a filament change carried out, a normal maintenance procedure, however after this there was a noticeable shift in results, this could be a possible source of error not previously considered. Though further investigation into this was deemed outside the scope of Townsends work.

2.8.3.1. Townsends method

The method developed by Townsend is used in depth in the authors work, as noted it allows for the extraction of data which adheres to existing standards (Townsend, Pagani, Scott, & Blunt, 2017). The method uses a combination of propriety and freeware software packages to produce .ply (polygon file format) files that are then converted into .sdf files using a MATLAB script. The process is explained in greater detail in section 3.3.6 where it is used in a study.

2.8.3.2. Advancements

Since the initial publishing of Townsends method, Digital Surf Mountains software has been update to allow the importation and analysis of both .ply and .stl files. This has decreased the time require to produce extracted area surface results from XCT scans (Digital Surf, 22).

2.8.4. Development of surface metrology for XCT

Development of methods to use XCT as a tool for the gathering of an areal surface texture parameters has also prompted the development of XCT specific parameters. Pre-existing surface parameters were not designed with re-entrant features in mind. Re-entrant features are features of a surface where the surface overhangs or goes back in on itself in a way that when viewed from above the true geometry is hidden. Features such as this are uncommon with most traditional manufacturing methods, however they are common in additive manufacturing (AM). Townsends method was developed around the use of XCT for analysis of AM surfaces, however it was developed to produce data in line with ISO 25178 and as such removes features that would not be visible to a line-of-sight measurement. This at the time of development was not an issue as existing areal surface texture parameters were as noted not designed to accurately evaluate them.

However more recent developments have seen the development of parameters that have been designed to evaluate these re-entrant features (Pagani, et al., 2019). Pagani et al. demonstrated that existing parameters cannot be used to accurately characterise surfaces with re-entrant features and presented a range of parameters developed specifically to evaluate surfaces that contained such features.

As noted the main advantage of XCT is its penetrative capabilities allowing analysis of features such as re-entrant features, internal geometries and surfaces. Alongside the work to produce parameters specific to XCT, work done by Thompson et. al. has demonstrated that XCT produces comparable to optical measurement systems, further to this showing that surface measurements of internal surfaces not accessible to the optical systems can be evaluated (Thompson, et al., 2017).

2.9. Summary of existing literature

Reviewing current literature, the major theme of the research is towards more accurate and traceable measurements. In the early days of XCT, more powerful sources and higher resolutions were identified as key goals, this is still seen in work today with ever increasing detector sizes and work being done to minimise focal spots size. These features have improved and other sources of inaccuracy are revealed such as the geometrical errors in the system itself, with some machines now existing with concession to these factors being available (NIKON METROLOGY, 2022). However if XCT is to become a new standard method for both dimensional and surface metrology as some have touted it, work must be done to quantify the sources of error, and offer methods of correction where possible. Work to do this has already begun, as seen in the literature with research showing how inaccuracies in the system can cause variation in measured results for both geometrical and surface analysis.

After reviewing the current literature in reference to the stated research aim of the project, the geometry of the machine itself has been shown to cause variation though it is understood how this variation may affect results. Work has been done on how variables in the electron tube can affect dimensional measurements, and research has been done to develop procedures specific to XCT to best optimise the process for measurement and analysis of surfaces.

XCT though is still not as accurate as measurement systems such as a CMM, and currently it should not be thought of as a full traceable measurement tool. Variation between scans of an identical surfaces have been measured and small changes in the machine have the have been shown to result in shifts in results.

2.10. Research aims and objectives

As previously stated, the aims of the authors research are to demonstrate how uncontrolled variables in the process of X-ray generation for XCT may cause variation which propagates through to extracted

surfaces and the areal surface texture parameters generated from them. Further to these correlations seen between identified variables and results should be further investigated as to establish possible methods of control or correction. Current research does not fully quantify several key factors of XCT with regards to the possibility that they introduce errors into measurement.

2.10.1. Objectives

The objectives as stated in the introduction to this work were:

- Identify uncontrolled variables in X-ray generation for cone beam XCT reviewing current literature to identify possible unknown sources of variation.
- Separate the variables into logical groups allowing for the development of studies to investigate any effects on end results (areal surface texture parameters), where possible variables should be isolated, but it is accepted by the author this may not always be achieved.
- Design and develop test methods for each variable starting at the beginning of the X-ray generation process and working through to complete surface data results.
- Quantify if variables introduce shifts in results that correlate with a measurable change in the variable, discussing where the variation introduced may prove significant.
- Where possible identify and develop possible methods of controlling or correcting error sources

Looking back at these after reviewing literature, the objectives stated fall in line with one of the current focuses of literature surround XCT as an industrial NDE tool.

3. The effects of variation and degradation of XCT emitter filaments

The filament, shown in Figure 3-1, as stated in section 2.2.2 a key electron gun element of the cone beam XCT. As discussed, the filament is the source of the electron beam and is a consumable, which degrades to failure after a period of use. This is primarily due to the high heat it experiences during use, working temperatures of a filament of 2700 K are common. As noted in the literature review Townsend et al 2017, reported during their study, that extracted areal surface texture parameters were seen to shift post filament change. A comparison showed a change of 0.95% Sq between data gathered before and after a filament change. The process of changing the filament was highlighted as a possible source of the noted variation in surface texture parameters, that could prove significant dependent on user requirement. It was thus hypothesised that variation between filaments was a contributing factor towards the noted variation and as such needed further clarification.
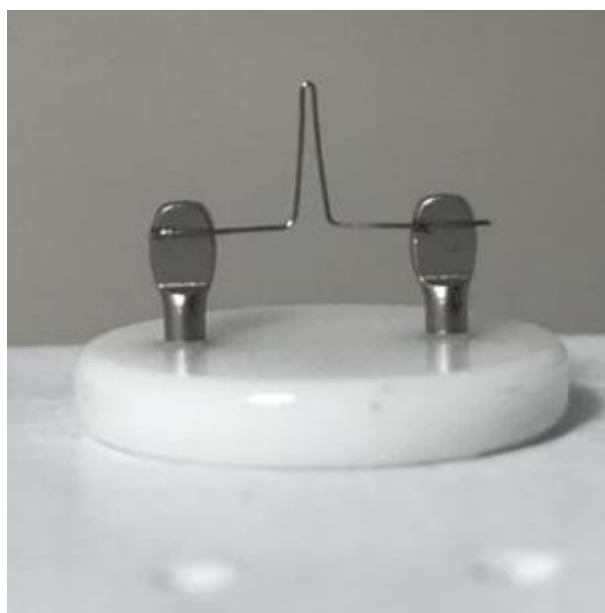
Figure 3-1 an XCT emitter filament before use

Filaments are drawn tungsten wire, jig formed, to produce the shape seen in Figure 3-1. The filaments are then welded onto a frame and then heated in a vacuum to reveal defects and relieve stresses imparted during the welding process (Agar Scientific Ltd, 2014). In XCT, the filament is used to generate free electrons via thermionic emission, these are focused into an electron beam using a combination of a negatively charged focusing cup (Whenelt cylinder) and electromagnetic coil. The beam is accelerated towards a target using an anode and cathode arrangement, as well as negatively charged focusing cup (2.2.2). Upon impacting the target, X-rays are produced via one of several possible interactions as detailed in section 1.6. Whilst the filaments are produced to a tolerance, it was hypothesised based on Townsend's work, that even small variations in geometry, surface condition or material composition that are permitted in the manufacturer's tolerances may influence the emission and go on to propagate through to variations in the extracted surface texture parameters. These variations could be exacerbated by minor damage in transport and installation due to the fragile nature of the parts. These variations were thought likely to be the significant to the variation initially noted by Townsend in 2017.

To investigate the hypothesis, a research exercise was developed where first, mathematical theory on thermionic emission was studied to evaluate whether it supported an investigation into differences in scans between individual filaments and across the life of a filament. If theory supported this, a study

would be conducted into how variations between filaments would affect areal surface texture parameters in orders to establish a pattern. Second to this, investigations were carried out into the variation inherent to filaments, such as varying geometry, materials composition, or possible defects at the emitter tip.

3.1. Thermionic Emission Theory

During use, the tungsten filament of an X-ray gun is held in a vacuum and current is passed through it. This current causes the phenomena of joule heating, which is a result of the inherent resistance of the tungsten. With a suitably high current the part can reach extreme temperatures, for a working filament these can exceed 2000 K. At higher temperatures the filament will start to emit electrons from its surface, this is known as thermionic emission. The intensity of thermionic emission varies dependent on material characteristics, for tungsten whilst mild emission occurs at lower temperatures, significant emissions does not occur below 2000 K as seen in Figure 3-2.
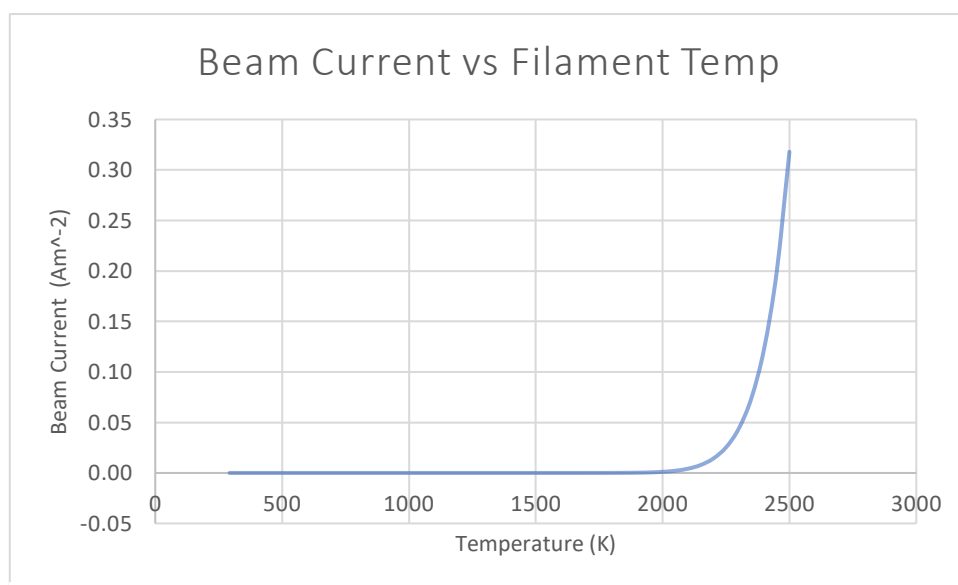
Figure 3-2 demonstrates how beam current is dependent on filament temperature

Electron emission is measure using emission beam current (J). This is calculated using Richardson's law shown as Equation 3-1, developed by Owen William Richardson after J.J. Thomson had identified the electron as the emitted particle in thermionic emission.

$$J = A_G T^2 e^{\frac{-W}{kT}}$$

Equation 3-1

Where T is filament Temperature, W is the material work function and k the Boltzmann constant. A_G is given as:

$$A_G = \lambda_r A_0$$

Equation 3-2

λ_r is a material specific correction value and A_0 is a constant calculated as:

$$A_0 = \frac{4\pi m k^2 q_e}{h^3} = 1.20173 \times 10^6 \, Am^{-2}K^{-2}$$

Equation 3-3

Using m and $-q_e$ as the mass and charge of an electron with h as Planks constant.

It is of note that Thompson's discovery of the electron and subsequent identification of it as the particle emitted during the thermionic emission process, closed a small chapter of research on what the previously unknown emission was. He would go on to discover Thompson scattering a nonrelativistic equivalent of Compton scattering this is discussed in section 1.6.2 (Hickson, 2015).

Temperature is the only non-constant or material specific variable in Richardson's equation. As the temperature of the filament is the result of Joule or Ohmic heating, the resistance of the wire will have a direct effect on the emitted electron beam. This heating will also cause sublimation (the vaporisation of material at the surface layer) at the surface of the filament, the rate of which, increases due to higher vapour pressure at the increased temperature (Szwarc, Plante, & Diamond, 1965). This degradation of the filament during its life results in decreasing cross sectional area (Wilson, 1956). As the cross-sectional area of the filament changes so its resistance as will be seen in Equation 3-4. Resistivity of a material is also temperature dependent (Jones, 1926). As the temperature increases the resistivity will also increase this will again affect the resistance of the filament as described in Equation 3-4.

$$R = \frac{\rho L}{A}$$

Equation 3-4

Where

R is electrical resistance

A is cross sectional area

L is length

As current is set by the user, as the resistance of the filament changes so will the voltage across the filament, this could be calculated using ohms law (Equation 3-5)

$$V = IR$$

Equation 3-5

Where V is voltage

I is current

R is resistance

Joule heating is defined using Equation 3-6, where P is power converted from electrical to thermal energy, I is current and V_a and V_b represent the change is voltage over the area the heating is being measured.

$$P = I(V_a - V_b)$$

Equation 3-6

Equations 3-4, 3-5 and 3-6 together can be used to show that as filament diameter changes with a constant current voltage will also vary. Any variation in voltage across the filament would result in variation of the power converted from electrical to thermal energy. This change in thermal energy would be represented as a change in temperature. As previously stated in the Richardson's equation

(Equation 3-1) temperature is the only non-material specific variable. It is clear that Equation 3-1 through to Equation 3-4 support the hypothesis that any variation in the filaments diameter would subsequently effect the temperature of the filament and therefore the emitted electron beam. Changes to the electron beam intensity will affect the focal spot, the point of X-ray generation, section 2.5 shows in detail how variation at this focal spot can affect a CT scan. This supported the initial hypothesis and was used to justify a physical study. The initial hypothesis was also expanded due to investigation into the theory behind thermionic emission. It was now hypothesised that the variation in extracted surface texture parameters between new and old filaments resulted from the degradation of the filaments condition and that an observable trend in extracted areal surface texture parameters would be seen over multiple filaments life. Though it was not known what form this trend may take.

3.2. Filament Properties and Material Choice

Tungsten is the most commonly used material for the emitter filament due to a combination of its material properties, shown in Table 3-1, this makes it an ideal candidate material for use in electron beam generation. Of all metals in pure form, tungsten has the highest melting point, lowest vapour pressure and lowest thermal expansion properties of any pure metal. Additionally, it is also very strong in tension (Szwarc, Plante, & Diamond, 1965).

Table 3-1 material properties of tungsten (W), (matweb, 2022) (Ed Fagan Inc., 2020)

Melting point (°C)	Thermal Expansion @20°C (ppm/°C)	Tensile Strength @1650°C (MPa)
3410	4.6	172

As outlined above, electron beam generation will only take place at extreme temperatures, thus it is important that a filament is made of a material that can withstand these temperatures. Vapour pressure relates to the stability of materials at the boundary layer, a low value means the compound's molecules bond well (Letcher, 2007) whereas a higher value of vapour pressure would be seen in more volatile materials. At higher temperatures, vapour pressure rises thus a material such as tungsten with a low value will remain more stable at the high temperatures required for filament operation (Speight, 2010). As a filament is heated its expansion is mirrored in the geometry of the emitted electrical field and beam, as thermal equilibrium is reached, the beam will then stabilise (Southall, Kagarice, Thron, Canepa, & Mackie, 2006). Due to the low levels of expansion of tungsten these effects are minimised, and it is therefore considered an ideal material for use as a filament.

Due to similar operating principles, the filaments found in many cone beam electron tube based XCT cylinders are identical to those found in scanning electron microscopes (SEM). In both machines the filaments are generally held in a Wehnelt cylinder, a negatively charged cap surrounding the filament with an aperture to allow a controlled flow of electrons through. Due to the negative electric charge of the cylinder the process of thermionic emission can be localised to the tip of the filament by supressing the emission of electrons elsewhere on the cathode. Combining this with the application of Richardson's law (Equation 2-1) an electron beam of known energy can be produced. This beam is emitted from the filament through the aperture of the Wehnelt cylinder which doubles as a convergent electrostatic lens preventing the electrons naturally dispersing. The beam is then drawn to an anode placed in alignment with the aperture.

In scanning electron microscopy alternative filament materials are more frequently found, two common alternates to tungsten are Cerium Hexaboride (CeB_6) and Lanthanum Hexaboride (LaB_6). When comparing tungsten to CeB_6, significant advantages can be noted.

3.2.1. Image brightness

Brightness in SEM is measured as amperes per unit area, a tungsten source at a given imaging setup would provide 106 A/cm^2 (Amperes per centimetre squared). The work function of CeB_6 is significantly lower than that of tungsten around 2.5eV compared to 4.5eV, this provides the two-fold advantage of a higher beam current at lower temperatures thus a much brighter image at all acceleration voltages. For SEM this provides a further advantage of a higher current in a similar sized focal spot and a higher imaging resolution.

Cerium Hexaboride and Lanthanum hexaboride are both alternative filament materials commonly used in SEM, they are even better suited to use in SEM electron guns than tungsten as both can produce a higher beam current for a smaller spot size, typically being 10x brighter, whilst also providing a much longer service life (ThermoFisher Scientific).

3.2.2. Emission temperature

Both Lanthanum and Cerium Hexaborides have much lower operating temperatures than equivalent tungsten workpieces around 1800 K compared to >2000 K for tungsten. This results in a lower energy spread for the hexaboride filaments which when relating to SEM allows for better image quality at much lower acceleration voltages. The lower temperatures again also allow for a much longer operating life. All factors included the typically CeB_6 filament may last upwards of 1500 hours scan time. (ThermoFisher Scientific)

3.2.3. Summary of alternative filament materials

Whilst little research has been carried out into the installation and use of these alternate filament materials in XCT. The potential benefits of using them warrants investigation, study of this is however outside the scope of this body of work.

3.3. Filament degradation study

Mathematical theory regarding emission of electrons supported the hypothesis that filament degradation resulting in changes to extracted roughness parameters (Townsend 2017) via fluctuating X-ray levels. A testing method was devised to monitor changes in areal surface texture parameters generated from surfaces extracted from XCT as a function of filament condition.

3.3.1. Artefact

The artefact used in the study was a 10 mm x 10 mm x 10 mm additively manufactured cube made from Ti6-4, the cube was not subject to any finishing methods that may have altered the surface from an expected relatively rough AM surface. A face was selected at random for all scans to be taken from, this was carried out by numbering the surfaces 1-5 and generating random number to select the surface. The bottom face of the artefact, relative to the orientation during manufacture, had support structures and was discounted from being the selected face.

In this study the method of data extraction from XCT scans used was that developed by Townsend et. al. this is discussed in further detail in section 3.3.6. It is of importance for this section that Townsends method states that all scans of the same surface are to be aligned to a common master during data processing. Alignment of all surfaces to a common master ensures that the same area of a surface is analysed for each scan allowing easily repeatable measurement of the same surface data. By minimising the difference between raw scan data this step can be optimised.

To ensure that the artefact was kept in place between scans a jig was produced using FDM (filament deposition modelling), this jig was designed such that the artefact could be placed in the same orientation each time a scan was taken, thus minimising any difference between each data set. The work holding jig was designed such that the artefact would be held with the face of interest at an angle relative to the Machines Z Axis. The stem of the jig was designed to fit into the manipulator of a Nikon 225 XT-H machine, this arrangement can be seen in Figure 3-3
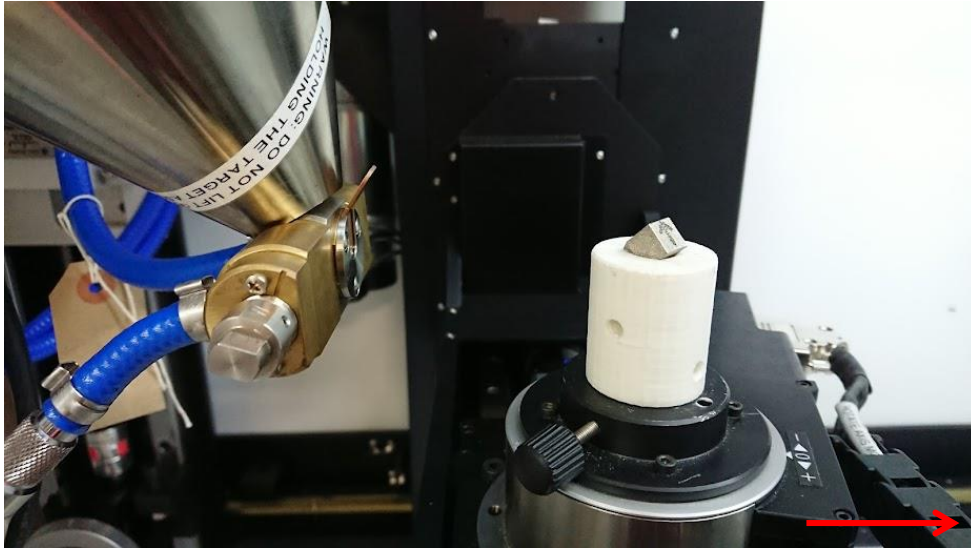
Figure 3-3 shows the artefact and jig in situ in the machine, the machines Z axis is noted by the red arrow.

The manipulator in a Nikon XT H 225 has an adjustable captive bolt, shown in Figure 3-5, that can be tightened to hold items in place during scans. Many of the standard Nikon stages provided with the machine have a keyway cut into them that this bolt interfaces with meaning consistent alignment withing the machine, this is seen in Figure 3-4. This keyway was copied in the design of the jig.

Figure 3-4 shows the underside of the standard Nikon stage, note the keyway on the left of the cylinder.
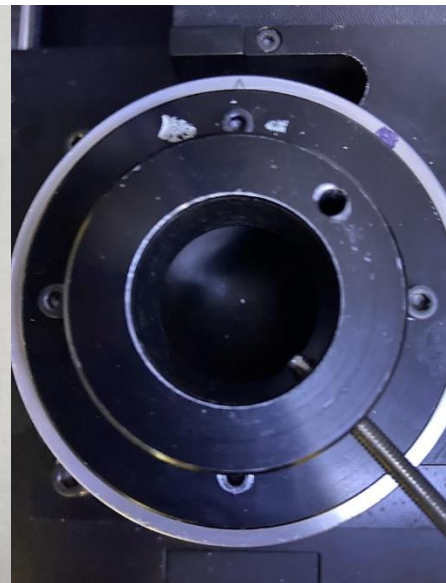
Figure 3-5 showing the manipulator mounting on a Nikon XT H 225, the captive bolt can be seen in the bottom right of the image.

As noted in section 3.3.6.4, Townsends method of data extraction already features an alignment procedure to ensure that when processing multiple scans of the same area, it is the same area that is

analysed each time. The use of a jig that interfaces with the existing stage present in the Nikon machine along with the jig holding the workpiece in the same alignment, ensures the artefact is in nominally the same place during each scan. By starting from an approximately identical starting position, the alignment procedure detailed in section 3.3.6.4 is optimised. As less data manipulation is required. Starting with a well aligned sample meant less chance of error thus meaning the same region of interest was analysed in each scan increasing the methods repeatability.

3.3.2. Data collection

Data collection was handled via two protocols designed to test slight variations on the hypothesis, a periodic scanning method designed to account for variation in results due to multiple users and a second consecutive scan method allowing for in depth study of changes in a small period of scan time.

3.3.3. Periodic scanning

The first protocol utilised was periodic scanning this was implemented to account for the possibility that the rate of filament degradation would be significantly affected by the range of scanning parameters that result from multiple users and projects on a multiuser lab based "working" XCT machine. It was thought likely a high-power scan requiring more work from the filament may result in larger variation of surface texture values because of the higher rate of change at the filament surface due to increased rates of sublimation and higher vapour pressure (Plante & Sessoms, 1973). Scans were to be taken after approximately every 20 hours of scan time, some scope was allowed as scan times are often not exact to the hour. Nikon 225 XT-H machines have an inbuilt filament lifetime clock to show the time in use allowing users to track the filament's use, this can be particularly advantageous in preventing long scans being set up only to find the filament has failed during the scan due to it having already seen extensive use. This clock was used for the study to allow scans to be taken at approximately 20 hour intervals. Scans by other users were logged to provide an idea of the demand put on the filament and as a second set of time stamps for the study. The removal and reinstallation of the artefact in the machine introduced the possibility of positional errors into the data. The jig described in section 3.3.1 along with the alignment stage of Townsend's method described in section 0 both are present to mitigate misalignment errors.

3.3.4. Continuous data gathering

The second protocol was a continuous data gathering method which set a batch scan to run for 120 hours with no outside influences. Nikon 225 XT-H has a batch scan function allowing scans to be queued without an operator being present meaning external variables were minimalised. The continuous method operated on a slightly different hypothesis that user demand and associated parameters on the filament would not be as significant an influencing factor on resulting areal data as general degradation over period time. The 120hr period was determined as a result of the first filaments failure after 120 hrs of scanning. It later proved advantageous that this limit was set as a close to failure filament was recovered and later analysed using SEM (3.6.2) for a different study.

3.3.5. Scanning parameters

For both protocols identical scanning parameters were used, these are detailed in Table 3-2, each scan of the artefact took approximately 3.3 hours to complete meaning that in all 106 scans were taken totalling over 350 hours of scan time across 4 filaments. The scanning parameters were decided upon by an experienced user using the histogram generated as discussed in section 2.3.

Table 3-2 scanning parameters used for filament degradation study

Voltage (kv)	160	**Power (w)**	9.9
Gain (dB)	12.0	**Magnification**	10.4
Filter thickness (mm)	1	**Filter Material**	Copper
Exposure time (ms)	4000		

3.3.6. Data processing for surface extraction

Data processing was carried out in accordance with the methodology developed by Townsend et al (Townsend, Pagani, Scott, & Blunt, 2017). This method produces surface topography data adhering to existing standards (ISO25178) for areal surface data extraction. ISO 25178 defines process for line-of-sight areal measurements such as focus variation microscopy. The use of this method allowed for the comparison of surface data results with those previously reported in Townsend's study, which first noted the variation being investigated. The method also allows comparison with established metrology instruments by removing any re-entrant features present, as these features are not detectable using standard areal methods. By removing the features, it provides a like for like comparison when observing results. Removal of these features, however, negates one of the clear benefits of using XCT, though it was not up until more recently that parameters were developed that could accurately quantify these undercuts and re-entrant features. It is also important to note that as XCT is still in its relative infancy in the field, comparison to more established methods is a required benchmark in establishing the validity of the method and the ideal operating range of the technology. This method is detailed in full below.

3.3.6.1. Export data

The method requires data in an .stl (stereolithography) file format. To achieve this, scans must be reconstructed, and surface determination performed. Reconstruction and surface determination can be carried out in a number of ways depended on the user's system. For a Nikon 225 XT-H reconstruction is performed in CTPro, a proprietary software for Nikon machines. Reconstructed scans were then imported into VG Studios Max where surface determinations was carried out. Once XCT scans are reconstructed, and surface determination performed the files were exported from VG Studios Max as an .stl (stereolithography) file.

3.3.6.2. Trim data

XCT data comprises of a full 3D model representative of everything within the scanning envelope at the time the scan was initiated. To lower the processing time required, data is trimmed to remove any data that is not required in future analysis. Data was trimmed in MeshLab a free mesh editing software. To minimise processing time all faces that were not to be measured were removed at this point. A small boundary was left around the measured face to prevent useable data being lost at this stage. Alongside this trimming an inverse line of sight selection normal to the measured face was used to select all hidden and re-entrant geometry, this was also trimmed and the data repaired using an interpolated fit algorithm in MeshLab. This step left the data similar to that expected of a line of sight measurement.

3.3.6.3. Convert to .ply

.stl and .ply files are both common formats of 3D mesh files, however .ply files are approximately 30% the size of .stl files. This is due to .ply files containing only vertices and not a triangular mesh. This conversion again lowers the processing time required. MeshLab can convert a .stl file into .ply file format, after data was initially trimmed this was carried out to decrease data processing time.

3.3.6.4. Alignment

As noted in section 3.3.1 all surfaces are aligned to a common master, this master was selected at random from the original data. Alignment was carried out in Cloud Compare a free software package allowing the editing and comparison of multiple meshes simultaneously. The master surface data was loaded in and denoted as such to prevent confusion. For the Townsend's original study, the focus variation surface measurement was used as the master, for this work a surface was selected at random. Once the master was clearly marked secondary data sets were then imported into the same session.

Registration or alignment is a 2-stage process. The first stage is a point alignment where common points are selected on both the master and aligned surface, a minimum of three points are required for 3D data sets. The user found that placing points on prominent surface features increased the speed and repeatability of the process. The selected points are then matched with the aligned surface being translated onto the master, so the corresponding points match on both surfaces.

Secondly a fine registration alignment algorithm in Cloud Compare (least squares regression) is used to accurately align the surface and master, this provides a more accurate alignment of the aligned surface to the master with iterative small changes made till a best possible alignment between points is achieved.

3.3.6.5. Crop data

Once the data is aligned to a master it is then cropped in Cloud Compare, this crop is done using a given distance around a predefined central data point, in this case the centre of the master data, This crop leaves only the data to be analysed for surface parameters. This is done to reduce processing time and computation requirements. Once this crop is performed the data is saved as .ply.

3.3.6.6. Convert .ply to .sdf

The XCT data in. ply format is then converted to .sdf files that can be imported into SurfStand. This conversion from a heightmap to a point cloud was done using a MATLAB script that performed a linear interpolation and projection of the data onto a plane. .sdf files allow for the extraction of areal surface texture parameters in Surfstand.

3.3.6.7. Surface parameter extraction

The .sdf files are then and processed opened in Surfstand, a surface analysis software that allows for the generation of surface texture parameters. The data is then filtered in line with ISO 25178, for the artefact used this required a Lambda F cut off filter of 8 mm to remove form deviation (British standards institute , 2012). The Lambda S filter was set at 25 μm to removal optical spikes. By filtering the data in line with the standard it is treated as data from other surface metrology equipment allowing comparison to more established measurement methods.

3.3.6.8. Possible error sources

Townsends method of data extraction included various sections which may lead to the introduction of both systematic and random errors. When initially performing the trimming of data, the selection of data to be removed/kept is done by the user, it is possible that human error could be introduced at this stage.

In Cloud Compare two sets of data are present in the same session to allow for alignment, it is possible to confuse these data sets for one another leading to the master data being saved as the aligned data set again introducing human error. The risks of this error can be minimised by ensure data sets are clearly labelled, it is also possible to assign a colour to a data set this can be used to highlight the master data set and prevent confusion.

When defining the input data used to crop the aligned surface in Cloud Compare it is important the inputs are calculated correctly, this is done by the user. Data can be saved so that subsequent crops are done using identical parameters however if the initial inputs are incorrect there is a possibility that a systematic error is introduced.

There is also potential that the algorithm for repairing the meshes and alignment of the surface introduced errors. Both MeshLab and Cloud Compare label the methods used with a relevant title that give an explanation of the process i.e. the fine registration in cloud compare is described as least square regression in the software however the exact algorithm used is not available, it is possible this algorithm introduces an uncertainty into the data.

In summary Townsends method contains various points where possible errors may effect data, however most of these can be eliminated by the user making sure to follow the steps and taking care to ensure they do not introduce the noted errors. It was thus deemed suitable for use in the study.

3.3.7. Filament Degradation Study results

Initially scans were processed at 20-hour intervals for each filament's data set, this was done to minimise processing time and establish if a clear pattern was immediate between the extracted areal surface texture parameters and the filament age. After extracting a useable surface using Townsend's method a range of areal surface parameters were generated using SurfStand software for each data set. Scan sets 1,2 and 3 used the continuous data gathering method and "scan set partial" was the only one to use the periodic method.

Initial analysis showed no trend across the life of the filament. Variation between the scans taken at 20-hour intervals appeared random in nature, as can be seen in Figure 3-6. The initial hypothesis that areal surface texture results taken from different filaments would at the point of installation would be tightly grouped was proved false. Results extracted near the end of a filaments life did not follow a pattern when comparing results from differing filaments. Scans taken at 20-hour intervals during the
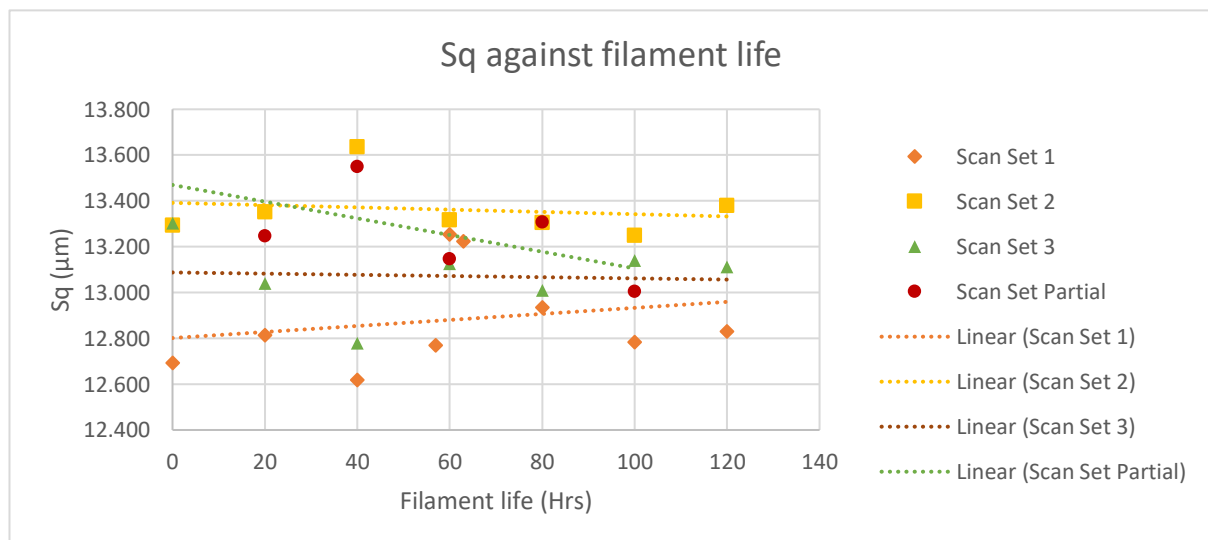
Figure 3-6 shows variation of Sq over the life of 4 filaments

filaments life also did not follow a pattern, variation in areal surface texture results appeared random. Comparing results from the periodic and continuous scanning methods indicated that random use of the filament between scans of a known surface did not introduce significant variance.

The lack of a clear trend in areal surface texture parameters across the life of a filament and the noted variation between filaments lead to the conclusion that the initial hypothesis was null. Variation seen between scans taken using the same filament when compared to the variation in scans taken using different filaments was at a lower level. All results presented were in keeping with Townsend's initial findings that variation was greater between filaments. This was noted for further investigation to be carried out. Sq or root mean square height is the root mean square of the ordinate values in the given surface area. It was seen to be indicative of the seemingly random variation displayed across the range of parameters tested. To ensure that results were consistent across different parameters Sa was plotted (Figure 3-7), the pattern seen in data matches the rises and falls seen in Sq (Figure 3-6Figure 3-7). As Sa and Sq are derived similarly (surface parameter definitions can be found in the Appendix in section 8.2), it is expected that they will follow a similar trend over a period of time. A range of other parameters, Ssk, Sku and Sz were plotted, to investigate whether other parameters followed a more obvious trend over a filaments life, these can be seen in Figure 3-8 through Figure 3-9. From the data it can be seen the unpredictable variation is still present though there is again no trend across all data sets across a filament's life.
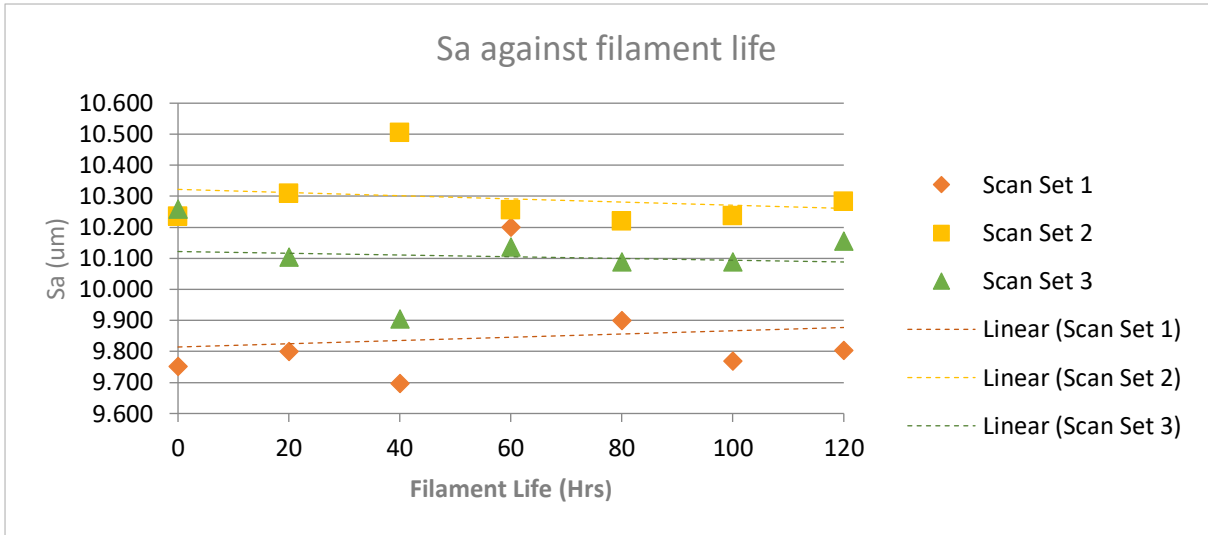
Figure 3-7 shows Sa against filament life the rises and falls in data values can be seen to correspond to the data in Figure 3-6
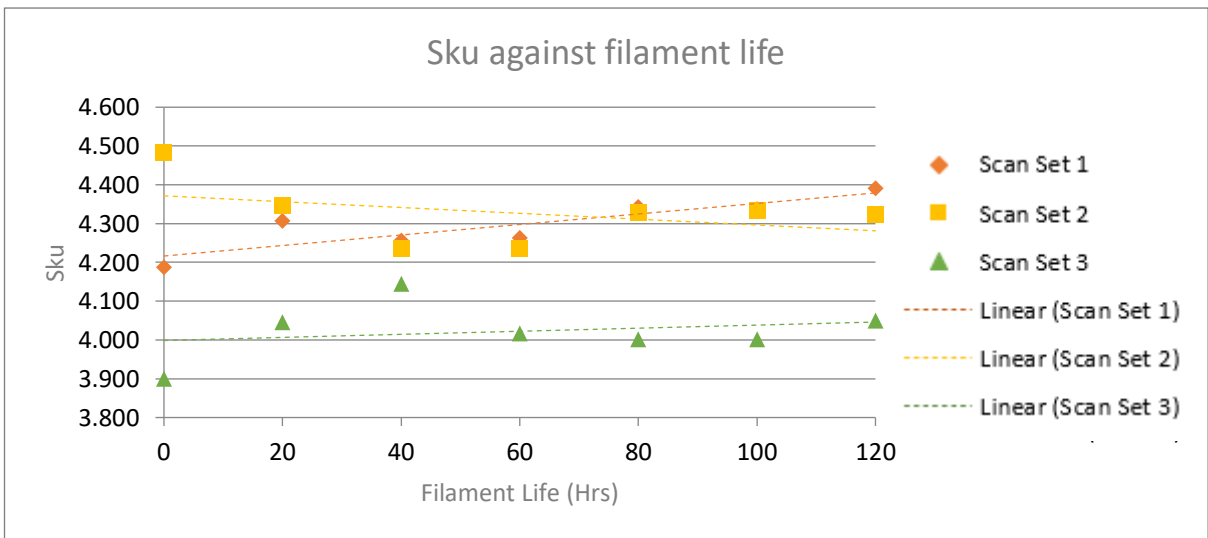
Figure 3-8 Sku against filament life, whilst there is variation in the results there is no distinct trend over the filament life.
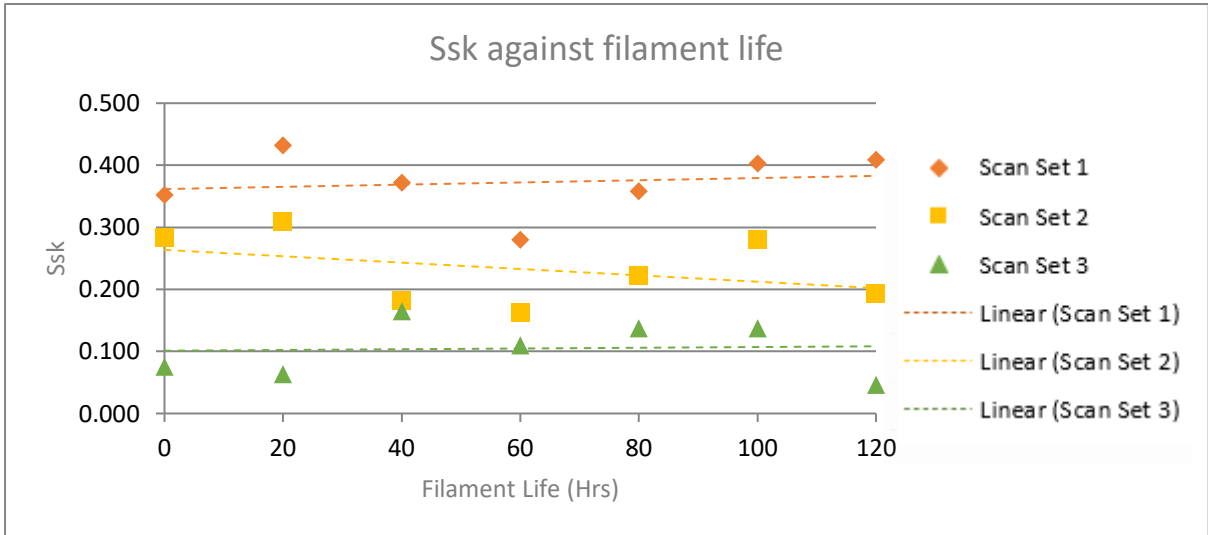
Figure 3-10 Ssk against filament life, this again shows variation in parameters that does not follow a trend during the filament's life.
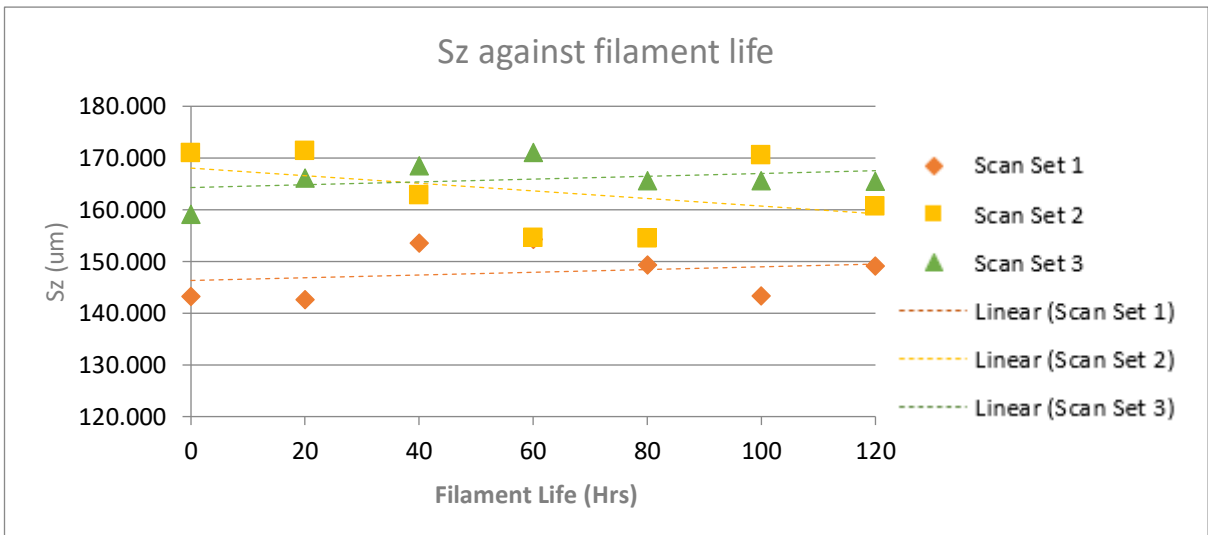
Figure 3-9 Sz against filament life, whilst there is variation in Sz it again does not follow a trend as the filament degrades.

3.3.8. Scan to scan variation

After initial analysis did not indicate a trend, all remaining data was processed in line with Townsend's method. The full data set, compiling of over 90 scans across the life of 3 filaments represented approximately 360 hours of scanning. Again, a range of areal surface texture parameter were generated for investigation. Data taken using the same filament continued to follow a pattern where it showed less variance than when compared to data taken using different filaments. No trend could be seen across the life of the filament with rises and falls appearing random in nature.

On a smaller time scale it was noticeable that parameters extracted from scans taken consecutively tended to show little variation. Larger variation could be seen when comparing groups from different points in each filament's life, with changes in extracted surface texture appearing gradual. Though gradual rises and fall were more common there were few large jumps in extracted areal surface texture parameters.

The seemingly random nature of the fluctuations in areal surface texture data proved puzzling as no clear pattern could be discerned to provide a link to a possible cause. It was thought that the variation could be linked to the surface determination process, the method of deciding the boundary where the artefact surface is. Surface determination is calculated in VG studios by comparing the average pixel intensity of the scans where a value assigned such that and any value higher than that is considered air whilst any value lower is material. It was hypothesised that investigating the pixel intensity values of scans may correlate with the variation in areal surface texture parameters.

3.4. Pixel Intensity measurement method

3.4.1. Pixel intensity value

As no patterns had emerged across the life of the filament, it was thought that a correlation may be present between the extracted areal surface texture parameters and the pixel intensity values of the XCT scans, these are the values used for surface determination and are typically displayed as a histogram (Figure 3-11). In order to investigate this a methodology was developed to extract the average intensity value of a scan.
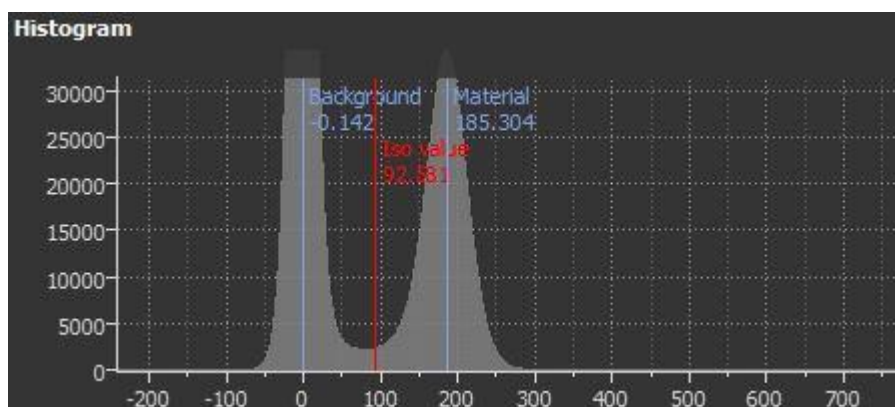
Figure 3-11 VGstudio histogram.

ImageJ is an image analysis software with a wide range of applications, it lends itself to automation with easy-to-use macro development tools and is thus ideal for analysis large stacks of images quickly.

The .tiff images produced using the Nikon XT-H 225 are in 16 bit greyscale format where values range from 0-65,536, each scan consisted of 1584 .tiff images in this format. Two regions were selected in ImageJ. The first region was an area of empty space where the average background or air value could be taken. The second region would be used to calculate the average intensity value of the part material. The regions were 100x100 pixels with locations chosen to prevent an overlap of the part or air into the other region, this process can be seen in Figure 3-12.
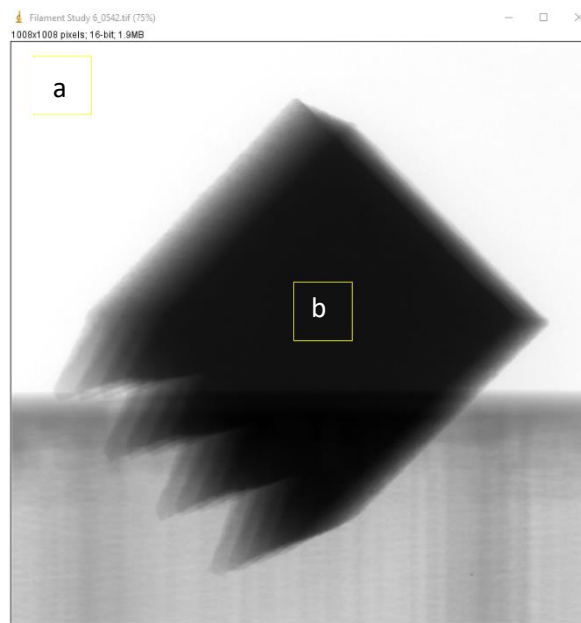
Figure 3-12 two regions for intensity value calculation, background (a) and material (b) the support structures noted in section 3.3.1 can be seen.

A macro was set up to repeat this process for all scans giving an average value for both background and material pixel intensity value. These values would be then measured against the extracted surface texture parameters to investigate if a correlation between the two value was present.

3.4.2. Pixel Analysis Results

It was immediate that again no clear corelation in trend was present between the areal surface parameters and any grey scale measurements, this is supported by the calculated correlation coefficients between the data sets shown in Table 3-3. This further added to the body of evidence disproving the hypothesis that the variation in extracted roughness parameters was due to a pattern of degradation during the filament's life.

Table 3-3 comparison of various pixel intensity values and Sq now clear correlation was present

Filament	1		2		3	
	Part vs Sq	Air vs Sq	Part vs Sq	Air vs Sq	Part vs Sq	Air vs Sq
Correlation Coefficant	0.010704	-0.29766	0.225715	-0.0563	0.343956	0.018533

3.5. Conclusion of degradation study

When investigating the initial hypothesis that filament degradation over its useful life was directly linked to the surface topography variation, first noted by Townsend, and shown in greater detail in this study. It has become clear to the author that the changes in extracted surface texture parameters, cannot be linked to the differences between a new and old filament as a significant and consistent change in results was not present. There is also a clear lack of correlation with any of the measured parameters when observing changes to extracted surface texture parameters throughout the life of a filament.

It is considered from the presented results, that the initial hypothesis of a clear link between filament age and extracted surface texture parameters is false. Due to a lack of correlation in the previous findings the focus of the work shifted to variation between the filaments prior to installation of the filament. As the greatest variation in results shown was between data gathered using different filaments, a new hypothesis was developed. It was proposed that the variation inherent between new filaments may be responsible for the variation seen in extracted surface texture parameters.

3.6. Analysis of inherent filament variation

A previously discussed in section 3 the filaments are a thin tungsten extruded wire welded to a frame with a ceramic shielding. The Agar A054X are according to manufacturer's specification 125μm in diameter, whilst no tolerances are specified for low diameter applications a tolerance of ±3% is common for drawn tungsten wire, though tolerances of as little as ±1% are possible. It is important to note when discussing thin wire (<0.5 mm) that the diameter of tungsten is measured by weight per unit length and the ±3% applies to this weight measurement (ChinaTungsten , 2009) (Elmet Technologies, 2021).

The delicate nature of the tungsten filament led the author to hypothesise that the noted variation in extract areal surface roughness parameters may be at least partially influenced by variation in the filaments which could easily be damaged. This hypothesis was again supported by the theory discussed in section 3.1, as a variation in filament would alter the resistance and thus the surface temperature and consequent electron emission.

3 key areas were highlighted for investigation the filament's diameter, surface defects and possible inclusions or other defects at the emission location.

3.6.1. Measurement method

To evaluate the filament emitter tip 3 measurement methods were selected SEM (Zeiss), confocal microscopy (Olympus Lext) and XCT. SEM and confocal microscopy would be used to analyse the surface of the filament and the tip, SEM EDX (energy dispersive X-ray spectrometry) analysis would also allow for the identification of any non-tungsten surface adherents to be identified. Though given the filament tip geometry, EDX analysis is only semi quantitative, for quantitative results samples must have a flat polished surface. XCT was chosen to allow comparison of 3D models of the filaments to compare geometric variation.

A new box of Agar AO54X filaments was acquired, and each was examined using both SEM and Confocal Microscopy, measurements focused on the tip of the filament, where useful emission takes place. Filaments were numbered to assure traceability. For the SEM, measurement would be set to use a magnification of 500 X, this led to a calculated image width of approximately 600.00 μm allowing a detailed analysis of the surface condition. Image analysis software installed in the SEM allows measurement between given points on an image using this calculated image width, though this method is not fully traceable.

Confocal measurement was to be used to analyse surface texture and any imperfection or inclusions on the surface, as SEM does not provide 3D surface data. Confocal scans were be set to 20 X and 50 X for each filament from directly above the filament. XCT was to be used to compare filaments geometrically by aligning each filament to a master and then comparing the approximate distance between points using cloud compare, this was later decided against as tests showed XCT filaments to small to accurately image in XCT. The alignment process (4.1.1) of filament installation compensates for some geometric variation.

3.6.2. SEM analysis

In Figure 3-13 draw marks from the extrusion process are clear and consistent across all filaments and a level of surface contamination is present on each sample to varying degrees. Though SEM does not allow for a true analysis of the debris that can be seen, as such, from these images the composition the composition and nature of the debris is unknown. It was however noted that the debris did not follow a pattern relating to the size or spread of the particles.
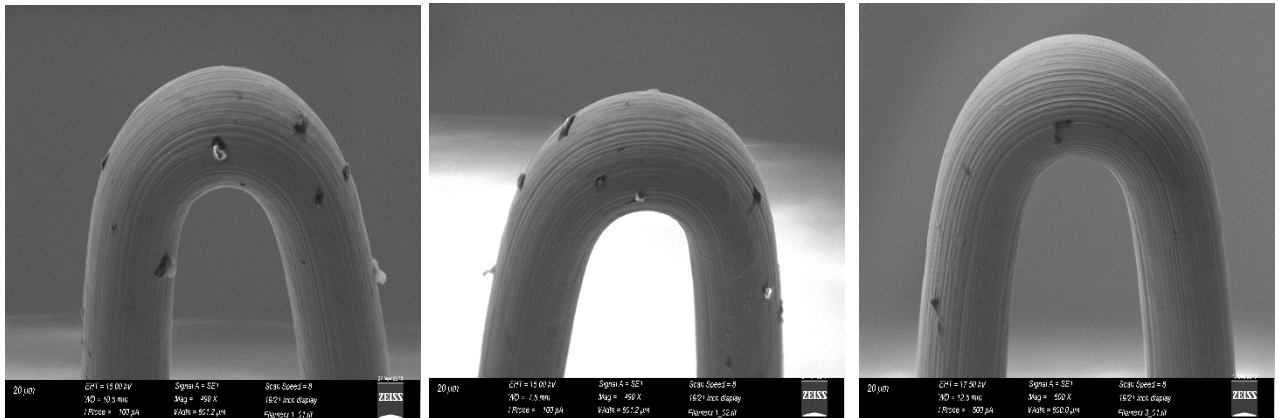
Figure 3-13 Comparison of 3 SEM images of new filaments

SEM combined with EDX allowed for a semi quantitative analysis of the material composition of the surface, this allowed for a more accurate idea of what the surface debris was. As can be seen from Figure 3-14 the filaments were shown to be largely tungsten with low levels of oxygen and carbon being commonly present. Some samples showed lower levels of various other elements such as silicon, sodium and iron. The EDX samples were taken during a separate session and using higher magnification, it was noted that many of the noted debris pieces were not present in the second set of scans, this led to the conclusion the debris was mainly loosely adhered dust particles (both organic and inorganic in nature) and not inclusions in the surface of the structure.
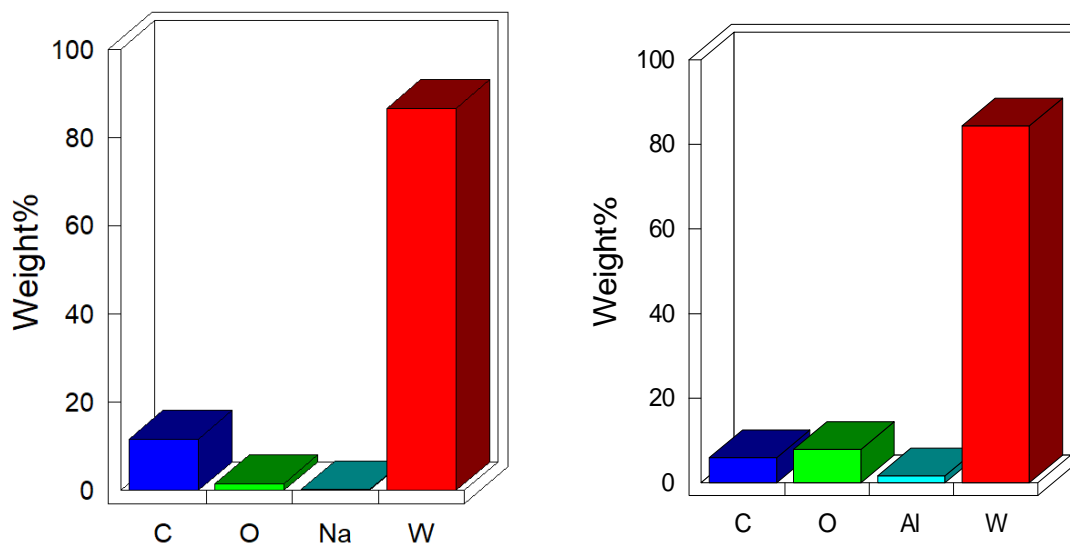
Figure 3-14 SEM EDX Material makeup graphs, these two examples were typical of what was seen across the set of ten filaments.

3.6.3. Confocal measurements

When observing the filaments using confocal microscopy it was again noted the surface debris was inconsistent when compared to previous measurements of the samples. Attempts to clean the filament resulted in bending the part. This evidence of the surface debris further supported the conclusion that the contamination was likely atmospheric dust and not surface inclusions, again draw marks from extrusion were present and consistent with the SEM imagery. 3D areal surface analysis showed that the surface debris was almost entirely raised above the filament surface, with few noticeable pores or imperfections in the surface itself.

3.7. Conclusions of Chapter 3

The work presented in this chapter further investigates the variation initially noted by Townsend in 2017 between filaments. The initial hypothesis presented was that the variation was due to the degradation of filaments during their useful life, this degradation being due to the increased sublimation rate of tungsten at high temperatures. When observing the mathematical theory behind thermionic emission, the process by which electrons are emitted from a filament in XCT, the theory supported the hypothesis. Mathematically the drop in filament diameter would result in an increase in emitted electron beam energy. An experiment was designed to measure the areal surface roughness extracted throughout the life of a group of filaments. By taking scans consecutively across the whole working life of a filament, it was hypothesised that as the filament aged a pattern would emerge in the results. The study would also provide the opportunity to investigate patterns in results across the life of a filament. The author hoped to assess whether a filaments degradation led to a predictable pattern or a drop in the precision or accuracy in areal surface texture results gathered from a less than pristine filament.

The hypothesis was shown to be false with no clear pattern throughout the life of the filament, variation in results remained seemingly random. It was also clear that the accuracy and precision of XCT over the life of a filament did not change with results near the beginning and end of the process showing similar levels of variation.

The data when analysed showed clear differences across the initial post installation scans. Consequently, a new hypothesis was developed that there may be significant variation between new filaments generated at installation. This was supported as results taken from different filaments showed more variation than those taken from a single part. It was also noted that later in the filament's life variation did not increase when compared to initial scans, indicating the degradation was not causing a significant sway in results. Alongside this, no pattern was noted during the life of a filament with results appearing to randomly shift from one scan to the next. As a result of this study, other factors surrounding the filament were considered and the focus of the work shifted to investigating these.

When considering the filament multiple variables were considered such as geometry, surface condition of a filament before and after use, and material composition. As geometry is somewhat corrected by the alignment stage of filament at installation, this consideration was left for further study. Surface condition and material composition were studied using a combination of confocal and scanning electron microscopy these showed that whilst some surface contamination was present both visibly and when material analysis was done using EDX there was no large-scale deformity in the surface of a new filament and the material composition of the filaments matched what was stated by the manufacturer. Whilst the material analysis did show some anomalies these were in keeping with the expected surface makeup of the part and general atmospheric dust. The filaments surface topography was in keeping with that expected of wire drawn tungsten with clear draw marks giving a uniform surface.

In summary

- New filaments do not appear to produce extracted surface texture results more precise than older filaments and accuracy does not undergo a pattern of change across a filaments life.
- Changes to extracted surface texture parameter do not show significant correlation with any measured variables including radiographic histograms or filament age.

- Variation of the geometry and material condition of box new filaments was not considered significant enough to warrant further investigation.
- Overall, the hypothesis that filament degradation over its useful life contributed to significant variation in extracted surface roughness parameters proved false.

4. The effects of manual focus variation on extracted areal surface texture parameters

It was clear after analysis of the results in Chapter 3 that the variations first noted by Townsend et al were not an anomaly and that areal surface texture parameters generated from XCT scans were subject to some inherent variation. Following the conclusions from the previous work shown in Chapter 3, it was clear to the author that no correlation between filament condition and extracted surface texture parameters was obvious when studying filaments throughout their useful life. Some variation was noted between new filaments however, this led to the investigation of other factors that could affect the emission of electrons from the filaments. Changes to filament geometry were more severe when comparing a new filament to itself after use, than were comparing two new filaments. Although theory showed that this would have an effect, the significance of the effect was deemed negligible compared to other factors. Surface condition and material comparison was investigated and were seen to be consistent across a range of new filaments, leading to them being discounted as possible influencing factors. The lack of factors linking the filament itself directly to the variation noted throughout Chapter 3 led to a new hypothesis. The variation noted at the point of installations was still greater than the average variation across a filament's life. However, as no clear and present link to the filament itself could be established a new line of investigation was opened. The process of installing a new filament in the machine is a complex set of procedures meant to optimise the filament for use in the machine. A filament must be aligned within a focusing cup, the cup must be aligned withing the electron tube itself and the filament must be conditioned, slowly brought up to an operating temperature, to ensure the best possible operating conditions. This set of processes introduces a group of variables not previously considered in the literature in terms of affecting extracted surface roughness.

The above considerations led to the study of the process of installing the filament into the machine, in this case it was hypothesised that the variation seen between filaments could be a result of the installations processes rather than the filament itself. The installation process includes a series of essential steps for optimal machine function and as such must be carefully completed at each filament installation. The largest variation noted in both Chapter 3 and Townsend's works was between filaments, all of which required installation via a defined procedure. Thus, it was thought possible that the variation may be because of influence of the installation process. A large variation caused by the installation process would indicate that it was not the filaments themselves responsible for the varying areal surface texture parameters, but the process of installation. As a consequence of this hypothesis the installation process and its effects are investigated in this chapter.

4.1. Installation process

The installation process of a new filament for a Nikon 225XT-H is described below, the machine uses a typical electron gun setup as described in section 2.2 in the literature review. When the filament is changed in an XCT machine, a process of focusing the electron beam onto the target is carried out and the demand on the filament is set. This allows the user to obtain the best possible scanning performance from the XCT machine. Where performance is defined as minimising noise, maximising scanning detail and facilitating results comparable to alternate metrology instruments. For the Nikon XT H 225 the process is detailed below.

4.1.1. Physical Filament alignment

The filament location in the focusing cup is important in establishing a useable electron beam if the filament is located poorly within the cup the negative bias of the Wehnelt cylinder may adversely

affect the emitted beam (Man, Keun, Dong, & Dong, 2008). To prevent adverse effects a multiple stage installation and alignment process is carried out.

First the beam must be located centrally in the cup. This is achieved via the loosening of two captive screws on the underside of the cup. After the screws are loosened the component, the filament fits into can be moved in the plane normal to the front face of the cup. The centrality of the filament can be checked using a low power magnifier. There are no given values in the documented procedure to ensure correct location with the user manual just asking the filament to be centred.

Once central the two captive screws are tightened and the focusing cup insert can be removed. Grub screws on the underside of the insert can then be adjusted to set the correct height of the filament. If correctly aligned the tip of the filament should protrude slightly through the hole of the Wehnelt cylinder. Figure 4-1 shows how the user should observer the centrality and height of the filament. This process of alignment is repeated until the user is satisfied that the filament is sitting centrally at the correct height within the cup. Verification of the location is performed by eye with the aid of low-level magnification.
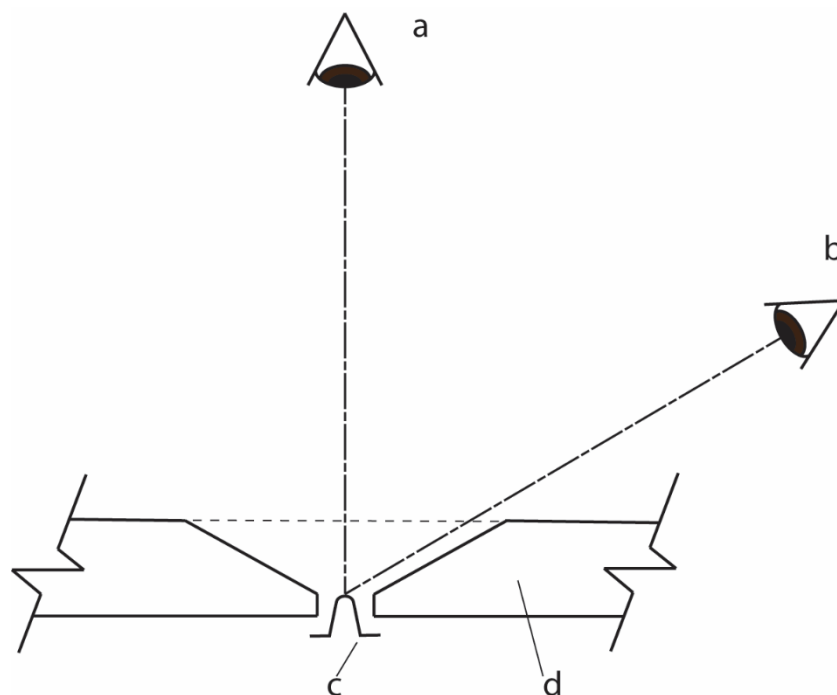
Figure 4-1 filament alignment guide as given in Nikon instructional material. (a) viewing position to ensure central location (b) viewing location ensuring correct filament height (c) filament (d) focusing cup. Image was recreated from Filament change procedure documentation (Nikon)

4.1.2. Pre-installation procedure

Prior to a new filament being installed in the gun the Wehnelt cylinder/focusing cup should be cleaned of any contaminants using compressed air, an alcohol-based cleaning solution and lint free wipes. The filament is installed in the correct location making sure the filament is undamaged prior to installation and ensuring the filament is fitted flat with the ceramic base and pushed firmly into the cup.

4.1.3. Wehnelt cylinder installation

Once the user is satisfied the filament is correctly located the Wehnelt cylinder is installed within the electron gun, which is sealed, and the air pumped out until a high vacuum (3×10^{-6} mBar) is achieved.

The high vacuum prevents unnecessary interaction between the electron beam and any gas molecules in the chamber.

4.1.4. Filament conditioning

To prolong filament life, it is beneficial to condition the electron gun, this process slowly increases the demanded potential difference (kV) of the gun to the maximum expected value, this process is recommended by the manufacturer to be repeated at the beginning of any period of usage. Post installation, this process should be carried out slowly increasing the kV demand until the gun is sitting stably at the maximum expected usage value during the filament life, subsequent conditioning need only be done to the values expected to be reached in the immediate future. During this process it is common for the machine to switch on and off.

4.1.5. Setting filament demand

For this step of installation, the machine parameters should be set to 40 kV and 250 µA, if the image window is oversaturated then the beam current can be reduced until this is resolved. The filament demand should then be set using the control software. The ideal point being the demand value where the live image screen no longer brightens when the demand is increased.

4.1.6. Source alignment for electron beam focussing

The electron beam is now ready to be aligned, this is performed initially using two pairs of manual alignment elements to physically shift the filament relative to the anode ring and magnetic lens within the gun. The first stage of manual adjustment is not suited to fine tuning, as such a second stage using electronically controlled adjustments in the proprietary CT software is performed. To observe if the machine focus is improving, a small, detailed specimen such as a microchip is inserted in the machine and a modulation function is turned on. The modulation function causes the onscreen feed of the XCT to shift rhythmically when the X-rays are on. This live feed allows the user to align the beam which correlates with the live image until there is no longer shifting and instead there is just pulsing in and out of focus. This process is carried out initially at 120kV and 80µA but then is repeated at 150kV, 100kV and 225kV. An interpolation function is then used to note how alignment will shift at any other required values. When this process is complete the electron beam is considered to be in focus. Final settings and signal stability are judged in a subjective manner and as such this process is variable between each focussing operation and between users.

When considering the process listed above it appeared clear the installation of a new filament introduces several variables that whilst essential in achieving optimal machine function may lead to variation in extracted surface texture parameters. As each stage in essential and without completion extraction of areal surface texture parameters would not be impossible, the entire process could be considered as a single variable for the following work.

4.2. Data extraction method and repeatability

When selecting a method of data extraction, it should be noted that new technologies have been developed since the study presented in the previous chapter were considered. Alongside Townsend's method, Mountains software (Digitalsurf France) now allows for the direct importation of stl files as exported from VG studio. Other specialised methods of surface extraction exist such as that developed by Garbout et al for example (Garbout, et al., 2018). However, this method is focused specifically on the extraction of data from topsoil, as it was developed specifically for the authors field, so whilst valid in its own right it is not ideally suited to the presented work. As Garbout's method is optimised for topsoil, Townsend's methods was designed specifically to work with metal AM parts and aligns to

existing standards regarding areal surface data extraction. It is clear in the opinion of the author that the Townsend method is preferable when compared to methods such as those presented by Garbout.

As noted, surface extraction can now be completed by importing a .stl taken from VG studios into MountainsMap, this may still require alignment through a third software such as MeshLab (Thompson, et al., 2018). This method provides a viable alternative to the Townsend's method; however it was deemed by the author that as Townsend's method provided data that adhered to existing standards and that previous studies had used the method which had proved to be repeatable there was no reason to move away from this proven method. By continuing to work with Townsend's method, direct comparison to previous studies was also possible without reprocessing all data with a second method which would be necessary to avoid introduction of a procedural error.

4.2.1. Townsend method repeatability study

The method laid out by Townsend allows for the extraction of areal surface texture data in accordance with existing areal surface texture parameters, specifically ISO-25178 (International Organization for Standardization, 2012). Its adherence to these standards makes it an ideal surface extraction method for this body of work and the field of surface metrology using XCT in its early form. It will allow comparison to existing established methods and thus help to validate results from the method due to the ease by which results can be compared. Developed using focus variation microscopy, specifically an Alicona G4 as a benchmark, it allows the extraction of areal surface texture parameters from an XCT scan, to align the data more closely with that gathered from the focal variation microscopy, any re-entrant features are removed during the extraction process, whilst this somewhat negates the benefits of XCT when observing AM surfaces, it allows data from focus variation microscopy to be compared to XCT data "conditioned" to appear as "line of sight" data. Consequently, this facilitates the comparison of areal surface parameters from XCT and FV systems. To show suitability as the primary method of surface data extraction for the authors work a repeatability study was carried out comparing a single scan processed multiple times to a set of data collected from scans of a single workpiece all processed using the same data extraction method. 20 scans were taken consecutively using the detailed scanning parameters (Table 4-1). The work artefact used was the same 10 mm x 10 mm x 10 mm Ti-6,4 selective laser sintered additively manufactured cube used in Chapter 3.

Table 4-1 scanning parameters used to gather data for the repeatability studies.

Voltage (kV)	185	Filter Thickness (mm)	0.5
Power (W)	9.6	Filter Material	Copper
Gain (dB)	16	Exposure Time (mS)	2000
Voxel Size (mm)	0.02		

Of these scans, a single scan was to be selected at random and 20 copies of the data set were made, purposely misaligned, and then processed to extract areal surface texture data. The data would be processed using Townsend's method, detailed in section 3.3.6, with the hypothesis that the method would be fit for purpose if little to no variation could be seen in the data set consisting of copies of the single scan. The misalignment of the copies necessitated the alignment stage of the method allowing for a more thorough evaluation, it was noted that without any misalignment copies of the same surface produced identical surface maps and parameters. These results would be compared to the extracted surface texture parameters of the 20 consecutive scans. This would allow for a side-by-side comparison of the variation inherent in Townsend's method against that inherent when using XCT for surface metrology. The 20 consecutive scans were processed identically to the misaligned copies first being aligned to the same selected master and then processed in accordance with

Townsends method. The results of both the repeatability data and 20 consecutive scans can be seen in Table 4-2.

To minimise the need for production of multiple samples the artefact used would be the same Ti-6-4 cube to be used in the main study later in this chapter. The 20 copies of an identical scan were to be used to demonstrate variation inherent to Townsend's method. Once all scans and copies had been processed in accordance with Townsend's method areal surface texture data was generated as per ISO-25178. Table 4-2 displays the average measured value across a range of scanning parameters as well as two standard deviations of the data set.

Table 4-2 show the repeatability of using Townsend's method to process one data set 20 times vs 20 scans of the same surface

AMPLITUDE PARAMETERS	Mean Value (Repeatability study)	2StdDev (Repeatability study)	Mean Value (20 Consecutive scans study)	2StdDev (20 Consecutive scans study)
Sq(um)	13.063	0.004	12.401	0.901
Ssk	0.269	0.002	0.218	0.191
Sku	4.546	0.002	4.189	0.331
Sp(um)	93.761	0.353	91.128	11.324
Sv(um)	57.772	0.103	56.487	4.225
Sz(um)	151.533	0.304	147.618	14.738
SPACING PARAMETERS				
Sds(1/mm^2)	198.914	1.403	76.636	10.275
Str	0.462	0.001	0.586	0.127
Sal(mm)	0.327	0.001	0.414	0.010
HYBRID PARAMETERS				
Sdq	0.252	0.000	0.184	10.275
Ssc(1/um)	0.082	0.001	0.051	0.127
Sdr(%)	3.046	0.002	1.658	0.323
SK FAMILY				
Spk(um)	17.650	0.020	16.552	1.219
Sk(um)	30.950	0.005	29.553	1.922

The results clearly indicate that the method introduces negligible variation when compared to the scanning procedure across a range of areal surface parameters, for no parameters did the data from the repeatably study show greater variance then the 20 consecutive scans. This not only proves the viability of Townsend's method but when observing the variation shown supports the hypothesis that using current cone beam XCT technology for surface analysis is affected by variation inherent to the scanning process.

From this work it was decided that moving forward Townsend's method was suitable for the planned study and any further work in the field.

4.3. Full reinstallation of the filament

To best investigate the hypothesised link between the process of filament installation and areal surface texture parameters extracted form the final XCT scan, a study was developed. This study focused on the installation procedure described and would use Townsend's method for surface extraction, as it had proved repeatable. A new filament was installed in the machine as per manufacturer guidelines and a scan of the same Ti-6-4 10mm cube used in Chapter 3 was taken. After the scan was finished the filament was immediately removed from the machine reinstalled and a second scan taken. These scans were the processed using Townsend's method and an attempt was made to generate areal surface texture parameters. The scan taken after the filament reinstallation however proved too noisy to analyse and no useable data could be extracted, shortly after this experiment the filament also failed during unrelated use. This premature failure and lack of useable results led to a need to redesign the study as it was believed that the issues stemmed from the filament removal from the vacuum of the electron gun.

As previously noted in section 3.2, the filaments are stated by the manufacturer as being made of pure tungsten. Tungsten oxidisation occurs at all temperatures however the rate of oxidisation and resulting thickness of the oxide layer are directly linked to the temperature at the surface of the filament (Warren, Nylund, & Olefjord, 1996). The filament must be brought above 2000 K for significant thermionic emission to occur. As the filament was removed immediately after the first scan was complete, and assuming minimal losses due to the filament being held in a vacuum, its temperature was still likely to be much higher than the 200 °C at which a significant oxide layer would quickly form (Warren, Nylund, & Olefjord, 1996). The change in the filament condition was investigated using an SEM shown in Figure 4-2. It is hypothesised that the formation of this oxide layer led to scans taken using this filament after its reinstallation were affected by this. It is also thought likely the formation of this oxide layer contributed to the rapid failure of this sample.
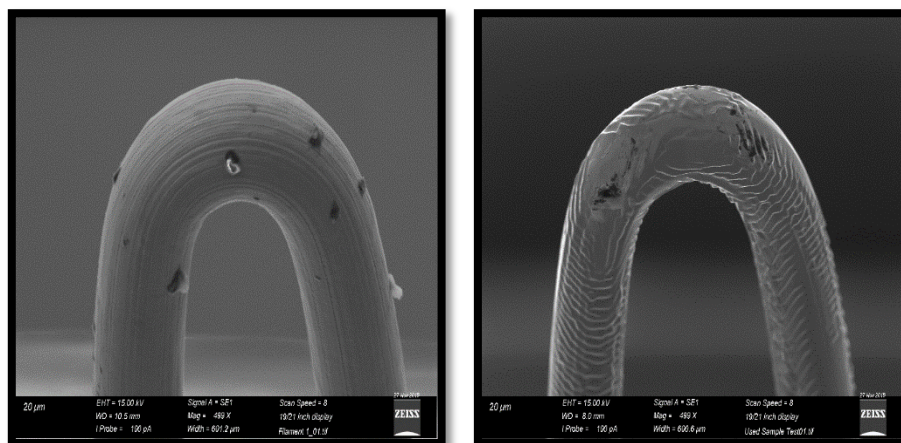
Figure 4-2 comparison of new (left) and used (right) filament a slight drop in diameter and sinificant changes to the surface are clear.

After the disadvantage of the initially proposed method was clearly understood an alteration to the methodology was adopted, instead of a full reinstallation (where the hot filament was exposed to atmospheric gasses), the study would repeat the steps described in sections 4.1.4-4.1.6 between each scan, using the manual adjustment controls (Figure 4-3) to purposely misalign the gun before then realigning and following the process for filament installation. Whilst the filament was not repeatedly reinstalled all other stages important to establishing a well-focused electron beam were carried out. A first scan was taken with the machine prior to any refocusing of the beam, the machine at this point was considered to have a correctly installed and focused filament. The manual adjustment controls were then used to manually defocus the beam and the machine was then refocused as detailed and a
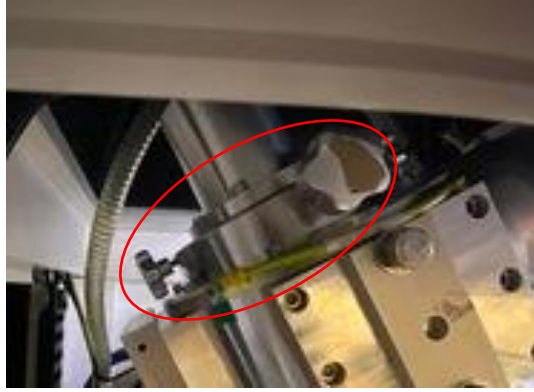
Figure 4-3 manual alignment adjustment controls (highlighted) each control knob has a corresopnding control on the opposing side of the tube.

second scan was then performed. The process was repeated 16 times, during the study the filament required changing after the 6th scan, this was unremarkable as the filament had approximately 180 hours of use at this time. The scans were termed focus set 1 and focus set 2. All scans were taken using parameters identical to those used in the repeatability study.

4.4. Anomalous results

As the present study focused on how variation in data gathering affects extracted surface texture parameters, a wide range of surface metrology parameters were analysed to give a well-rounded analysis of how error may propagate throughout the data collection process. Of the 16 data sets taken 9 were taken on one filament with a further 6 taken on a second. One further data set proved too noisy to yield any significant results as scanning parameters and post processing were standardised it is thought that this may have been due to highly sub optimal machine focusing. A comparison between the high noise scan and a useable scan of the same surface can be seen in Figure 4-4.
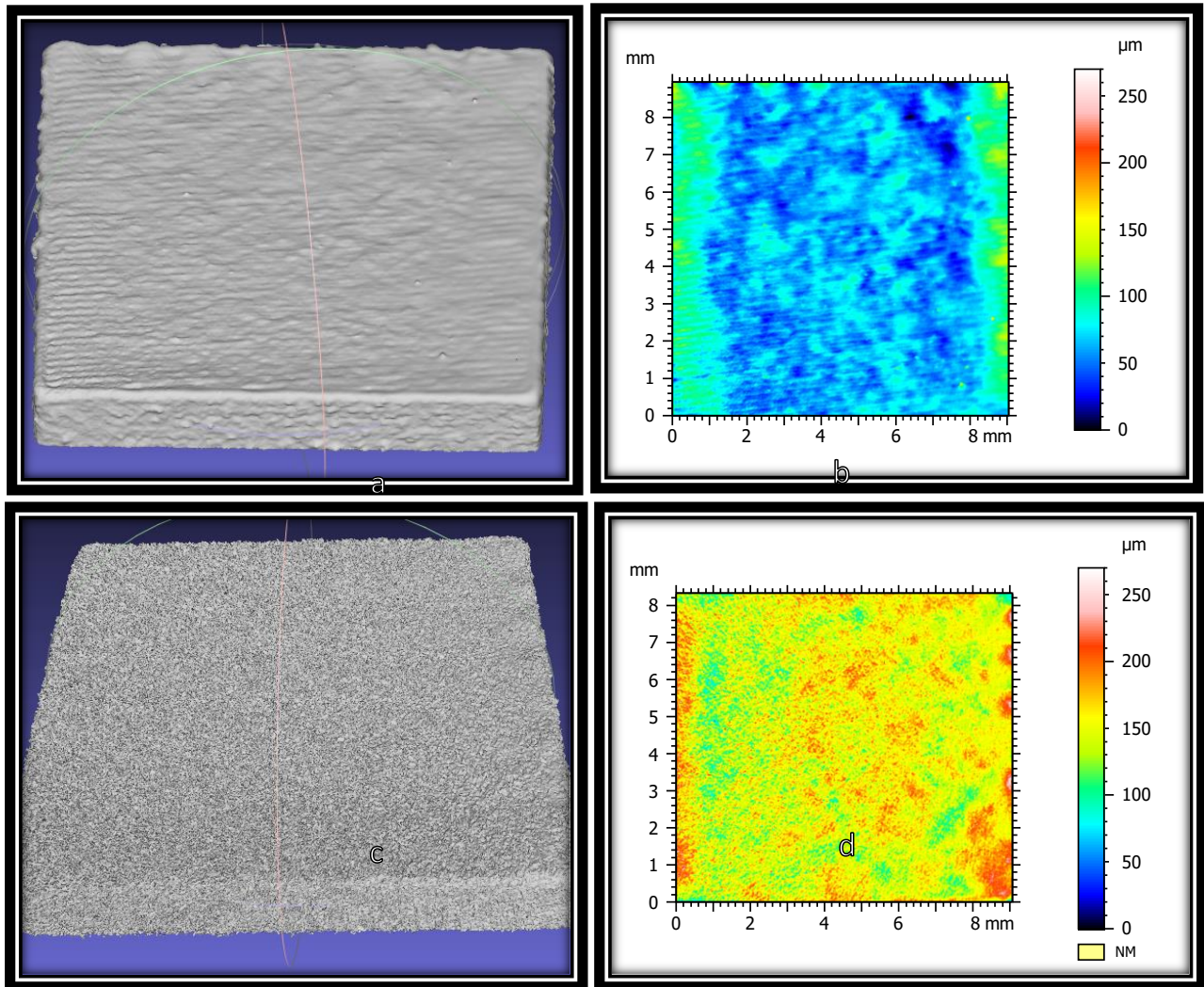
Figure 4-4 Comparison of noise between good quality XCT scan (4a,4b) and noisy scan not fit for use (4c,4d) same vertical scale throughout.

Figure 4-4 c, d, are included here to illustrate the issue that even when machine focus is "nominally" optimal, extremely poor results can be obtained when extracting surface data despite using scan conditions that have previously obtained usefully quantifiable data.

4.5. Initial analysis of refocusing study results

Initial results showed variations in extracted surface texture parameters between each focus set, these results showed consistent variation across the two filaments with there being no statistical change between the two data sets across a range of surface texture parameters. When compared, the mean Sq and Sdr representing amplitude and hybrid parameters of the two data sets lie within one standard deviation of each other. This indicates that the variation between filaments may be attributable to changes in focus when installed and not the deviation between filaments. This is demonstrated in figures 5a through 5c. Spacing parameters as represented by Sal, did not follow this pattern with the mean values not lying within the single standard deviation, though the variation in results was low with a maximum variation of 0.056 mm between the two data sets.
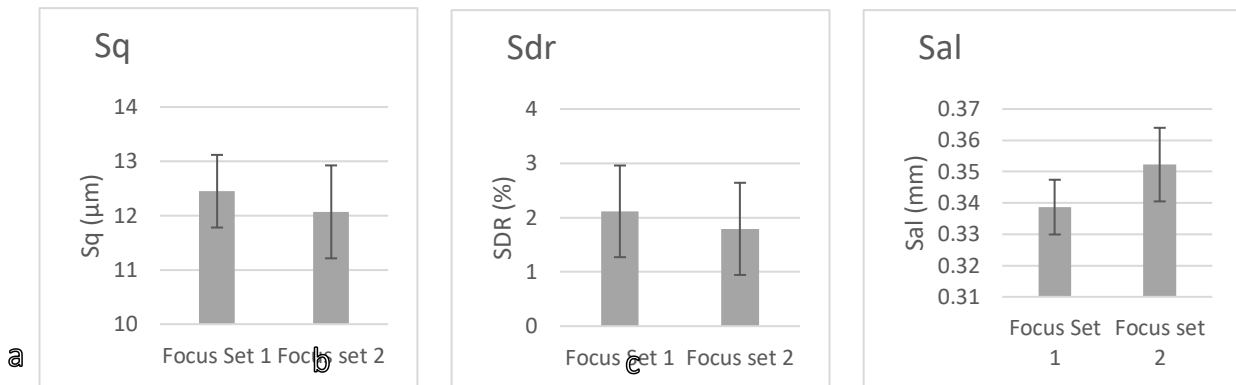
Figure 4-5 Graphical representation of the variation seen across amplitude hybrid and spacing parameters when varying machine focus. Sq (5a) Sdr (5b) Sal(5c)

Initial comparison between the two filaments data sets showed that the variation between the filaments for a range of surface roughness parameters is of a lesser impact than previously thought, with significant overlap in the data sets. The variation seen when refocusing the machine is larger than that seen between the first and second filament, this further disproves the hypothesis from Chapter 3 that differnce in the filaments were the main cause of variation between scans. A t-test was carried out comapring results from the two data sets and showed the differences between the two data sets were negligable.

4.6. Comparison to filament life study results

Initial results showed that changes in surface texture parameter due to altered machine focus were greater than the equivalent changes after different filaments. Comparison to the surface data presented in Chapter 3 is now carried out as to better demonstrate this variation across a range of surface roughness parameters. All data for both studies use the same single artefact. Though to further minimise variation all data from both studies was aligned to the selected master used in the newer study using the software CloudCompare, details of the alignment procedure can be found in section 3.3.6.4.

4.6.1. Amplitude parameters

When comparing the amplitude parameter results given, to the results from Chapter 3 close to direct comparison is achieved as the same surface was measured with comparable scan conditions. While the relevance of individual scans from the study is low, comparisons between each filament and the focus settings of the XCT can be drawn. An example of which can be seen in Figure 4-6 comparing the mean Sq sand Sa value of a given surface from a sample data set of varying XCT focus to the results of multiple filament changes.
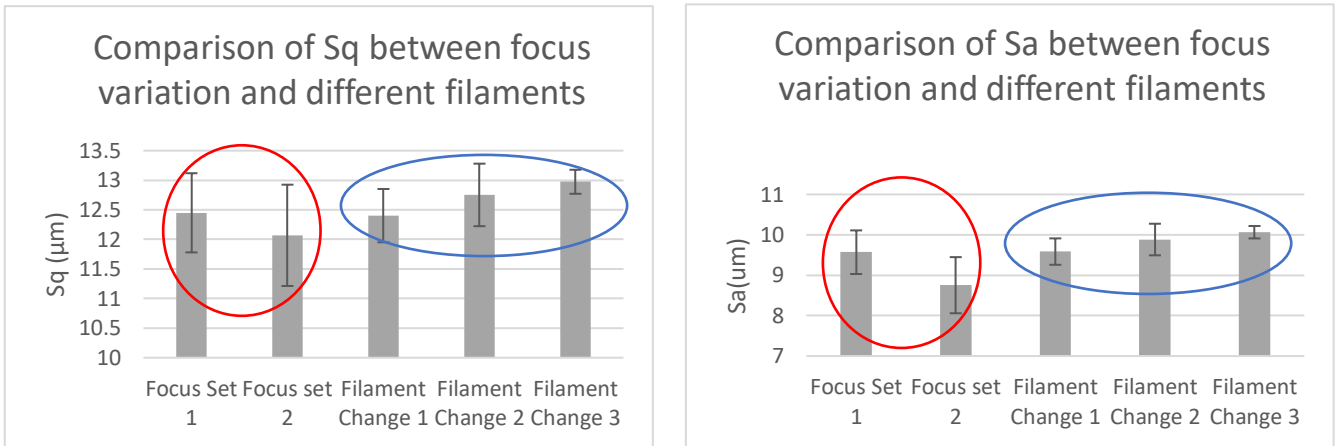
Figure 4-6 comparison of variance seen in Sq (left) and Sa (right) when refocusing machine against full filament changes. Note Focus Set 1 and Focus set 2 consist of 16 measurement whereas the filament change data sets consist of 30 measurements

Almost all Sq and Sa values taken during the first filament change study fall within one standard deviation of the mean for the focal length variation study, this is indicative of the trend seen across all amplitude surface parameters. From this, it can be hypothesised the variation seen in previous work was in fact resultant from the focus being altered after the installation of each filament. A statistical T test was carried out showing that the variation in Sq of data sets filament change 1,2 and 3 was not significant, this is supported when compared to the larger variation in focus set 1 and 2 in Figure 4-6.

4.6.2. Hybrid parameters

As with amplitude parameters, hybrid parameters followed a pattern where most results from the author's previous filament life study sat within one standard deviation of mean of the focus variation data presented in this report. Sdr was chosen to represent this graphically (Figure 4-7). A larger proportion of values lie outside of one standard deviation of the focus work mean; however, the majority still sit within one deviation whilst non-sit outside two standard deviations of the mean of focus set.
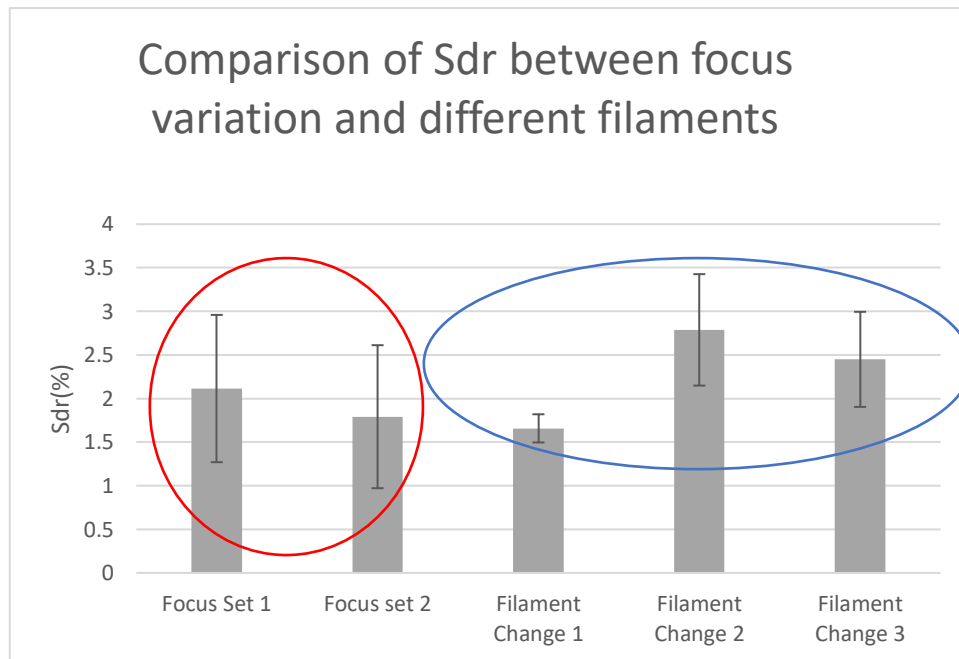
Figure 4-7 Variation in Sdr when altering machine focus compared to that of different filaments, Note Focus Set 1 and Focus set 2 consist of 16 measurement whereas the filament change data sets consist of 30 measurements.

4.6.3. Spacing parameters

For spacing parameters (Figure 4-8)grouping was typically much tighter with Sal and Str across all data sets showing a standard deviation of less than 0.01 from the mean value.
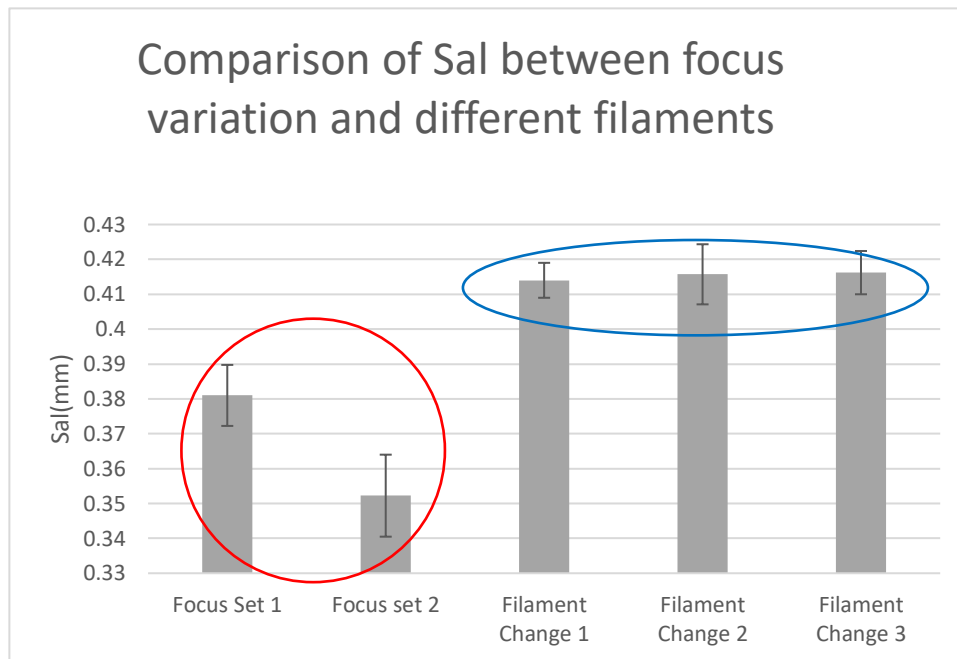
Figure 4-8 Variation in Sal when altering machine focus compared to that of different filaments. Note Focus Set 1 and Focus set 2 consist of 16 measurement whereas the filament change data sets consist of 30 measurements

This did not then follow the trend displayed across other parameters where most data commonly fell within one standard deviation of the focal variation data. However, there was minimum variance across all data sets and a maximum variation of 0.085 mm across all data sets. Changes in surface parameters in the focal variation data did follow the pattern of wider variation of higher variation than when focus was not adjusted. This may be due to the spacing elements of the surface which are generally larger, being less affected by focussing variation.

4.7. Conclusions of Chapter 4

The work presented in Chapter 4 investigates whether there is a link present between the process of installing a new filament into a XCT electron vacuum tube machine and the variation in areal surface texture parameters noted in previous chapters and other published work. The hypothesis that the installation and focusing of a new filament is a significant factor in the variation noted was proved to be correct. It is clear when analysing the large number of parameters gathered that variables introduced by the installation process are responsible for the majority of the variation noted. By reinstalling the same filament multiple times without removing the filament form the vacuum the variable of the filament was removed, however the variation between each reinstallation remained consistent with that noted from filament to filament. As the variation remained consistent when a variable was removed, then based on the results, it is the opinion of the author that the variable does not introduce significant variation. As a consequence, the author's hypothesis from Chapter 3 was proved false, the filament degradation and the variation between new filaments do not have a significant effect on areal surface texture parameters. The studies presented in this chapter however, supported the hypothesis that developed from the conclusions of Chapter 3, it is the installation process introduced variables that was responsible for the noted variation.

When observing the data, the variation in areal roughness parameters shown from a single filament reinstalled multiple times was consistently larger than the variation seen between different filaments. The majority of the results gathered in Chapter 3 fit within 2 standard deviations of all results gathered in the re-installation study. This indicates that the variation shown in Chapter 3 work is likely as a result of the installation procedure. This is supported by section 4.6 which have demonstrated that variation to the focal spot of the electron beam, can cause variation in the resultant radiographs.

In Summary

- Filament age and degradation have little significance in the extracted surface parameter variation shown here.
- The installation process of a new filament into the machine, particularly the focusing, is likely the cause of most of the variation in extracted areal surface texture parameters. This is supported by literature investigating the focal spot.
- The next stage of research should focus on measuring how the focusing procedure of the installation process can best be measured. This measurement would allow for any quantifiable links to be established.

5. Development of a novel method for measuring XCT focal spots

As proven in Chapter 4, focus variation, the focusing process of a cone beam XCT machine, appears to be a significant contributor to the variation in extracted surface roughness. This variation has been presented in all experimental results gathered to this point. In order to try to formally establish the relationship between focus variation and extracted surface roughness. A method for measurement of focus spot variation is required. Unfortunately, the focus spot parameters cannot be directly quantified by the XCT machine itself and as such, a specific method of measurement is required.

The focal spot, as discussed in section 2.2, is the point of X-ray generation in the XCT process. Its shape and intensity have been shown previously to affect the emitted X-rays, this is expanded on in section 2.5.1. However, a correlation between this variation and the variation in extracted areal surface texture data noted in this body of work, has yet to be established. It was considered that by measuring the focal spot in situ, during measurement of a surface, a link may be established.

The development of a method allowing for in-situ focal spot measurement throughout a XCT scan and across multiple scans is needed to allow the possible correlation between an XCT focal spot's geometry and the extracted areal surface texture parameters. Measurement of focal spots can be achieved via several different methods (BSI, 1999) (Probst, et al., 2019). Consequently, a review of existing methodologies was carried out to assess the viability of using one of these pre-existing methods for analysis of the focal spot as defined above. If a suitable method did not present, then a greater understanding of these methods would provide a base for a novel method to be developed.

5.1. Review of existing methods of focal spot measurement

A variety of methods are currently described in standards and literature for analysis of focal spots. The subject is also addressed somewhat in section 2.8. As a result of this, a deeper review of these methods has been carried out below in order to assess suitability for adaption to use in the present work. Any adopted method must meet 3 set criteria:

1. Have the ability to measure focal spots in the size range of 7-200 μm (the given size range of Nikon XTH 225 focal spot used in this study)
2. The method must be able to be integrated into a normal scanning environment i.e. must be possible to measure both focal spot and a given part surface concurrently.
3. The equipment required for the method must be installable within the dimensions of the Nikon XCT used in the present study.

5.1.1. BS EN:12543

BS EN:12543 are series of standards detailing methods that allow for focal spot measurement. Each section (1-5) is targeted at a specific machine type and equipment sets, allowing a range of valid methods dependant on user requirements or circumstance.
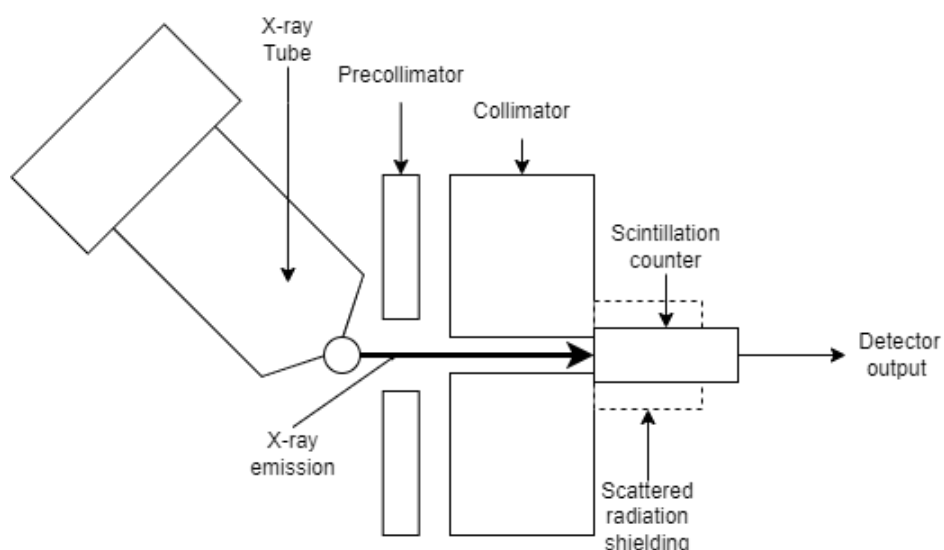
Figure 5-1 required set up for BS EN:12534-1

Section 1 of the standard describes a scanning method, suitable for applications where quantitative values for intensity and spot size are required in machines where the tube voltage does not exceed 500 kV. The method employs a highly collimated receiver and can measure focal spots above 100 µm in diameter. The method relies on an approximate size of the focal spot to be known so that a collimator with the correct hole dimension can be installed. A lookup table can be found in the standard for this purpose. A pre-collimator, double slit collimator and radiation detector is mounted on the CT machines manipulator, with the radiation detector output connected to a data processor as seen in Figure 5-1.

The method provides a thorough analysis of the characteristics of the focal spot regarding both dimensions and intensity. The use of shielding around the detector minimises the influence of background radiation, and the method can measure relatively small focal spots from very high voltage tubes. However, it requires specialist equipment, and a concurrent surface measurement by the XCT cannot be taken at the same time. As a result of this, this method whilst thorough, is not considered a suitable method for measuring the focal spot simultaneously to a part surface, essential to investigate the potential correlation between the two. It would also not be suitable as a base for development of a novel method.

5.1.1.2.   BS EN:12543-2

This section specifies a method for the measurement of focal spots of a size of 200 μm or larger in diameter and tube voltages up to 500 kV, using a pinhole camera. The pinhole camera diaphragm size is governed by the focal spot size as with section 1 of the standard, a lookup table is found in the standard. The radiographic image detector is placed normal to the beam direction at a distance n from the face of the pinhole diaphragm as shown in Figure 5-2.

Figure 5-2 key:

1 plane of anode

2 reference plane

3 radiograph image detector

4 magnified length of effective focal spot

5 beam direction

6 incident face of the diaphragm

7 physical length of the actual focal spot

m distance between incident face of pinhole diaphragm and focal spot

n distance radiograph image detector and incident face of pinhole diaphragm
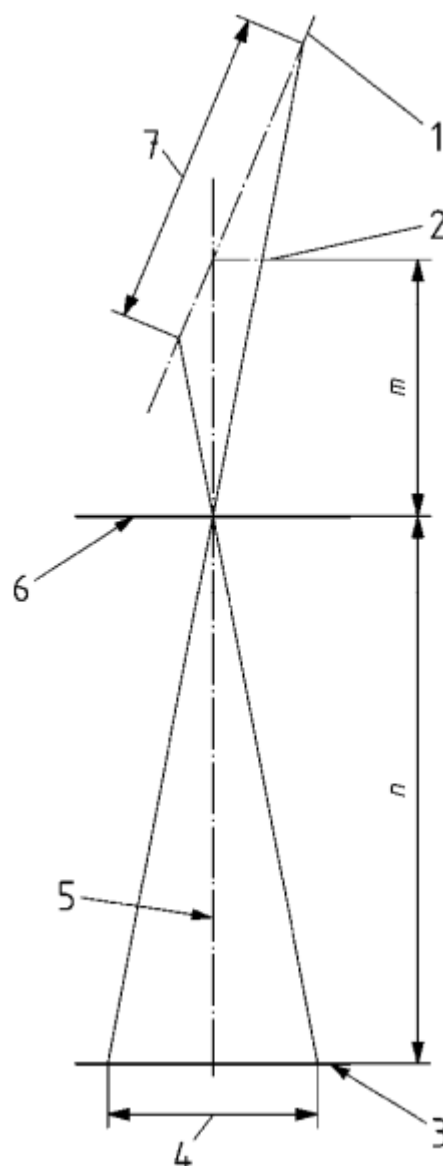
Figure 5-2 geometry of pinhole set up taken from (BSI, 1999)

The generated grey scale image of the radiation detector will be representative of the X-ray dose, by evaluating the image, focal spot size can be obtained. Pixels with an intensity 10% greater than the maximum value above background intensity are represent the area of the focal spot. An example output of this can be seen in Figure 5-3
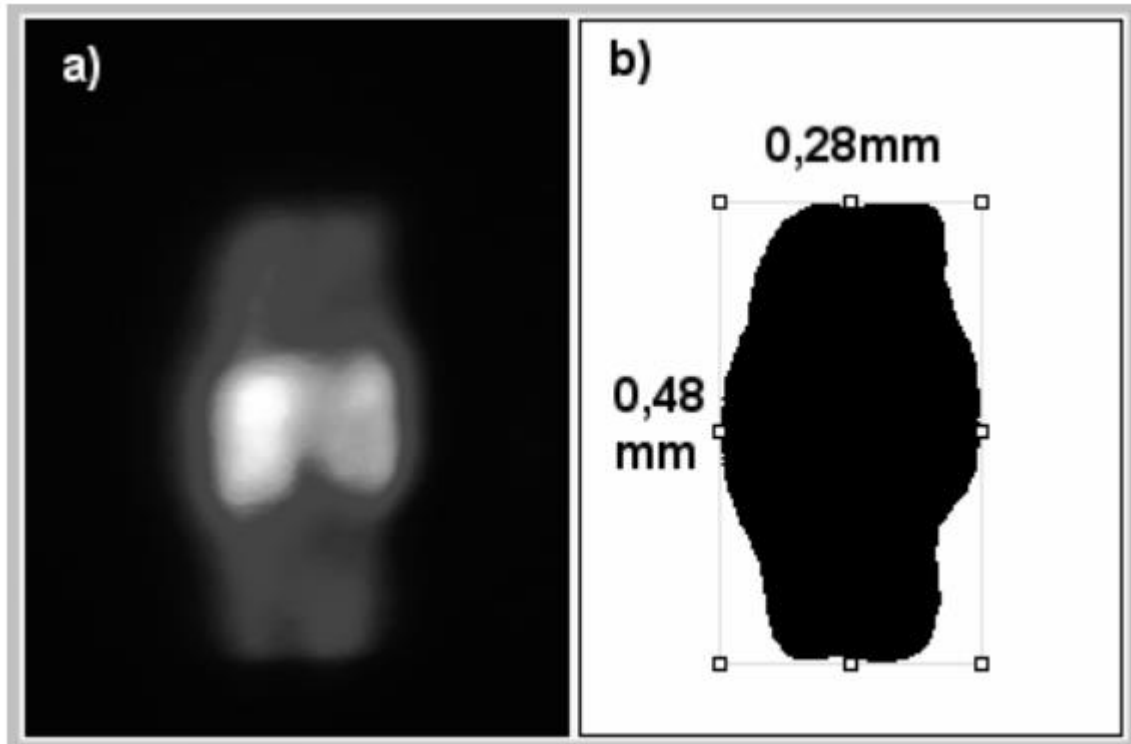
Figure 5-3 evaluation of focal spot size via pinhole camera method, taken from (BSI, 1999) a) grey scale imager proportional to x-ray dose, b) evaluation result based on 10% threshold showing focal spot dimensions.

The pinhole method generates a clear profile of the focal spots size, geometry, and intensity as seen in Figure 5-3. Like BS EN 12543-1, it can be used for high voltage tubes up to 500 kV. However, it is not suitable for the measurement to focal spots less than 200 µm. The Nikon XTH225 has an estimated maximum focal spot size of 225 µm. Due to this, the method is again considered unsuitable for use in the proposed study and would not make a suitable base for developing a novel method.

This section covers a method where a slit camera is used to measure focal spot size, it is suitable for focal spots exceeding 100 µm in size, with X-ray tubes where tube voltage does not exceed 500 kV. The applied voltage is however limited to 200kV. The slit camera used for the method follows the dimensions in Figure 5-4 and is made of tungsten or a similarly absorbent material.
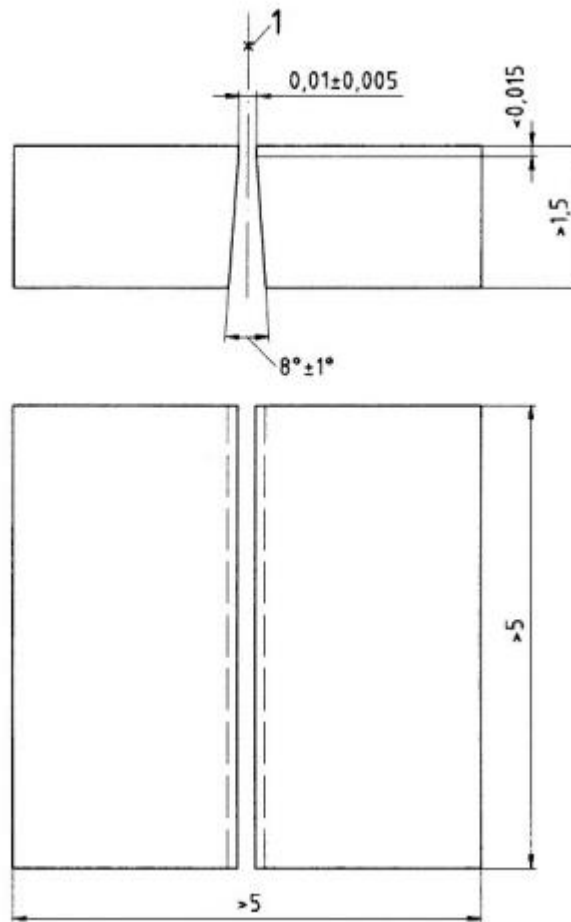
Figure 5-4 dimensions of the slit camera for use in focal spot measurement, point 1 represents the symmetry axis. taken from (BSI, 1999)(all dimensions in mm)

The arrangement of the equipment for this method is similar to that of BS EN:12543-2 shown in Figure 5-2 with label 3 now representing film instead of a detector, m now being the distance between the slit block and focal spot and n the distance between the film/detector and the slit block.

Once two radiographs have been produced the focal spot size is determined by physical measurement of the artefact on the image. The size is given in each direction measured direction. This method requires an un-interrupted detector meaning that it would not be possible to use with a measurable surface in situ, the minimum focal spot size of 100 µm is also too low for the Nikon XTH 225 system.

Section 4 of EN12543 uses analysis of sharp edges to measure focal spots of 500 µm or more and is suitable for tubes with voltages up to 500 kV. The method as designed uses a thick-walled metal pipe covered in 1mm lead sheet to provide a straight edge. The lead covered tube is located between the source and detector as shown in Figure 5-5.
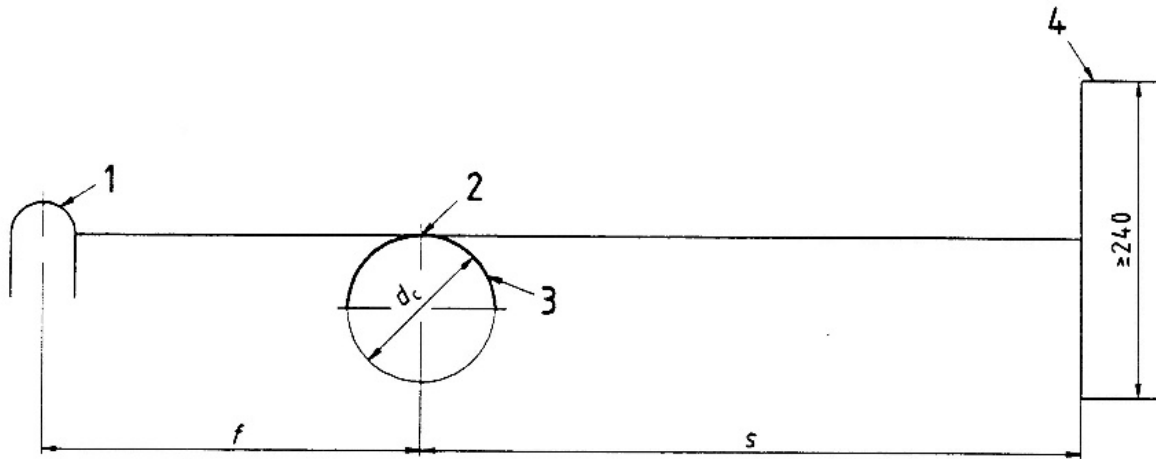
Figure 5-5 arrangement of metal pipe in XCT for BS EN:12543-4 taken from (BSI, 1999)

Figure 5-5 Key

1. Source

2. Edge

3. >1mm lead film on steel pipe

4. Detector

F-Distance to artefact edge from source

S-Distance from artefact edge to detector

di-Smallest measurable area for optical density (1 pixel if using a detector or densitometer tip size on film)

dn- expected focal spot size (given by manufacturer)

A minimum of two radiographs need to be taken with the tube positioned horizontally in one, to measure focal spot height. For the second radiograph the tube should be vertical, for the calculation of the focal spot width. Image intensity profiles need to be taken perpendicular to the straight pipe for both radiographs. The 5% and 95% values of intensity are calculated and displayed on the intensity profile. The distance between these two points on the radiograph represents the geometric un-sharpness (u_g). The focal spot length and width can then be calculated using a series of equations given in the standard.

The edge sharpness method allows for rapid testing due to the lack of complex equipment required. However, it is also notably the least accurate method and not suitable for focal spots of a micro XCT at lower powers due to the large minimum focal spot size.

Section 5 is specific to micro focus CT and thus was selected as the basis for an automated method. The method is specific to micro focus XCT machines with a tube voltage no higher than 225 kV and allows accurate measurement of focal spots from 5 μm to 300 μm in diameter. The introductory statement of the standard also notes that the focal spot size is a key contributor to image quality and resolution. The method measures image sharpness at the edge of a given artefact, in this method specified as either a pair of crossed wires or a ball of highly absorbing material such a tungsten or platinum. The diameter of the artefact should be between 0.9 mm and 1.1 mm with an accuracy of ± 0.01 mm.

The test object should be mounted on a polyethylene strut between magnification of X 20 and X 100 in the machine, the minimum distance to source should be no less than five times the diameter of the test object. Image profiles along the length (y axis) and width (x axis) of the generated radiographs are then taken and the diameter of the object can be measured detecting the edge of the artefact at 50% of the total image contrast. This allows the user to calculate geometrical magnification $M_{l,w}$ using:

$$M_{l,w} = \frac{D_{l,w}}{D_{real}}$$

Equation 5-1

Where

$D_{l,w}$= measured object diameter in given axis

D_{real}= true object diameter

It should be noted many modern XCT machines provide the user with a geometric magnification value in the user interface, meaning this step can be skipped. The distance from the 90 % to the 50 % image intensity is then taken along the line profile and distance between the points on each side is taken. It is of note the thresholds for section 5 of the standard are significantly different to those in section 4 this may be 50 and 90% compared to 5 and 95%. This may be related to the resolution and geometric un sharpness present in the scans, it is likely these values differ greatly between a 5um and 500um focal spot.

These 90-50% distances are then used to calculate focal spot size in a direction (D) using Equation 5-2 changing $M_{l,w}$ to the relevant axis.

$$D = \frac{(\overline{EF} + \overline{GH})}{M_{l,w}}$$

Equation 5-2

Where *EF and GH* are taken as the distance between points from Equation 5-2.
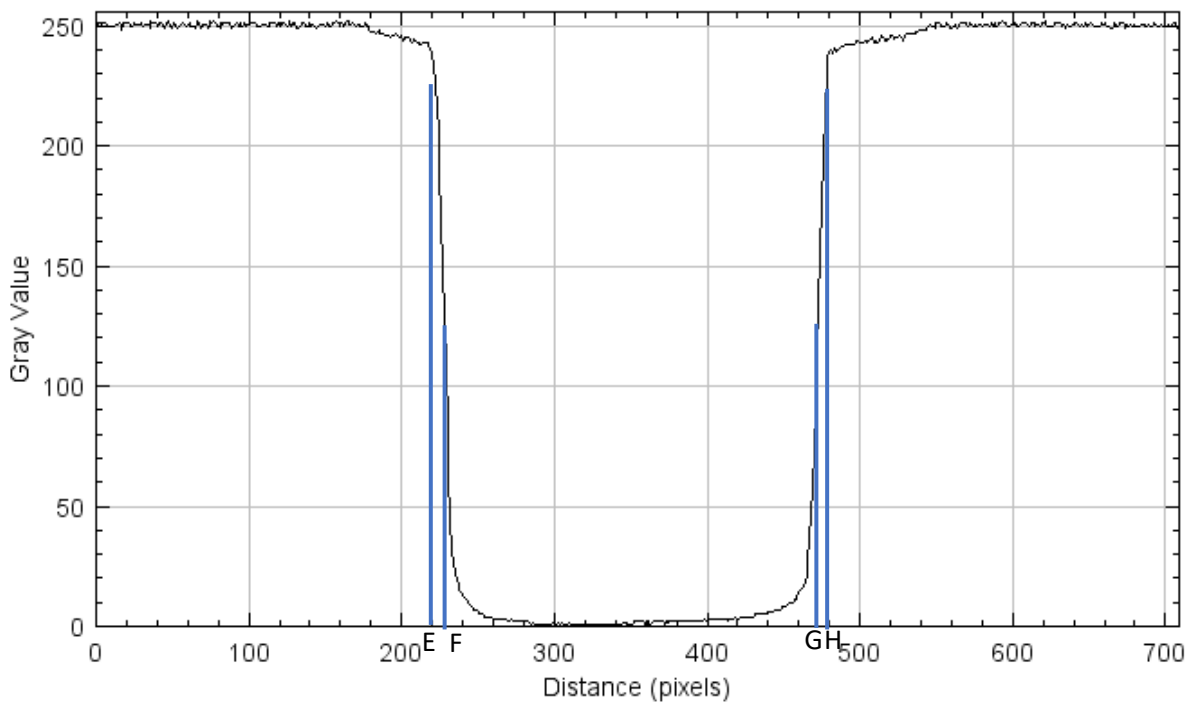
Figure 5-6 place holder for intensity profile

This method is specifically developed to work with micro XCT and has a potential for use in the present study, it could also be used as a base to develop a novel method of focal spot measurement specifically for integrating into simultaneous measurement of artefact surfaces. Of the existing methods accepted by the standard, this method clearly would be easiest to modify to suit in situ measurements due to its suitability for a small focal spot and its non-reliance on covering the entire detector with collimators or other equipment.

5.1.2. Siemens star pattern method

The use of a Siemens star pattern, as discussed in section 2.4.1 as a method of focal spot analysis was also considered for use in this study (Probst, et al., 2019). Whilst the method allows for a great depth of analysis the SSP covers the entirety of the X-ray tube window, as such it will interfere with any artefact placed in the chamber for scans, conversely any artefact would interfere with the SSP in the scan. As a result, the method does not provide a suitable base for development of a novel method nor is it suitable in its current form.

5.2. Summary of focal spot measurement methods

After reviewing a variety of existing methods of focal spot measurement it was decided that a novel method would be the best approach. This novel method would use BS EN:12543-5 as a base but would be developed to allow for measurement of the focal spot for an increased number of angles. Of the available artefacts the ball was selected in the form of a high-density ball bearing. A ball of sufficient accuracy would provide an ideal artefact. This method provides an ideal basis for development as it does not require large amount of equipment to be put in the X-ray beam, it is also specialised in its specific deign for use with micro-CT systems, and will not limit the measurable focal spot size, as would be an issue with the other presented methods. The method would also be extended to allow the simultaneous measurement of a "known" surface alongside the focal spot. The simultaneous measurement of both the focal spot and surface will allow for investigation into the link between variation in the dimensions of the focal spot and the extracted areal surface texture parameters. Prior

to developing a novel method for focal spot measurement, small studies using the exact method described in BS EN:12543-5 were to be carried out, alongside this, a method derived from section 4 of the same standard was tested as the method was simple enough that to be replicated quickly.

5.3. Measurement method

Before a method based on the noted standard was developed that automated and increased the scope of measurement, initial tests were run on BS EN:12543-4/5 to evaluate their suitability as a base. The method described in section 4 as noted is not designed for micro-CT. Nevertheless, it was decided to run a test of the method as no specialist equipment was required. The methodology laid out in section 5 is designed for micro XCT and was hypothesised to provide the best point from which to develop a focal spot assessment method. Once a base for the method was selected a novel automated approach would be developed. The automated approach would be required to take images from a full XCT scan, typically 1584 images, plotting the focal spot dimension across the circle in 180 locations.

5.3.1. Initial Tests

5.3.1.1. BS EN:12543-4 testing

To test the ease with which the focal spot measurement methods could be applied on the Nikon machine, an initial viability study was carried out using a method based on EN BS12543-4 to evaluate the plausibility of measuring the focal spot. A dense steel rod with a straight edge as required by BS12543-4 this was placed in the XCT machine at a distance between the emitter window and detector adhering to the standard. An AM metal cube 10 mm x 10 mm x 10mm was also included in the scans to act as a calibration artefact to set image scale. Once the radiograph was taken in both x and y the focal spot dimensions could be calculated using Equation 5-3 for the horizontal plane and Equation 5-4 the vertical plane.

$$l = U_{gh} \times \frac{f}{S}$$

Equation 5-3 for the horizontal plane

$$w = U_{gV} \times \frac{f}{S} \text{ in}$$

Equation 5-4 the vertical plane

Where

l is focal spot length

w is focal spot width

f distance between focal spot and edge (Figure 5-5)

s edge to film distance

ug is given as the geometric un-sharpness between the 5% and 95% values of intensity

The focal spot was calculated at 190x363 microns, this is over the manufacturer specified limit of the focal spot, but at the high powers used during the image generation process is not unreasonable, the method used is also not best suited to micro CT as noted.

From this initial testing it was determined that measurement of the focal spot was possible. A further study assessing the viability of BS EN:12543-5 was required before developing an extended novel method of focal spot size assessment.

To test the ease with which the agreed upon standard could be applied to the used Nikon XCT machine, a second viability study was conducted, the focal spot would be measured according to section 5 of BS EN:12543. If successful, this method would be used going froward for development of a novel protocol. The BS EN:12543-5 standard requires a high-density metal ball 1 mm in diameter with a tolerance of 0.1mm and a sphericity of P-V 0.01 mm. Grade 10 tungsten ball bearings were acquired for this purpose. Tungsten is mentioned in the standard as a suitable material. Ball bearing grades relate to the tolerance it was manufactured to, grade 10 falls within the required tolerances of the standard Table 5-1.

Table 5-1 tolerance's of grade 10 ball bearing compared to those required by BS EN:12543-5

	Size mm	Sphericity mm	Nominal Diameter Tolerance mm	Surface roughness (Ra) µm
Grade 10	Sizes range from 0.1524 to 254	0.00025	±0.0013	0.025
BS EN:12543 Requirement	0.9-1.1	Na	±0.01	Na

As with previous studies the XCT machine used would be the Nikon XTH 225 machine, a tube voltage of 85kV and a tube current of 81 µA were used. No filter was present. The location of the part within the XCT was governed by the standard using Equation 5-1, this gave a best possible magnification of X 50. The sphere was mounted in a polymer cone Figure 5-7.
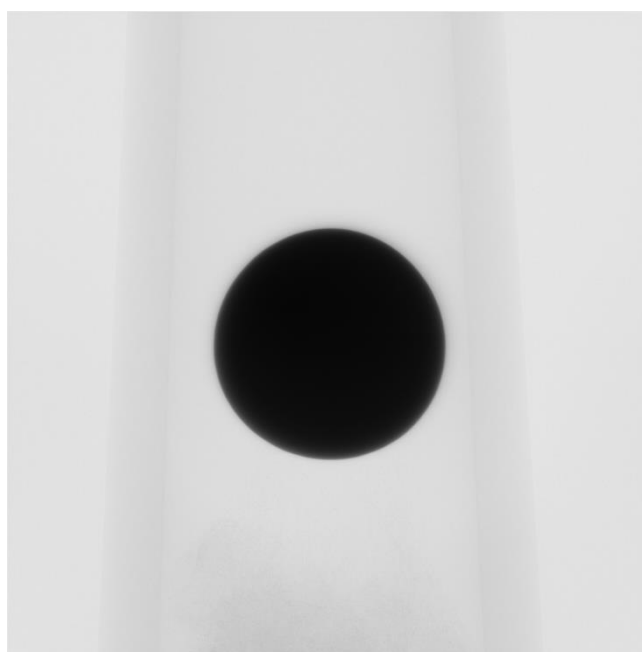
Figure 5-7 shows tungsten ball bearing in polymer cone, the cone is barley visible due to the high energy required to image the tungsten.

Once a set of radiographs were taken, analysis of the focal spot was carried out. Using the free online ImageJ software line profiles in X and Y were taken through the centre of the ball bearing. The centre

was found iteratively by plotting profiles in X and Y in ImageJ. The line profiles were adjusted until the profile showed that the width of the "material pixels" was the widest, this was taken as the centre. These line scans were exported as CSV files for analysis. The data comprised of a grey value for each given pixel along the line scan. As the pixel size was governed by the magnification and is given by the machine the scale of the image was calculated. From this, the ball bearing diameter could be measured and was calculated at 1.024 mm within the acceptable limits for the standard method. The 0 and 100 % intensity values were taken and from this, the 50 and 90 % values calculated. The .csv files were then searched for grey values that matched the calculated thresholds, these were then obtained and the x and y coordinates of the corresponding pixels in the image were used to make measurements for the required distances as specified in the standard. With these distances, equations Equation 5-2 could be used to calculate the focal spot size longitudinally and vertically. This gave a focal spot size of 0.074 mm in the horizontal and 0.129 mm in the vertical axis. This indicates an ellipsoid focal spot and lies within the specified manufacturer tolerances of the Nikon CT. As focal spot size is influenced by the tube parameters both the focal spot size and tube voltage were in the middle of the operating range which as would be expected.

5.4. Developing a novel method of continuous focal spot measurement

The developed method would be derived from the method demonstrated in section 5.3.1.2, the key changes would be the automation of the process to accomplish measurement of a focal spot across a scan or set of scans quickly, and the simultaneous integration of the method into scans of artefacts with a known surface roughness. This will allow the hypothesised correlation between focal spot size and extracted areal surface texture parameters to be investigated.

5.4.1. Sample images for testing and development of a novel method of focal spot analysis

To develop a method for use as stipulated in section 5.3, a selection of scans of varying scanning parameters were taken in line with that specified in BS EN:12543. Of the two possible artefacts described in the document, a high-density ball bearing, was selected. The selection was made as a high-density sphere would not require additional fabrication, thus reducing the time it would take to begin the work. A tungsten ball bearing could be used as the artefact matching the requirements stipulated in section 5.1.1.5. The use of a sphere artefact would also allow the method to be integrated into a simultaneous scan of the AM artefact surface as a sphere of suitable accuracy would not be affected by the rotation of the stage.

5.4.2. Image import and conversion

The Nikon 225XT-h XCT system used for the study exports a series of TIFF images that are then used to construct a 3D model based on the 16-bit greyscale values of the image. These images are taken and imported into MATLAB where they are then converted to 8-bit greyscale meaning a small data range 0-255 instead of 0-65536. 8-bit greyscale was selected as it is shown being used in the standard method and allows easier data handling due to the lower range of values.

5.4.3. Intensity thresholds and image contrast

The intensity thresholds are then found, first a background intensity value is taken from a region where no artefact is present, the mean intensity value of this region is taken, this is assigned as the maximum intensity value. The lowest pixel intensity value in the image is then found and an average of its neighbours is taken to eliminate possible anomalous results. This is assigned as the minimum intensity value from this the image. Where two or more non-neighbouring pixels with equal values are both equal to the lowest value the pixel closest to the centre of the image is taken.

This high and low value are then used as the 0-100 % image contrast and from this the 50 % and 90 % thresholds are calculated.

5.4.4. Finding true artefact centre

For accurate measurement, a deviation of the method stated in BS12543-5 is used where the profile traces must be taken through the centre of the ball artefact. This led to the requirement to find the true centre of the artefact accounting for any shift in the position of the artefact between radiographs, as a method is not stated in the standard. In theory the centre of the ball bearing would provide the darkest section of the radiograph, as when scanning a sphere the longest path through it for an X-ray would be the centre, thus leading to the highest level of attenuation. However it was found that pixel greyscale varied sufficiently throughout the scan it that multiple low intensity pixels were found to create multiple false centres when using a simple "find lowest value" method. This led to inaccurate focal spot measurement and the false centres would often lead to errors in the code. These false centres can be seen in Figure 5-8 as the blue asterisk marks.
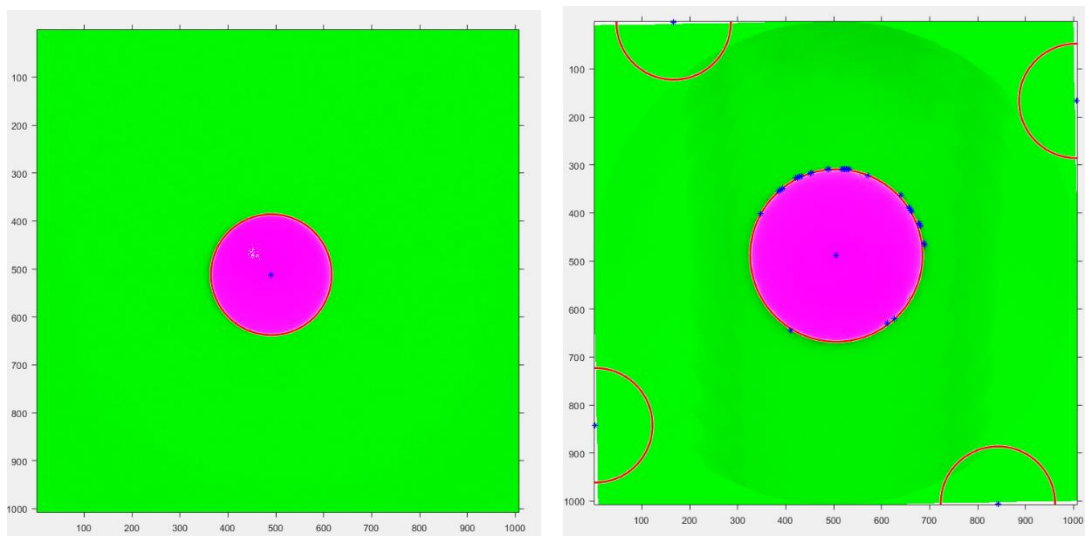
Figure 5-8 images used to find centre (left) ideal conditions with 1 centre 11. (right) large number of false centres due to artefacts

Table 5-2 key to Figure 5-8

Figure 5-8 Key	
*	Possible centre
O	Best fit circle (centres must be inside)
	Free space/Air
	Artefact/Material (ISO 50)

Using the true image centre relied upon the artefact's placement being accurate across all scans, thus it was not considered as workpiece position was found to vary slightly in X during the rotation of the stage. Variation in Y was less significant. A three-stage process was developed as an alternative to using either the image centre of solely the darkest pixel value.

First a manual analysis of a group of radiographs of the artefact is carried out with the objective of finding a range of values where the centre of the ball bearing could pass through, these values were stored as an array in the script. This gave a range of coordinate values the centre of the workpiece would likely fall within. The darkest pixel is then found alongside an average background value where the artefact was never present, using these the 50 and 90% thresholds required where found. All pixels that matched the darkest pixel value were highlighted as possible centres, this is seen in Figure 5-8, it can be seen that some pixels around the edge of the artefact are present highlighted, these are

examples of beam hardening described in section 2.4.3. Circles were then fitted using the 50% threshold and the possible centre values. This was done such that all centres sat within a circle and the circles all had a circumference that passed through pixels approximately equal to the 50% threshold value at points. These circles can be seen in Figure 5-8. All possible centres were then compared to the array of coordinate values defined in the manual analysis step. The potential centre (x, y) coordinates were subtracted from each set of (x, y) coordinates in the array as seen in Equation 5-5.

$$\begin{bmatrix} x_n \\ y_n \end{bmatrix} - \begin{bmatrix} x_p \\ y_p \end{bmatrix} = \begin{bmatrix} \Delta x \\ \Delta y \end{bmatrix}$$

Equation 5-5

Where x_n and y_n represent all given coordinates of the manually defined array

And where x_p and y_p are the x and y coordinates of every given potential centre

Δx and Δy represent the difference between a given coordinate in the defined array and the potential centres coordinates.

This data was stored in an array for each potential centre value of the Δx and Δy values, where potential centres that lay within the manually defined array would have 0 values for Δx and Δy. The sum of these values was then taken for each potential value using Equation 5-6.

$$\begin{bmatrix} \Delta x_1 \\ \Delta y_1 \end{bmatrix} + \begin{bmatrix} \Delta x_2 \\ \Delta y_2 \end{bmatrix} + \begin{bmatrix} \Delta x_n \\ \Delta y_n \end{bmatrix} = \begin{bmatrix} x_t \\ y_t \end{bmatrix}$$

Equation 5-6

Where x_t and y_t are an array giving the sum of all differences calculated using Equation 5-5, these values were calculated for each potential centre, the potential centre with the lowest values of x_t and y_t would fall within the manually defined array most often and was selected as the true artefact centre. This method was tested and proved successful in finding coordinates that were central to the circle. This was defined at the work piece centre for the image analysis.

5.4.5. Image intensity profile and calculating focal spot size

An image intensity profile is then plotted through the calculated centre in the X axis, from this profile points closest to the 50 % and 90 % thresholds on either side of the artefact are taken. The distance between the pairs is calculated, these values are then used in Equation 5-2, alongside the geometrical magnification which is calculated using Equation 5-1.

5.4.6. Index and repeat

The image is then indexed by n degrees specified by the user and the steps detailed in sections 5.4 are repeated until the image index angle is equal to 180 degrees, meaning a circular profile of the focal spot for the image is achieved. After the development of the automated method, it was found that the workpiece holding fixture used for initial method testing and validation caused significant anomalies in the results extracted as the line scan was passed across these values. The interference was due to the holding fixture being close enough to the 90% threshold that it would alter the distance between the pairs calculated in section 5.4.5 This led to the anomalous results seen in Figure 5-9. Attempts to create a "work around" in the script proved unsuccessful as manipulating pixel density resulted in interference with all pixel values, introducing new errors. A manual method was ruled out due to the increased time to adjust each image. As such adjustments were made to the work holding arrangement to prevent the results being skewed by the holding method.
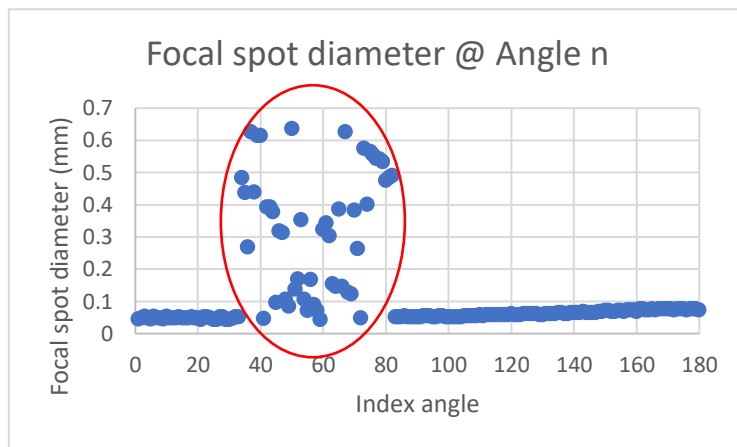
Figure 5-9 Focal spot measurements showing the spike caused in focal spot diameter(red), a result of unsatisfactory work holding.

A new holding arrangement of low-density foam was trailed which proved to give a more consistent grey scale throughout the image as can be seen in Figure 5-10. This adjusted work holding, lead to the poor results seen in Figure 5-9 being prevented in future measurements as seen in Figure 5-11.
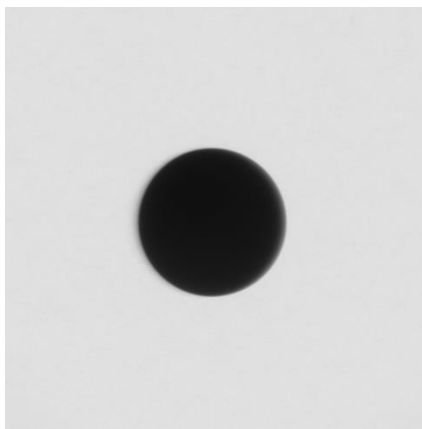
Figure 5-10 ball bearing suspended in low density foam, as an alternative to the polymer cone.
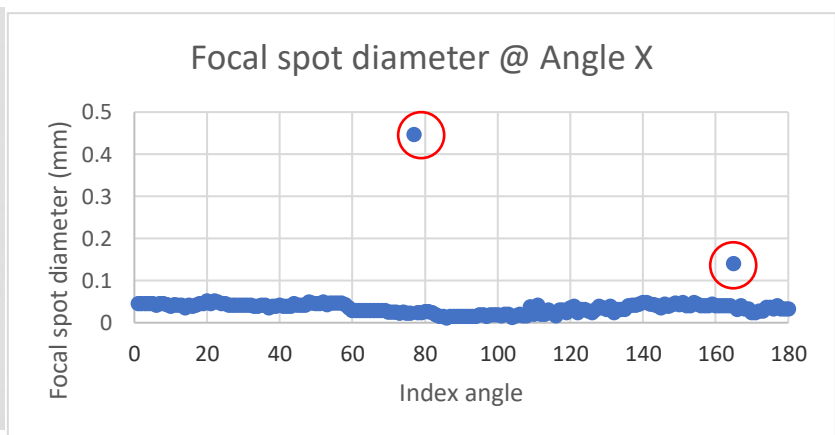
Figure 5-11 results from alternate work holding, whilst some anomalies remain (highlighted red) the precision of the results is significantly improved.

5.4.7. Method evaluation

The final script uses an automated variation of the method described by BS EN:12543-5 allowing for rapid analysis of the focal spot, to a higher level of complexity. Taking measurements in up to 180

planes instead of the 2 specified by the standard allows a comprehensive understanding of the dimensions and geometry of the focal spot. Initial testing generated results in keeping with expected focal spot size for the scan parameters used. These tests gave a focal spot 0.044 mm in the X axis and 0.014 mm in Y. This level of astigmatism is not uncommon in X-ray focal spots and electron optics. The method used in section 5.3.1.2 was repeated on the same image (Figure 5-10) and provided a measured focal spot of 0.058mm and 0.020 mm respectively. This is in line with the size and shape estimated using the automated method. The slight variation can be attributed to the manual method requiring the centre of the artefact to be manually assigned, introducing human error. The automated method prevents this, as the centre is found using a mix of fitted circles and image intensity analysis, explained in section 5.4.4. In comparison the automated method removes human error and produces values in line with existing standards. The method also takes a much greater number of measurements thus any calculated averages are likely more representative.

The focal spot can be measured using the developed method with a measurement uncertainty equal to the effective pixel size at a given magnification. Effective pixel size varies with magnification; thus, the measurement uncertainty of the method is dependent on the magnification of the scan. For example, at a magnification level 50 x the Nikon XT-H 225 reports a pixel size of approximately 4 microns, thus the uncertainty at this level is ±4 μm. However, at a magnification level of 10 x this increases to 20 microns. Variation in the focal spot smaller than the size of 1 effective pixel cannot be seen as a pixel cannot be accurately subdivided to give the required range in grey scale intensity values. The test scans used in the evaluation of the method were carried out at a magnification of 50 x meaning that the calculated results had an uncertainty of ±4 μm as noted.

Due to the inverse link between effective pixel size and magnification, for smaller focal spots it is advised to use a higher magnification when using the detailed procedure. In order to achieve a better resolution/smaller effective pixel size and thus a lower measurement uncertainty. As a machines focal spot size reaches the manufacturers quoted minimum of 3 μm, a magnification of 50 x would give an uncertainty greater than focal spot diameter invalidating the method (Nikon, 2022). As BS 12543-5, from which the novel method is derived, is suitable from 20 x – 100 x geometric magnification, the minimum achievable error in the method would be approximately 2 μm at 100 x magnification, in this machine. With the use of higher resolution detectors this could be further improved.

5.5.   Conclusions of Chapter 5

A novel method of focal spot measurement has been developed that allows the characterisation of focal spot geometry in 180 axis. This method is based on existing standards and produces results in line with those standards. The use of dedicated code increases the speed at which analysis of the focal spot is carried out. Characterisation of a focal spot can be achieved for either a single radiograph or as an average focal spot size across a scan or group of scans. The method also does not require large amounts of specialist equipment and can be integrated into simultaneous scans of other artefacts. This key requirement allows for the investigation of the hypothesised correlation between extracted areal surface texture parameters and focal spot variation.

In summary

- A novel method of focal spot measurement, based on and benchmarked against existing standards has been produced.
- The methods include automation of key processes to limit the possibility of introduction of human errors.

- The developed method can fully image the focal spot of a cone beam micro XCT in 180 axis rapidly, only requiring a single radiograph as an input.
- The method does not require any specialist or expensive testing equipment.
- The method can allow for the simultaneous scanning of a second artefact.

6. Investigating the link between focal spot dimensions and extracted surface texture parameters

The method developed in Chapter 5 was proven to produce realistic results for focal spot size in line with those gathered using the existing standard methods. For the present study the method was developed specifically for the simultaneous measurement of the focal spot and a surface artefact to allow any link or correlation between focal spot changes and dimensions/topography of the artefact to be established. It is hypothesized from the results in Chapter 4 that the changes in areal surface texture parameters noted by refocusing the machine between scans will be quantifiable and correlate significant change in the focal spot. Consequently, this led to the development of the method described in Chapter 5.

This chapter details the research completed with regards to developing an understanding of the link between focus, via quantified measurement of the focal spot, and the areal surface texture data parameters extracted from scans. The chapter is split into two sections, i) investigations around the focal spot when altering tube power and ii) inclusion of surfaces into the scan measuring the focal spot and the surface of an AM artefact.

Section 1 investigates the variation of X-ray power and includes both qualitive and quantitative data as power is altered. As noted, power is a key aspect in altering the focal spot size. The second section features the inclusion of two artefacts the ball measurement artefact and an additively manufactured part measured in situ during focal spot measurement, with scans taken before and after refocusing. Focal spot stability and extracted areas surface texture parameters were investigated individually before any correlation in changes between the two variables are analysed.

6.1. Variation of X-ray tube power

Prior to the inclusion of a second artefact into scans, further studies were carried out to investigate how the focal spot of a machine can affect scan quality. For this study the artefact used was the same ball bearing the method in Chapter 5 was designed around. Individual radiographs were taken as tube power was varied from 3 W to 10 W in 1 W increments. After this the auto-defocus setting was activated and further radiographs were taken at 15 W and 20 W. Auto-defocus is a setting that is recommended by Nikon to be activated when tube power exceeds 10 W, this is to prevent the electron beam damaging the target anode.

Theoretically as the focal spot diameter increases the accuracy of the measurement should decrease, due to geometric un-sharpness as noted in section 2.5.1. It was considered that the measured focal spot would be stable from 3-7 W in line with manufacturer specification. From 8-10 W variation in focal spot may be present but would be minimal as the machine would be still operating at the lower end of its operational window. With auto defocus implemented, the focal spot size was expected to increase significantly. Unlike its roots in medical imaging when used in industry XCT commonly is used to image and analyse denser materials, the materials require higher tube powers to penetrate necessitating analysis of how these power affect measurements.

The focal spot size may reach 0.225 mm according to the manufacturer constituting 22.5% of the diameter of the 1 mm artefact. It was thought that as the focal spot approached this size, it may be the case that a pattern could be established where focal spots of a size greater than a given percentage of features in a region of interest would mean XCT was unsuitable for accurately evaluating such a region.

6.1.1. Method

The method for this section comprised collecting radiographs generated at 1 W intervals from 3 to 10 W with a further two radiographs being taken at 15 and 20 W with auto defocus activated. All other settings were kept the same with 1000 ms exposure and a 140 kV tube voltage. Magnification was set at 50 X, within the bounds defined in BS12543-5 (BSI, 1999).

6.1.2. Results of varying tube power
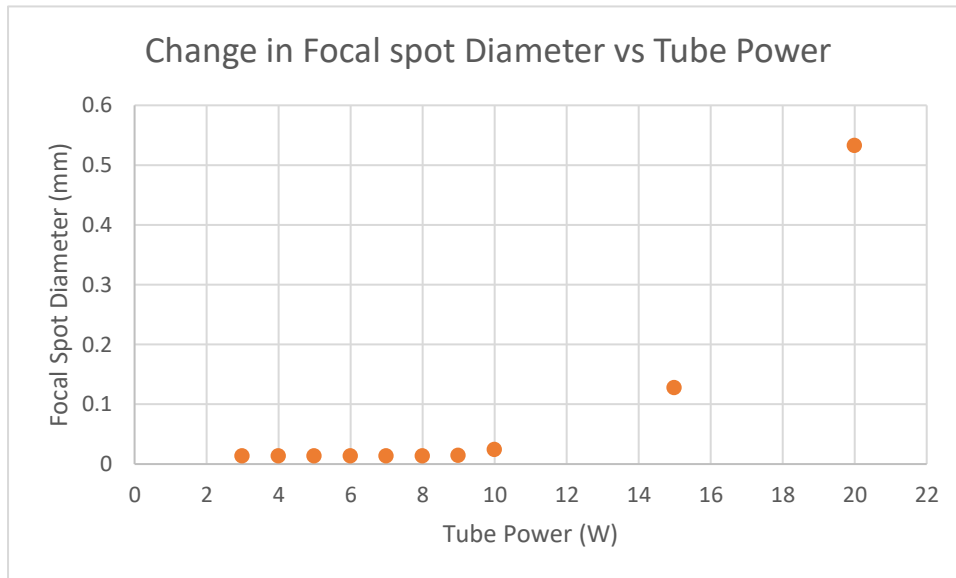
Figure 6-1 shows the increase in focal spot diameter due to the use of auto defocus

Figure 6-1 shows the increase of average focal spot diameter due to increasing tube power and where defocusing is applied.
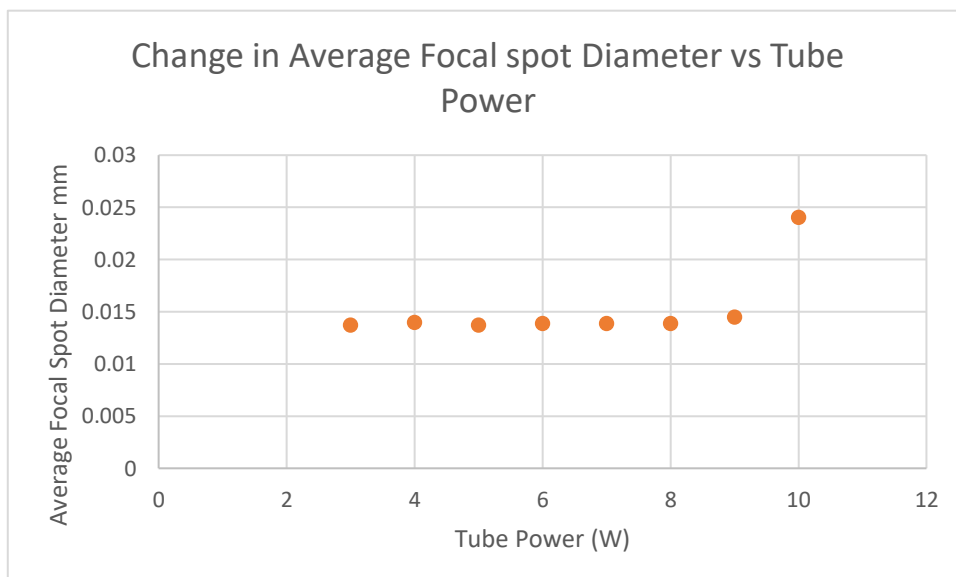
Figure 6-2 shows the increase in focal spot diameter with tube power exclduing results subject to auto defocus

Figure 6-2 shows the increases in focal spot diameter when staying below the 10W auto defocus threshold. When observing this in conjunction with the data in Table 6-1 it can be seen that very

little variation is present between 3-8 W which is inline and slightly better than the manufacturer specification for the machine. At 9 and 10 Watts there is a notable increase in average focal spot diameter though this is not of the same scale as when auto defocus is enabled.

Table 6-1 variation in average focal spot diameter (mm) due to increasing tube power (W)
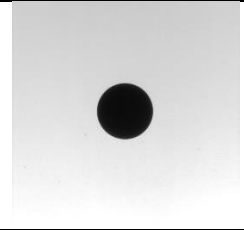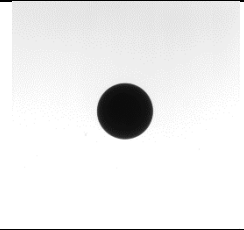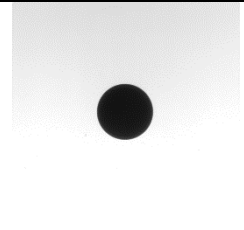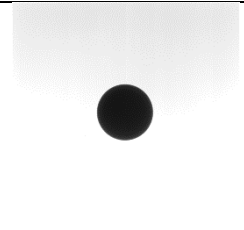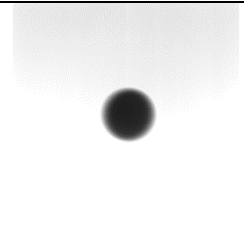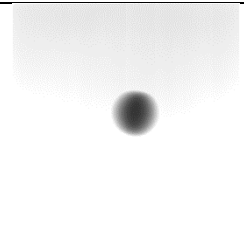
Power (W)	3	4	5	6	7	8	9	10	15	20
Focal Spot Diamter (mm)	0.0137	0.0139	0.0137	0.0138	0.0138	0.0138	0.0145	0.0240	0.1278	0.5327

The measured focal spot diameter at 20 W was highly unlikely to be representative, at this excessive tube power the image quality dropped below an acceptable level, due to a combination of increasing penumbra effect and a higher number of high-power X-rays penetrating the artefact completely. As the method is based on image analysis, if the geometric un-sharpness is too severe it is unlikely that realistic results could be attainted.

Qualitative analysis of the images themselves showed that the radiograph quality remained largely unaffected below 10W, as auto defocus was enabled image sharpness dropped and at 15 W the spherical artefact had lost some edge definition but was still recognisable, however at 20W the shape and position of the ball had changed enough to be considered unacceptable.

Table 6-2 shows shift in focal spot diameter and ball artefacts diameter as power (W) is increased

Power	Focal spot Diameter		Artefact diameter (ISO 50%)		Image
	X (mm)	Y (mm)	X (mm)	Y (mm)	
3 W	0.0117	0.0138	1.019	1.154	
4 W	0.0117	0.0138	1.019	1.154	
5 W	0.0117	0.0139	1.019	1.158	
6 W	0.0117	0.0104	1.019	1.158	

7 W	0.0117	0.0104	1.019	1.159	
8 W	0.0117	0.0140	1.019	1.159	
9 W	0.0157	0.0140	1.017	1.151	
10 W	0.0157	0.0138	1.017	1.152	
15 W	0.1346	0.0906	0.860	0.949	
20 W	*	*	0.124*	0.336*[1]	

From Table 6-2 it can be seen that focal spot stability below 10 W led to consistent measurement of the artefact, and that the focal spot remained stable throughout this range. At 15 and 20 W the auto defocus function was enabled, the greatly increased size of the focal spot meant that the diameter as measured using 50% of the intensity value, was significantly decreased.

At 20 W reasonable results for focal spot and artefact diameter could not be achieved, highlighting this, is the radiograph taken at 20 W (Table 6-2) which displays high geometric un-sharpness. At high

[1] Due to a high level of anomalous data, measurement of the focal spot and artefact at 20 W proved difficult with the results not being representative of the true geometry of either. An estimate is given in the text, thought this is not likely realistic.

levels of geometric un-sharpness, the method appears prone to error, measuring the average diameter of the focal spot at 20 W as 0.533 mm, twice the given value for maximum focal spot size of the machine given by the manufacturer (Nikon, 2022).

The measured diameter of the ball bearing was calculated at 0.124 mm in X and 0.336 in Y. These values, outside of this study would be unrepresentative of the geometry of the ball and highlight that prior to initiating an XCT scan and to obtain high quality dimensional data, users should have a good estimation of the expected results, as previously discussed in section 4.4.

The decrease in "measured" artefact diameter also led to the hypothesis that as focal spot size increases, the minimum detectable feature size also increases. This is supported by the theory surrounding the penumbra effect (2.5.1) and it is thought likely that larger focal spot sizes would lead to an indirect form of data filtering. With further work in the field, it is hypothesised that it may be possible to establish a ratio between focal spot size and resolvable scale. Such a ratio would be a useful guide for end users, though a study of this scale is outside the scope of the current work.

6.1.3. Summary of measured variation in tube power

As discussed, variation of the tube power and associated focal spot size of a Nikon XTH 225 machine was carried out and measured using the novel method described in section 5.4. This method allowed the evaluation of the diameter of the focal spot. Results were in line with both the manufacturers specifications and previous work indicating a positive dependence between focal spot size and tube power (Nikon, 2022) (Hiller, Masil, & Reindl, 2012). As focal spot size increased the measured diameter of the ball artefact decreased, at high powers this was significant enough to result in inaccuracy in the method of measurement itself. This indicated that the method was suitable only when operating within a specific envelope. Exceeding the bounds at which the method can image the ball artefact to an acceptable certain degree of accuracy lead to inaccurate focal spot measurement due to high levels of geometric un-sharpness and this led to the conclusion that as the focal spot approaches a given percentage of the dimensions of features of interest, the ability to accurately resolve those features is diminished.

It is of note that the variation in measured focal spot diameter seen from 3-8 W beam power does not exceed the measurement uncertainty of ±4 µm of the method developed in the previous chapter with results showing sub-micron variation as power increases in this range. The stability of the results in this section matches the manufacturer specification as the beam is not automatically defocused in the 3-8 W range, meaning that the focal spot diameter should not change significantly. If the focal spot geometry is stable in this range as indicated, it in turn indicates a high level of repeatability for the method.

6.2. Simultaneous scanning study

A study comprising of the simultaneous scanning of both the ball artefact used throughout the chapter and an AM surface was planned. This study hoped to quantify how the changes observed throughout Chapters 3 and 4 were reflected in the XCT focal spot dimensions and part geometry. It was hypothesized that a link could be found between the two. Section 6.1 has already established that as focal spot size increased geometrical measurements taken using the XCT would inversely decrease due to the geometric un-sharpness. This led to the hypothesis that when using a higher focal spot size, a significant level of unintended filtering may occur. As the previous studies, shown in Chapter 4 had noted variation in extracted surface topography results after just refocusing the machine, the planned study would first investigate how scans taken using identical parameters were affected by the machine being refocused.

6.2.1. Simultaneous scanning methodology

Alongside the ball artefact, a second surface artefact would need to be selected, an appropriate artefact would allow for the simultaneous scanning of both the focal spot and artefact surface to be achieved. Considerations were made such that the level of magnification was within the acceptable range described in BS EN 12543-5, the standard the focal spot measurement method the present work
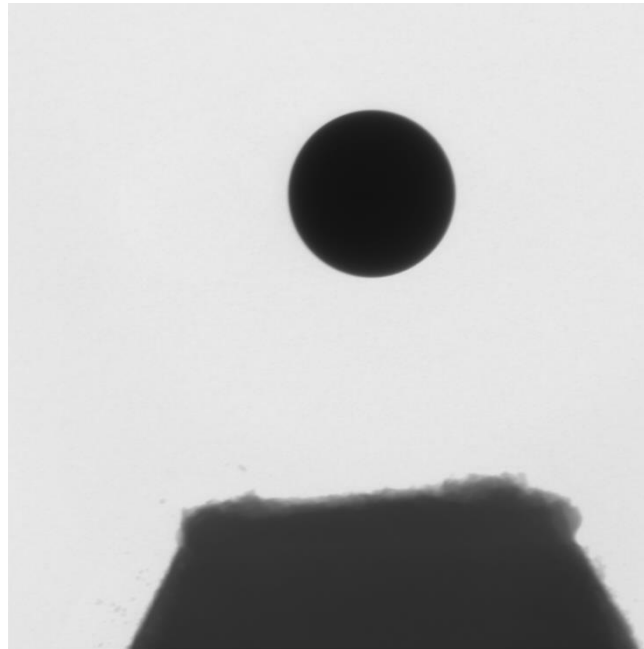
Figure 6-3 individual radiograph of the ball and surface artefacts.

is based upon. Both the artefact and surface were required to be visible throughout the scanning routine, as such a large artefact would prove non-viable. Thus, a small additively manufactured selective laser sintered (SLS) Inconel artefact was selected as the surface artefact. From testing, the maximum magnification achieved whilst still providing useable data for both artefacts was 50 X, this can be seen in Figure 6-3. This was in line with the magnification used during the development of the method, meaning no adjustments or additional testing was necessary.

Two groups of scans were to be taken; the first 5 scans (group 1) were taken prior to the machine being refocused. These scans would be followed by a refocusing of the machine using the process described in section 4.1 and in line with manufacturer recommendations. After the machine was refocused to a suitable standard, a second group (group 2) of 5 measurements were taken. The measurements would be taken of the ball and surfaces artefacts simultaneously. To prevent the introduction of errors due to work holding as previously noted in Chapter 5, both materials would be suspended in low density foam.

Scanning parameters were set to 170 kV tube voltage and 3.4 W tube power, exposure was set to 2829 ms, no filter was used as this would introduce an extra variable in the method. This led to a clear image of the surface and ball artefact seen in Figure 6-3.

For analysis, the focal spots were measured intermittently throughout each scan, totalling 11 measurements per scan. This meant every 144th image would be processed. Images were processed using the method developed in Chapter 5, to prevent the introduction of errors from the surface artefact all images were cropped prior to analysis.

All surfaces were trimmed to prevent lengthy processing times, aligned to a randomly selected master using Cloud Compare after which the files were exported as .ply format. For this study areal surface roughness parameter data was be extracted using DigitalSurf Mountains.

6.2.2. Simultaneous scan results

6.2.2.1. Focal spot diameter

Initial analysis of the focal spot diameter showed a measurable shift in results between scans taken before and after the machine refocusing. Focal spot stability was also investigated, and scans taken in the post refocusing exhibited better stability from scan to scan. Both the shift in focal spot diameter and change in focal spot stability can be seen in Table 6-3.

Table 6-3 compares focal spot measurements of two groups taken pre and post refocusing the machine.

	Focal Spot Diameter (mm)					
Scan	1	2	3	4	5	Average
Group 1	0.0290	0.0250	0.0224	0.0225	0.0213	0.0240
Group 2	0.0201	0.0185	0.0199	0.0191	0.0199	0.0195

Across a single scan focal spot stability was also evaluated, for each set the diameter was measured in x and y being the width and height of the spot respectively. Examples of these measurement are given in Figure 6-4 and Figure 6-5. The stability of the Focal spot in Figure 6-4 shows that there is a growing astigmatism throughout the scan this could be due to the guns thermal drift as the electron optics coils and filament heating up and moving the electron beam out of focus, though other factors could also impact the stability of the spot such as the initial focusing of the gun.
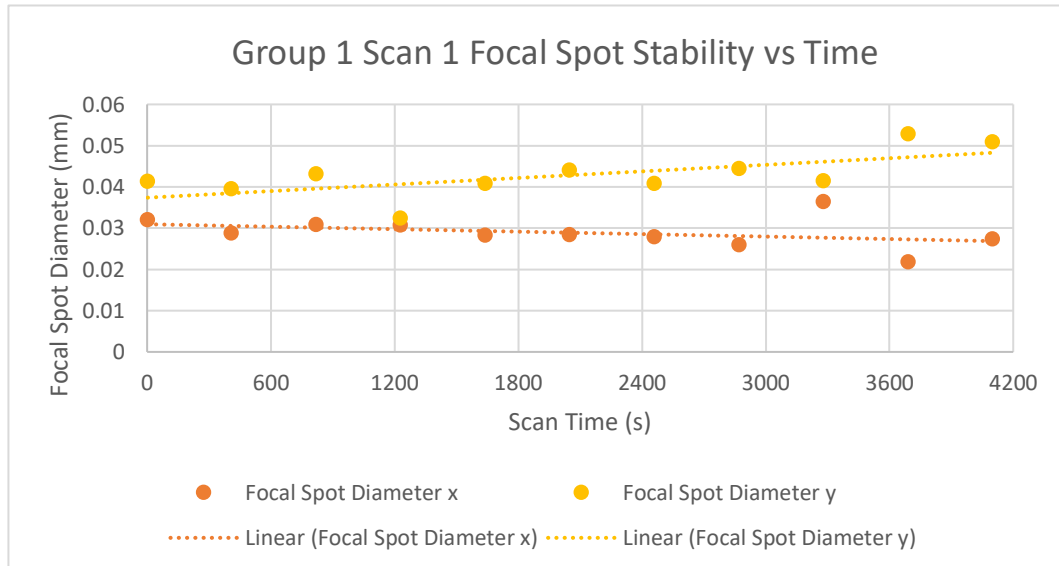
Figure 6-4 shows the change in focal spot dimensions over a single scan from group 1

Figure 6-5 shows the same data for the first scan of group 2, the spot again shows an astigmatism as with the first data set being biased in the y direction, the spots stability is generally better over the time of this can and the astigmatism is seen to be decreasing slowly. When comparing the first and last measurements of each data set the scan from Figure 6-4 has an increase in y of 10 µm compared to a decrease of 1µm in the data shown in Figure 6-5. In x the 1st data set shows a decrease of 5 µm whereas the data in Figure 6-5 only shows a shift of 2 µm, the data presented in Figure 6-5 shows the machine is more stable across the scan from group 2. The greater stability could be due to the gun

already being close to a thermal equilibrium due to use prior to the scan meaning the focal spot was not drifting due to thermal expansion. The focal spot is shown to be more geometrically stable in group 2 in both Table 6-3 and Figure 6-4 and 6-5.
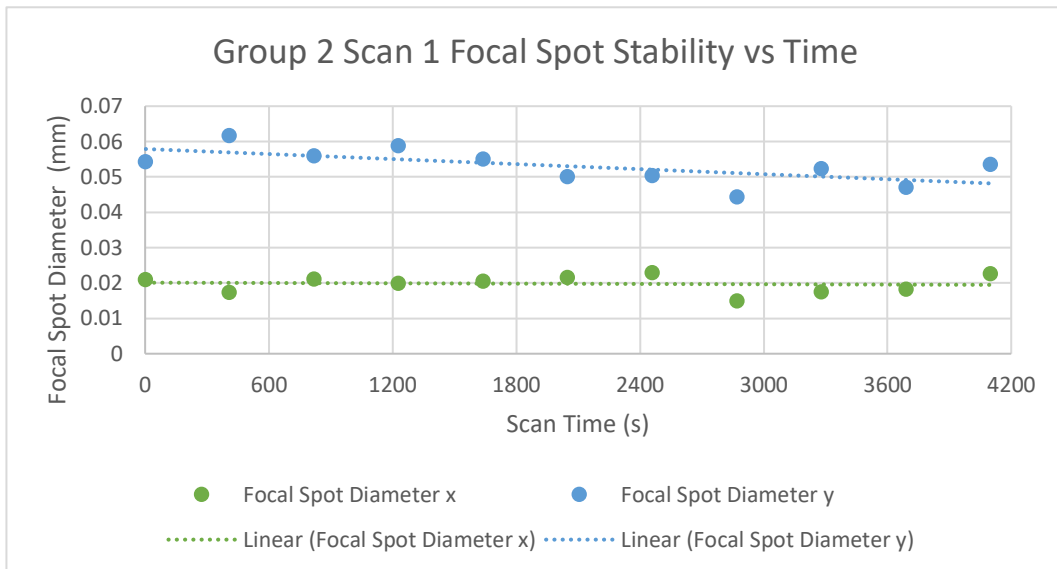
Figure 6-5 shows the change in focal spot dimensions over a single scan from group 2

Analysis of the Inconel surface artefact used in the study was carried out in DigitalSurf Mountains analysis of the surface itself proved unremarkable; the surface showed characteristic features of an SLS AM part that had not be subjected to post processing. Visual analysis performed during the alignment of all surfaces to a predetermined master showed little notable variation between scans, example data is shown in Figure 6-6.
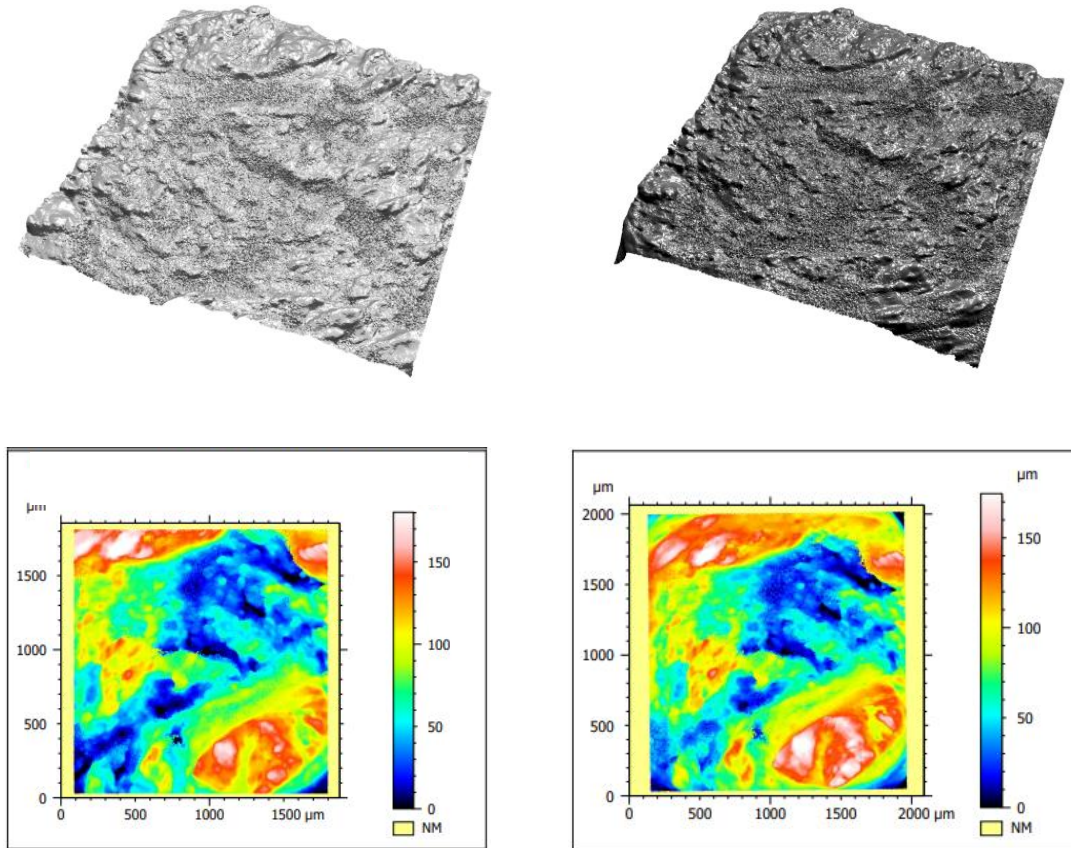
Figure 6-6 (clockwise from the top left) 3D surface view of group 1 scan 1, 3D surface view of group 2 scan 5, pseudo colour height map of group 2 scan 5 , psuedo colour height man of group 1 scan 1

Extracted surface parameters showed minor variation from scan to scan for Sq, Sa, and Sdr with a larger level of variation seen between the two groups for these parameters this observed variation was similar to that highlighted in Chapter 3 with a variation of less than a micron between individual scans and a larger shift between the two groups, this data is presented in Figure 6-7 and Figure 6-8.
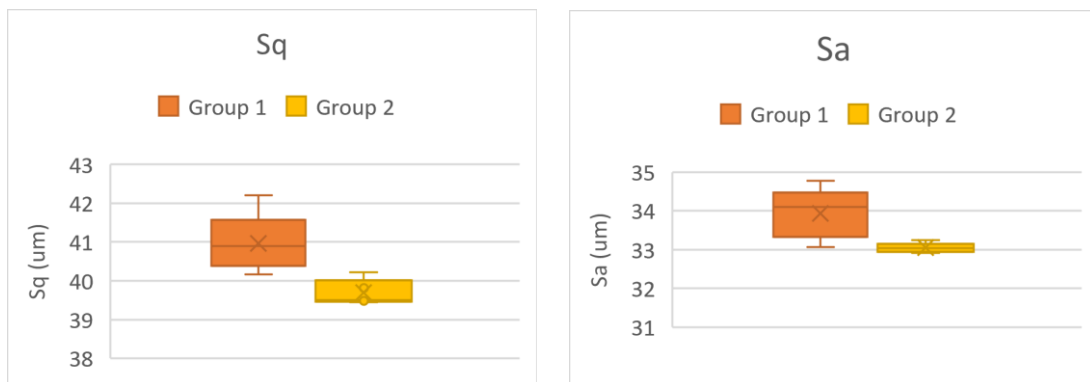
Figure 6-7 shows Sq (left) and Sa (right) prior to and after refocusing
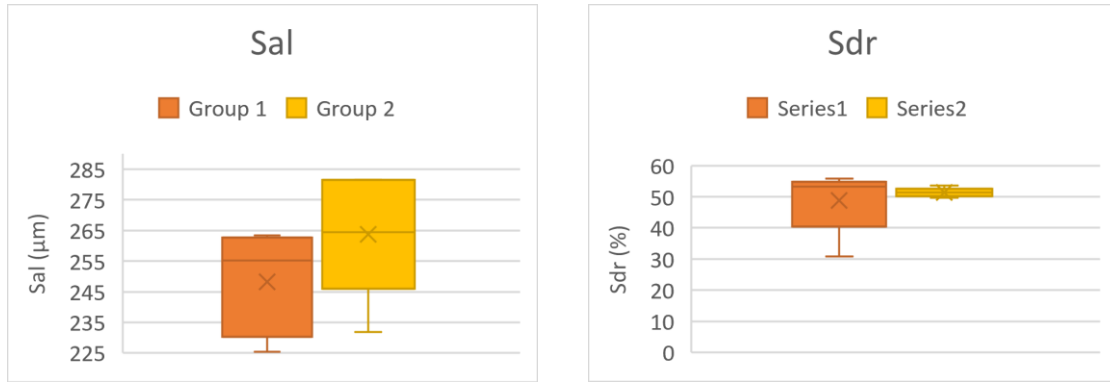
Figure 6-8 shows Sal (left) and Sdr (right) prior to and after refocusing

For Sal variation from scan to scan and variation between the two groups is comparable though there has been shift in the mean value between the two data sets of 15 μm. The Sal parameter is a numerical index of the density of structures in units of length, as the value increases it indicates the feature size on a surface is increasing. Whilst a shift of 15 μm does not indicate a huge change in the surface the definitive increase in mean does still indicate a shift between the two groups.

Comparisons of Sq, Sa, Sal and Sdr all followed this pattern similar to results noted in Chapter 4. It is interesting to note that for Sal the results in group 2 were higher, all other gathered parameters tended to show the values for group 2 being lower or approximately equal to the values extracted from group 1.

This was the only parameter where group 2 was consistently higher in value. However, when analysing Figure 6-7 and Figure 6-8, much lower levels of variation are present for all data sets in group 2. Correlation between the levels of variation between focal spot diameter and surface texture were carried out due to this.

6.2.2.3. Investigation of a link between shifts in areal surface texture parameters and focal spot diameter

When observing the two data sets of extracted areal surface texture parameters and focal spot diameter. As noted previously, the variance of data for group 1 was larger across almost all measured parameters, including focal spot diameter (Table 6-4).

Table 6-4 shows average focal spot diameter and variance in relation to extracted areal surface texture parameters of both groups

	Scan	Focal Spot Diameter (mm)		Sq (μm)	Sa(μm)		Sal(μm)		Sdr (%)
	Average	0.024		40.964	33.940		248.240		48.750
Group 1	Variance	7.56E-06		0.465	0.329		231.862		83.096
	Average	0.020		39.694	33.046		273.840		51.362
Group 2	Variance	3.84E-07		0.087	0.013		92.290		1.647

The shift in areal surface texture parameter between the two groups, is in alignment with that originally noted by Townsend et. al. and demonstrated further in section 3.3 (Townsend, Pagani, Scott, & Blunt, 2017). There is a clear shift in measured focal spot diameter and furthermore in the stability of the focal spot with greater variation being seen in the first group. It also appears there is greater

stability in extracted surface texture parameter results in group 2 as can be seen with the lower variance. This indicates a possible link between focal spot stability and extracted areal surface texture parameter, highlighting a possible issue with XCT as an unstable focal spot may be difficult to assess and thus cause unwanted variation. However further work would be needed in this area.

The shift in results is small and significance of the variation may be heavily dependent on use, however there is evidence to support a link between focal spot diameter and extracted surface texture parameters. The amplitude parameters (represented by Sq and Sa) show a noticeable positive reliance of focal spot diameter, whereas spatial parameters (Sal) show an increase due to a possible smoothing/filtering effect. The hybrid parameter (Sdr) on the other hand shows a reduction with the smoothing/filtering effect.

When assessing how shifts are mirrored in results from individual scans and how this affected extracted surface parameters it can be seen that the two groups show differing patterns. Group 1 (Figure 6-9) shows a large variation in focal spot size across the group, extracted areal surface texture parameter results also show this but there is no clear pattern between focal spot diameter and extracted surface texture parameters.

The amplitude and hybrid parameters follow somewhat sinusoidal pattern but there is little change in focal spot that can be linked to this.
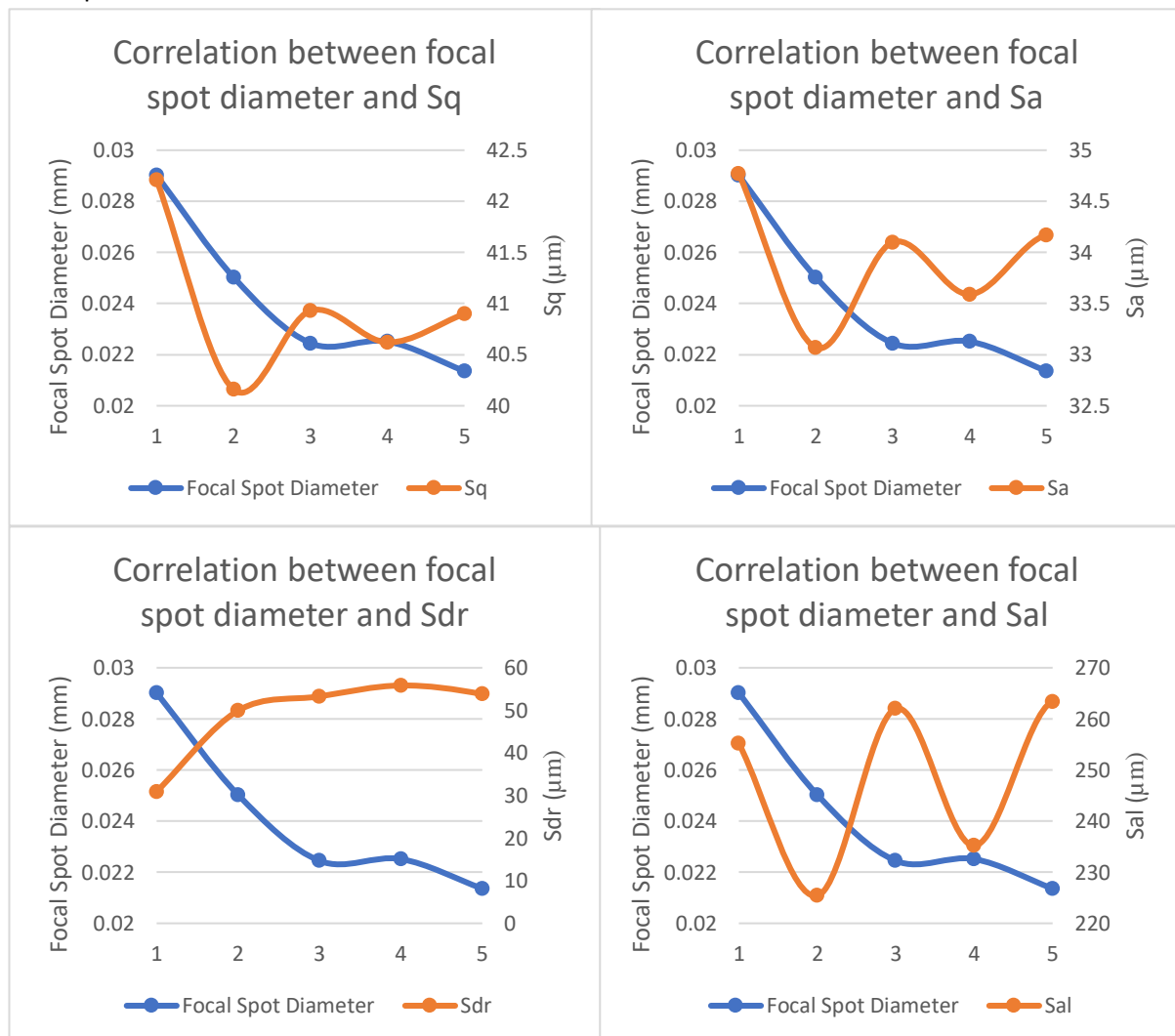
Figure 6-9 shows focal spot diameter results vs varying areal surface texture parameters (group 1)

When observing the same graphs for Group 2 (Figure 6-10) a much stronger link can be seen between focal spot diameter and extracted areal surface texture parameters. As the focal spot diameter rises both Sq and Sa follow the same pattern, this is representative of all amplitude parameters. Sdr the hybrid parameter in this instance also follows this pattern. Spatial parameters represented by Sal, follow an inverse phenomenon to other results as can be seen in Figure 6-10 as the focal spot diameter increase Sal decreases.
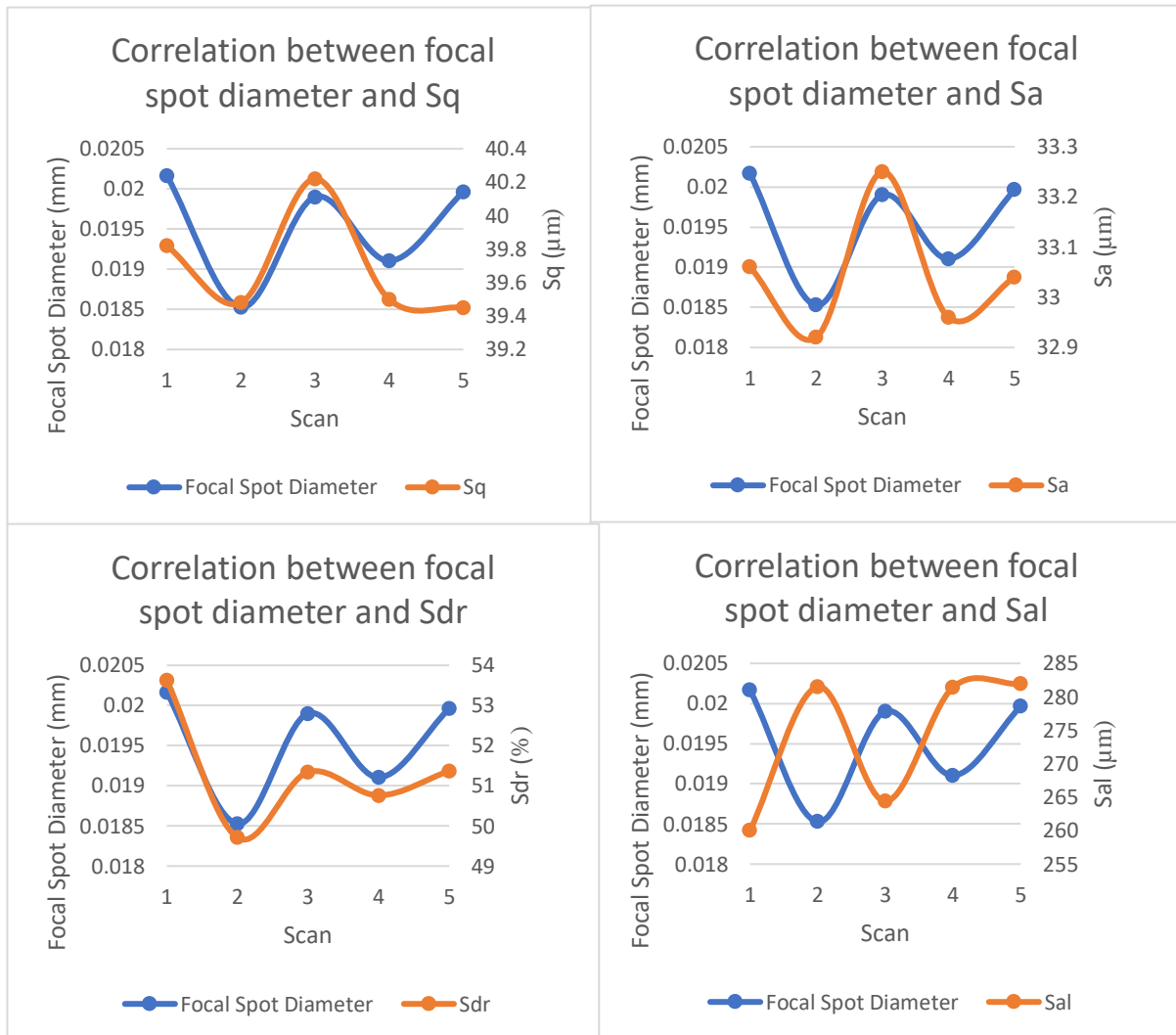
Figure 6-10 shows focal spot diameter results vs varying areal surface texture parameters (group 2)

The stability of the focal spot over a single scan was shown in section 6.2.2.1 to be greater for Group 2, this may be linked to the better correlation between focal spot diameter and surface texture parameters. It is hypothesised a more consistent X-ray source would mean less variation between individual radiographs due to the penumbra effect. As the surface parameters are extracted from a 3-dimensional model reconstructed from all radiographs it could prove significant if there was variation between radiographs.

6.3. Summary of investigations into the link between focal spot diameter and extracted surface texture parameters

Comparison between the two groups shows the difference between the extracted areal surface texture parameters follows pre-existing patterns established in Chapter 3. The clear pattern in group 2 is not as present in the results group 1. The instability of the focal spot diameter measured in group 1 does however correlate with an increased measured variance in areal surface texture parameters. It is hypothesised this may be linked, and that as focal spot stability improves, small shifts in focal spot diameter may result in comparatively small shifts in extracted areal surface texture parameters as seen in group 2. In comparison scanning with a focal spot that is unstable i.e. with a diameter showing large amounts of fluctuation, could lead to larger variation in areal surface texture parameters.

6.4. Conclusions of Chapter 6

The novel methods developed in Chapter 5 and used in Chapter 6 proved effective in measuring the focal spot of the cone beam machine tested. Measurement of the focal spot at different tube powers showed that as power increased focal spot diameter also increased, this fell in line with current literature (Hiller, Masil, & Reindl, 2012). Focal spot stability under 10 W was generally good as specified by the manufacturer however the best value given for focal spot was not achieved and a consistent astigmatism was present in the machine (Nikon, 2022). When measuring the diameter of the artefact used to measure the focal spot, it can be seen that as focal spot diameter increases, the measured ball diameter decreased. This was in line with previous work and theory surround geometric un-sharpness and the penumbra effect described in section 2.5.1 (Flay, 2016). The method of focal spot measurement was prone to error at very high powers, where electron beam defocusing was applied to prevent damage to the target. This inaccuracy was due to the geometric un-sharpness being too great for accurate measurement of the ball artefact. This not only limits the method but shows that measurements taken at high power may lead to inaccurate scan data.

Simultaneous scanning of both the focal spot and surface artefact confirmed that a change in focal spot geometry was present after a refocus, the diameter of the focal spot was measured to vary over this process as did the extracted surface texture parameter results. Data from group 2 of the simultaneous scanning study correlated that as focal spot size increased and decreased extracted surface parameter results by majority, mirrored this, though spatial parameters showed an inverse relationship possibly resulting from spatial filtering. The measurement of the focal spot in group 1 showed much greater levels of variation, the changes in focal spot diameter were not mirrored in extracted areal surface texture parameters.

In summary

- The conclusion of Chapter 4 that re focusing the machine is the cause in variation in areal surface texture parameters is further supported.
- The new novel method has shown it is possible to extract areal surface texture parameters alongside measurements of the focal spot.
- The method has produced results in line with theory surrounding geometric measurement of the focal spot.
- It appears likely a relationship exists between focal spot diameter and extracted areal surface texture parameters, though further work is needed to full categorise this relationship and how each parameter type (amplitude, spatial or hybrid) may vary.

7. Conclusions

The development of XCT as a tool in the field of surface metrology, has led to the need for a greater understanding of how errors specific to the field may affect results gathered using the technique. XCT is unlike any other method of gathering data existing in the metrology and further NDE applications, as by using X-rays to image an artefact a 3D model of both the internal and external structure can be imaged in detail. The use of X-rays though introduces a new swathe of errors sources, these must be investigated and quantified before XCT can be seen to move towards the traceability of more established methods of measurement.

The results presented in this work have investigated a series of the sources of error unique to XCT and a novel method able to quantify some of the effects of the errors sources in alignment with real world measurements has been developed.

7.1. Primary conclusions

- **The focal spot variation of a cone beam XCT machine affects areal surface texture parameter results extracted using XCT.**
    - In Chapter 6 the focal spot diameter is measured alongside a surface artefact these measurements show that if a focal spots diameter is unstable and varies over the course of a series of scans this variation carries through to the extracted areal surface texture parameter.
    - Alongside this, any scan to scan variation in focal spot diameter from a single focusing operation shows as small shifts in extracted areal surface texture parameters, this variation is individual to the family of parameters that correlates closely with the change in diameter.
- **When refocusing an XCT after a filament change a clear shift in extracted areal surface texture results can be observed.**
    - The shift in extracted areal surface texture parameters after a filament change was investigated in Chapter 3 under the assumption that the filament's changing condition throughout their useful life was linked to shift in extracted areal surface texture parameters, this was disproved in a series of studies included in the chapter.
    - In Chapter 4 the focus of the investigation shifted to look at the act of alignment and refocusing, a part of the filament installation process. Studies found that variation in extracted areal surface texture parameters could be observed when refocusing the machine, these shifts matched changes shown in the previous chapter. This indicated the shifts seen in Chapter 3 were linked to the focusing procedure as well.
- **A novel method of focal spot measurement has been developed with the benefit that it can be included into scans measuring other artefacts simultaneously.**
    - A need to quantify how machine focus effected extracted areal surface texture parameters led to the development meant of a novel method to measure both variables simultaneously.
    - This method accomplished simultaneous measurement of both artefacts, its development being detailed in Chapter 5 and results gathered using the new method being presented in Chapter 6.

7.2. Secondary conclusions

- As an XCT filament degrades during its useful life there is no measurable variation or pattern in areal surface texture parameter results extracted from scans during this time.

- Accuracy of areal surface texture parameter extracted from XCT does not decrease at any point during a filament's useful life.

- Small shifts in the average pixel intensity of the background or material do not correlate with any pattern seen in extracted areal surface texture parameters.

- There is currently a small variation in extracted areal surface texture parameter results between scans taken under identical conditions and processed identically.

- XCT users should be aware that when using XCT machines for surface analysis, that if not working within an ideal operating envelope, results gained can be significantly incorrect as seen in section 4.4 where a nominally "focused" machine provided a scan consisting primarily of noise and thoroughly unrepresentative of the object scanned. This is also seen in section 6.1.2 where a scan of a ball bearing appears heavily distorted due to using an unsuitably high tube power.

- Under ideal circumstances an XCT user should have a "general" idea of how the expected scan should appear as otherwise errors such as those described may go unnoticed.

- Development of XCT as a tool of surface metrology requires further development, calibration of machines should be the forefront of this research to help establish traceability. Only after this has been achieved can the true potential of the technology be achieved.

7.3. Contribution to knowledge

- Investigation into the repeatability of XCT has been carried out. The extracted areal surface texture parameter data presented demonstrates the repeatability of and variation present when using XCT as a tool for the analysis of surface topography. Future users can use this data to better understand how scans taken under "identical" conditions may vary. Work should continue to build upon this to develop a thorough understanding of the precision achievable using XCT for large scale data gathering.

- Refocusing of an XCT machine has been shown to cause a quantifiable shift in areal surface texture parameters gathered using XCT, the significance of the shift is application dependent. Any XCT user taking surface measurements using the technology, should be aware that refocusing the machine can introduce these errors.

- A novel method of measuring the focal spot has been developed that can allow for the simultaneous measurement of a second artefact, this method has been used to show the existence of a possible link between the diameter/stability of the focal spot and extracted surface texture parameters.

7.4. Future work

7.4.1. Comparison of results across a range of cone beam XCT systems

The novel method developed in Chapter 5 was developed using results gathered form a Nikon XTH 225 machine, and all results gathered using the method are most relevant to this system. The method is not machine specific and only a few changes to inputs surrounding pixel and image size would be required to gather similar results from a range of machines. Studies similar to that detailed in Chapter 6, are required on a machine specific basis if users want to better understand how the results presented relate to different machines. The method could be applied to any cone beam machine of which a focal spot not lower than the manufacturing tolerances of the ball artefact used. Focal spots smaller than this would require a more precise artefact.

7.4.2. Integration into standard practise

A method of focal spot measurement, integrated into the focusing procedure of an XCT would provide a way by which the focus of the machine could be examined and quantified each time the procedure was performed. If procedures were established that set a minimum acceptable focus level at a given range of scanning parameters, the accuracy and precision of scans could be greatly improved. Calibration artefacts are typically expensive equipment, but the artefact required by BS EN 12543-5 is comparatively cheap and the method developed in Chapter 5 is a development on this method which gathers an increased number of results and automates the procedure entirely. This makes it the ideal candidate for integration into the focusing procedure of non-specialised cone beam XCT.

7.4.3. Investigation into how focal spots affect specific parameters

As shown in Chapter 6, the extracted areal surface texture parameters appear dependent on the focal spot diameter, this variation however is not uniform. Further study should be undertaken using the methods developed in this work to investigate how variation to the focal spot can cause changes in the specific extracted areal surface texture parameter groups. Work should be split to assess individual changes to spatial, hybrid and functional parameters, assessing how geometrical un-sharpness due to changes in focal spot geometry propagate into these measurements.

8. Appendix

8.1. References

European Society of Radiology. (2013). *THE STORY OF RADIOLOGY.* 2013 Vienna: European Society of Radiology.

International Organization for Standardization. (2012). *ISO 25178-2:2012.* Retrieved from https://www.iso.org/: https://www.iso.org/standard/42785.html

Abdulla, S. (2021). *CT artefacts*. Retrieved 03 23, 2022, from https://www.radiologycafe.com/frcr-physics-notes/ct-imaging/ct-artefacts/

Addinall, K., Townsend, A., & Blunt, L. (2019). The use of X-Ray Computed Tomography to investigate modification in firearms. Krakow: 26th Annual Meeting of ENFSI Firearms and GSR working group.

Agar Scientific Ltd. (2014, Jan). *Agar Filaments for Cambridge, LEO, Zeiss & AEI.* Retrieved from www.agarscientific.com: https://www.agarscientific.com/agar-filaments

Alvarez, R., & Macovski, A. (1976). Energy-selective Reconstructions in X-ray Computerized. *Phys Med, 21*(5), 733-744.

AXT PTY Limited. (2021). *PrismaXRM*. Retrieved 03 22, 2022, from https://www.axt.com.au/products/prismaxrm-micro-ct/

Badea, C. (2021). *Molecular Imaging.*

Bam, L., Miller, J., Becker, M., & de Beer, F. (2016). X-ray Computed Tomography – Determination of Rapid Scanning Parameters for Geometallurgical Analysis of Iron Ore. Perth: Proceedings of the 3rd International Geometallurgy Conference.

Beckman, E. C. (2006). CT scanning the early days. *The British Journal of Radiology, 79*(937), 1-89.

Becquerel, E. (1853). Rescherches Sur La Transmission De L'Electricite Au Travers Des Gaz A Des Temperatures Elevees. *Annales de Chimie et de Physique, 39*, 48.

Becqurel, E. (1839). Memopire sur les effets electriques produits sous l'infuence des rayons solaires. *Académie des sciences*, 561–567.

Bock, R., Hoppe , S., Scherl , H., & Hornegger, J. (2007). Beam Hardening Correction with an Iterative Scheme Using an Exact Backward Projector and a Polychromatic Forward Projector. *Bildverarbeitung für die Medizin* , 46-50.

Bosmans, H., Carton, A.-K. K., Rogge, F., & Zanca, F. (2005). Image quality measurements and metrics in full field digital mammography: An overview. *Radiation Protection Dosimetry*, 120-130.

British Institute of Radiology. (2022). *Origins of radiology*. Retrieved from British Institue of Radiology: https://www.bir.org.uk/useful-information/history-of-radiology/origins-of-radiology.aspx

British standards institute . (2012, 04 30). *BS EN ISO 25178-2:2012*. Retrieved from bsol-bsigroup-com: https://bsol-bsigroup-com.libaccess.hud.ac.uk/Bibliographic/BibliographicInfoData/000000000030154352

BSI. (1999). *12543-5: Non-destructive testing-Characteristics of focal spots in industrial X-ray systems for usie in non-destructive testing.* Brussels: BSI.

Chahid, M., Townsend, A., Liu, A., Bills, P., Sperling, P., & Racasan, R. (2020). Optimizing X-Ray Computed Tomography Settings for Dimensional Metrology Using 2D Image Analysis. *Structural Integrity of Additive Manufactured Materials and Parts*, 88-101.

Chahid, Y., Townsend, A., Liu, A., Bills, P., Sperlign, P., & Racasan, R. (2020). Optimizing X-Ray Computed Tomography Settings for Dimensional Metrology Using 2D Image Analysis. In N. Shamsaei, & M. Seifi (Eds.), *Structural Integrity of Additive Manufactured Materials & Parts.* ASTM.

ChinaTungsten . (2009). *Properties of tungsten wires*. Retrieved from http://www.tungsten-wire.com.cn/: http://www.tungsten-wire.com.cn/the-properties-of-tungsten-wire.html

Chotas, H., Dobbins, J. I., & Ravin, C. (1999). Principles of digital radiography with large area, electronically readable detectors: a review of the basics. *Radiology, 210*, 595-599.

Clayton, D. (1983). *Principles of stellar evolution and nucleosynthesis : with a new preface.* Chicago: University of Chicago Press.

Compton, A. H. (1923). A QUANTUM THEORY OF THE SCATTERING OF X-RAYS. *The Pyshical Review*, 483-502.

Consultative Committee for Length. (2019). *Mise en pratique for the definition of the metre in the SI* (9th ed.). Sevres: Bureau International des Poids et Mesures.

Digital Surf. (22). *Digital Surf*. Retrieved 04 27, 22, from https://www.digitalsurf.com/

Dowdy, J., Murray, R., & Christensen, E. (1990). *Christensen's Physics of Diagnostic Radiology.*

Ed Fagan Inc. (2020, 6 10). *Tungsten-Refreactory Metals and Alloys.* Retrieved from https://www.edfagan.com/: https://www.edfagan.com/wp-content/uploads/2020/06/Tungsten_6-10-20.pdf

Einstein, A. (1905). Does the inertia of a body dpend upon its energy-content? (English Translation). *Annalen der Physik, 18*, 639.

Elliot, J. C., & Dover, S. D. (1982). X-ray microtomography. *Jorunal of Microscopy, 126*(2), 211-213.

Elmet Technologies. (2021). *TUNGSTEN WIRE*. Retrieved from https://www.elmettechnologies.com/: https://www.elmettechnologies.com/tungsten/tungsten-wire/

Fano, U. (1947). Ionization Yield of Radiations. II. The Fluctuations of the Number of Ions. *Physical Review, 72*(1).

Ferrucci, M., Leach, R., Giusca, C., Carmignato, S., & Dewulf, W. (2015). Towards geometrical calibration of x-ray computed tomography systems—a review. *Measurement Science and Technology, 26*(9), 1-30.

Ferucci, m. (2018). Towards Traceability of CT Dimensioanl Measurments. In S. Carmignato, W. Dewulf, & R. Leach (Eds.), *Industrial X-Ray Computed Tomography* (pp. 229-266). Springer.

Flay, N. (2016). *An investigation of the factors associated with the X-ray tube and their influence on dimensional measurement in micro-focus cane-beam industrial X-ray computed tomography systems.* Southhampton: University of Southampton.

Flemming, A. (1934). On the history and development of the thermionic valve. *REPORT OF A DISCOURSE GIVEN AT THE TWENTY-FOURTH ANNUAL EXHIBITION OF THE PHYSICAL SOCIETY*, 44-49.

Garbout, A., Sturrock, J., Armenise, E., Ahn, S., Simmons, R. W., Doerr, S., . . . Mooney, S. J. (2018). TopCap: A Tool to Quantify Soil Surface Topology and Subsurface Structure. *Vadeose Zone Journal*, 1-10.

Giacomuzzi, S., Springer, P., Stohr, B., & Schreder, J. (1998). Gustav KAISER an early Austrian Röntgen Pioneer: A Late Appreciation. *Ber. nat.-med. Verein Innsbruck*, 363-368.

Gilboy, W. (1984). X- and Y-Ray Tomogoraphy in NDE Aplications. *Nuclear Instruments and Methods in Physics Research, 221*, 193-200.

Gilboy, W. B., Foster, J., & Folkard, M. (1982). A tomographic gamma-ray scanner for industrial applications. *Nuclear Instruments and Methods in Physics Research, 193*(1-2), 209-214.

Glasser, O. (1993). *Wilhelm Conrad Röntgen and the Early History of the Roentgen Rays.* Norman Publishing.

Gordon, R., Bender, R., & Herman, G. T. (1970). Algebraic Reconstruction Techniques (ART) for three-dimensional electron microscopy and X-ray photography. *29*, 471-481.

Guthrie, F. (1873). On a Relation between Heat and Static Electricity. *The London, Edinburgh and Dublin Philosophical Magazine and Journal of Science*, 257-265.

Harrison, M. (2014). *Geissler Tubes*. Retrieved from electricstuff: https://www.electricstuff.co.uk/geissler.html

Herman, G. T. (1979). Correction for beam hardening in computed. *Physics in Medicine & Biology, 24*(1), 81-106.

Hickson, P. (2015). *ASTR 530 Essential Astrophysics.* Retrieved from https://phas.ubc.ca/: https://phas.ubc.ca/~hickson/astr530/ASTR530_2015_ch8.pdf

Hiller, J., Masil, M., & Reindl, L. (2012). Physical characterization and performance evaluation of an x-ray micro-computed tomography system for dimensional metrology applications. *Measurement Science and Technology, 23*.

International Standard Orgnsitation. (2002). *ISO 15708-1:2017(E) Non-destructive testing — Radiation methods for computed tomography — Part 1: Terminology.* International Standard Orgnsitation.

J.J.Thomson. (1897). XL. Cathode Rays. *The London, Edinburgh and Dublin Philosophical Magazine and Journal of Science*, 293-316.

Janssens, E. (2018). *Advances in X-ray reconstruction algorithms for limited data problems in conventional and non-conventional projection geometries .* Antwerp: Universiteit Antwerpen.

Jiang, X., Scott, P. J., & Blunt, L. (2007). Paradigm shifts in surface metrology. Part II. The current shift. *Proceedings of the Royal Society, 463*, 2071-2099.

Jones, H. A. (1926). A Temperature Scale for Tungsten. *PHYSICAL REVIEW*, 202-207.

Kak, A., & Slaney, m. (1988). *Principles of Computerized Tomographic Imaging.* IEEE Press.

Kamphius, C., & Beekman, F. (1998). Accelerated iterative transmission CT reconstruction using an orderen subsets convex algorithm. *IEEE Transactions on Medical Imaging, 17*(6), 1101-1105.

Kastner, J., Harrer, B., Guillermo, R., & Oliber, B. (2010). A comparative study of high resolution cone beam X-ray tomography and synchrotron tomography applied to Fe- and Al-alloys. *NDT&E International, 43*, 599-605.

Kramar, U. (2017). *Encyclopedia of Spectroscopy and Spectrometry* (3 ed.).

Kruger, R., & Cannon, T. (1978). The application of computed tomography, boudnary detecation and shaded graphics reconstruction to industrial inspection. *Materials Evaluation*, 75-80.

Kruth, J. P., Bartscher, M., Carmignato, S., Schmitt, R., Chiffre, L. D., & Weckenmann, A. (2011). Computed tomography for dimensional metrology. *CIRP annals, 60*(2), 821-842.

Kumar, J., Attridge, A., Wood, P. K., & Williams, M. A. (2011). Analysis of the effect of cone-beam geometry and test object configuration on the measurement accuracy of a computed tomography scanner used for dimensional measurement. *Measurement Science and Technology, 22*.

Lange, K., & Carson, R. (1984). EM reconstruction algorithms for emission and transmission tomography. *Journal of comuputer assisted tyomogrpahy, 8*(2), 306-316.

Lawrence Livermore Labs. (1974). *Radiation gage imaging for non destructive testing applications.* Livermore: Lawrence Livermore Labs.

Letcher, T. M. (2007). *Thermodynamics, Solubility and Environmental Issues.* Durban: Elsevier Science.

Man, J., Keun, P., Dong, H., & Dong, Y. (2008). Design and analysis of a thermionic SEM column using 3D finite element analysis. *Physics Procedia*, 199-205.

matweb. (2022). *Tungsten, W*. Retrieved from matweb.com: https://www.matweb.com/search/datasheet_print.aspx?matguid=41e0851d2f3c417ba69ea0188fa570e3

Mayba, I., Gaiua, R., Kyle, R., & Shampo, M. (1997). Ukrainian Physicist Contributes to the Discovery of X-Rays. *MAYO CLINIC PROCEEDINGS*.

Meggit, G. (2008). *Taming The Rays.* Pitchpole Books.

Meroli, S. (2022). *The interaction of photons with the matter*. Retrieved from meroli.web: https://meroli.web.cern.ch/Lecture_photon_interaction.html

Microscopy Australia. (2014, June 12). *Characteristic X-rays*. Retrieved from myscope.training: https://myscope.training/legacy/analysis/eds/xraygeneration/characteristic/

Miroslaw, J., & Fournier, G. R. (2007). *Basic principles of the interaction of light with matter.* Academic Press.

Mitchell, K. W. (1989). A Generalized Approach to Wall Thickness Measurements in CT Images. *Topical Proc. Industrial Computerized Tomography, ASNT*, 120-124.

Mould, R. F. (2018). Alan Archibald Campbell-Swinton (1863–1930). *Journal of Oncology* , 46-49.

Muibbullah, M., & Ikuma, Y. (2019). Photoelectron ejection by electromagnetic wave. *Optik*, 802-809.

Munch, B., Trtik, P., Marone, F., & Stamanoni, M. (2009). Stripe and ring artifact removal with combined wavelet — Fourier filtering. *Optics Express*.

Murphy, A. (2020, 07 23). *K-absorption edge*. Retrieved from Radiopaedia.org: https://radiopaedia.org/articles/k-absorption-edge?lang=us

Nickoloff, E., & Berman, H. (1993). Factors Affecting X-ray Spectra. *Radiographics* , 1337-1348.

Nikon. (2022). *www.nikonmetrology.com*. Retrieved 02 14, 2022, from https://www.nikonmetrology.com/images/brochures/xt-h-series-en.pdf

Nikon. (n.d.). Filament Change Procedure Documentation.

NIKON METROLOGY. (2022). *www.nikonmetrology.com.* Retrieved from www.nikonmetrology.com: https://www.nikonmetrology.com/images/brochures/mct225-en.pdf

Nobel Prize Outreach. (2022). *www.nobelprize.org*. Retrieved 03 14, 2022, from https://www.nobelprize.org/prizes/medicine/1979/press-release/

Noel, A., & Thibault, F. (2004). Digital detectors for mammography: the technical challenges. *European Radiology, 14*.

Otha W. Linton. (1995). Medical applications of X-rays. *SLAC Beam Line*, 25-34.

Pagani, L., Townsend, A., Zeng, W., Lou, S., Blunt, L., Jiang, Z. Q., & Scott, P. J. (2019). Towards a new definition of areal surface texture parameters on freeform surface: Re-entrant features and functional parameters. *Measurment*, 442-459.

Paulus, D. (1980). Xeroradiography: an in-depth review. *Crit Rev Diagn Imaging, 12*, 309-384.

Pettersson, H., & Allison, D. (2001). *The Encyclopaedia of Medical Imaging.* Oslo: NICER Institute.

Plante, E. R., & Sessoms, A. B. (1973). Vapor Pressure and Heat of Sublimation of Tungsten. *Journal of Research of the National Institute of Standards and Technology*, 237-242.

Planter, E. R., & Sessoms, A. B. (1973). Vapor Pressure and Heat of Sublimation of Tungsten. *Journal of Research of the National Institute of Standards and Technology, 77*(2), 237-242.

Polischuk, B., Rougeot, H., Wong, K., Debrie, A., Poliquin, E., Hansroul, M., . . . Shukri, Z. (1999). Direct conversion detector for digital mammography. San Diego: Medical Imaging '99.

Preece, W. H. (1884). On a Peculiar Behaviour of Glow-Lamps When Raised to High Incandescence. *Proceedings of the Royal Society of London*, 219-230.

Probst, G., Hou, Q., Pauwels, R., Boeckmans, B., Xiao, Y., & Dewulf, W. (2019). Focal spot characterization of an industrial X-ray CT. Furth: German Society for Non-Destructive Testing.

Reimers, P., & Goebbels, J. (1983). New possibility of nondestructive evaluation by X-Ray computed tomography. *Materials Evaluation*, 732-737.

Reimers, P., Gilboy, W. B., & Goebbels, J. (1984). Recent develoments in industrial application of comupterised tomography with ionising radiation. *NDT international* , 197-207.

Rivers, M. (1998, May 14th). *Tutorial Introduction to X-ray Computed Microtomography Data Processing*. Retrieved from https://www.mcs.anl.gov/research/projects/X-ray-cmt/rivers/tutorial.html#Ring%20artifact%20reduction

Roentgen, W. C. (1896). ON A NEW KIND OF RAYS. *Science*, 227-231.

Russo, P. (2017). *Handbook of X-ray imaging: Physics and technology.* CRC Press.

Secades, C., O'Connor, B., Brown, C., & Walpole, M. (2014). *Earth Observation for Biodiversity Monitoring: A review of current approaches.* Montreal: Secretariat of the Convention on Biological Diversity.

Shepp, L. A., & Vardi, Y. (1982). Maximum Likelihood Reconstruction for Emission Tomography. *IEEE - Transactions on Medical Imaging, 1*(2), 113-122.

Sigl, C., & Quinn, R. (1980). *Radiography in Modern Industry.* Eastman Kodak Company.

Slocombe , J., Townsend, A., Addinall, K., & Blunt, L. (2019). The effects of x-ray computed tomography filament degradation on extracted areal surface texture data. *European Society for Precision Engineering and Nanotechnology, Conference Proceedings - 19th International Conference and Exhibition, EUSPEN 2019* (pp. 346-349). Bilbao: euspen.

Slocombe, J., & Blunt, L. (2022). The effects of manual XCT focusing on extracted surface texture data. *Surface Topography: Metrology and Properties*.

Smith, H., Bills , P., Addinall, K., & Blunt, L. (2021). 3D Imaging of Modified Firearms Using X-ray Computed Tomography (XCT).

Southall, L. A., Kagarice, K. J., Thron, A. M., Canepa, P. M., & Mackie, W. A. (2006). Thermal Expansion Characteristics of Hexaboride Electron Sources and Other Factors Impacting Beam Stability. *Microscopy and Microanalysis*, 1776-1776.

Speight, J. G. (2010). *Natural Water Remediation.* Butterworth-Heinemann.

Sprawls, P. (1995). *Blur, Resolution, and Visibility of Detail*. Retrieved from http://www.sprawls.org/ppmi2/BLUR/

Sprawls, P. (1995). *Physical Principles of Medical Imaging* (2 ed.). Medical Physics Pub Corp.

Sprawls, P. (n.d.). *X-Ray Tube Heating and Cooling*. Retrieved 03 22, 2022, from http://www.sprawls.org/ppmi2/XRAYHEAT/

Steffen , J. P., & Froeba, T. (2011). Reducing the Focal Spot Shift of Microfocus X-ray Tubes to Increase the Accuracy of CT-Based Dimensional Measurement. *International Symposium on Digital Industrial Radiology and Computed Tomography*, 20-22.

Summerhays, K., Baldwin, J., Campbell, D., & Henke, R. P. (2004). Application of Simulation Software to Coordinate Measurement Uncertainty Evaluation. *NCSLI Measure, 2*(4).

Sun, W., Brown, S. B., & Leach , R. K. (2012). *An overview of industrial X-ray computed tomography.* National Physical Laboratory.

Sun, W., Brown, S., & Leach, R. (2011). *An overview of industrial X-ray computed tomography.* National Physical Laboratory .

Sun, Z., Ng, C. K., & Reis, C. (2018). Synchrotron radiation computed tomography versus conventional computed tomography for assessment of four types of stent grafts used for endovascular treatment of thoracic and abdominal aortic aneurysms. *Quantative Imaging in Medicine and Surgery, 8*(6), 609-620.

Szwarc, R., Plante, E. R., & Diamond, J. J. (1965). Vapor Pressure and Heat of Sublimation of Tungsten. *Journal of Research of the National Institute of Standards and Technology*, 417-421.

Tawfik, A. S. (2021). *Development and optimisation of a method for assessment of porosity in additively manufactured parts using x-ray tomography.* University of Huddersfield.

ThermoFisher Scientific. (n.d.). *SEM Technology: A Comprehensive Guide.* ThermoFisher Scientific.

Thompson, A., Körner, L., Senin Nicola, Lawes, S., Maskery, I., & Leach, R. (2017). Measurement of internal surfaces of additively manufactured parts by X-ray computed tomography. *7th Conference on Industrial Computed Tomography.* Leuven.

Thompson, A., Lindau, I., Attwood, D., Liu, Y., Pianetta, E. G., Howells, M., . . . Winick, H. (2009). *X-ray Data Booklet.* Lawrence Berkeley National Laboratory.

Thompson, A., Senin, N., Maskery, I., Korner, L., Lawes, S., & Leach, R. (2018). Internal surface measurement of metal powder bed fusion. *Additive Manufacturing*, 126-133.

Townsend, A., Pagani, L., Scott, P., & Blunt, L. (2017). Areal surface texture data extraction from X-ray computed tomography reconstructions of metal additively manufactured parts. *Precision Engineering*, 254-264.

Townsend, A., Radu, R., Bills, P., & Blunt, L. (2017). Development of an interlaboratory comparison investigating the generation of areal surface texture data per ISO 25178 from XCT. *7th conference on industrial computed tomography*.

University of Oxford Department of Physics. (2022). *Cathode ray tube*. Retrieved from physics.ox.ac.uk: https://www2.physics.ox.ac.uk/accelerate/resources/demonstrations/cathode-ray-tube#:~:text=In%20the%20cathode%20ray%20tube,the%20path%20of%20the%20beam.

Van de Casteele, E., Van Dyck, D., Sijbers, J., & Raman, E. (2003). A model-based correction method for beam hardening artefacts in X-ray microtomography. *Journal of X-ray Science and Technology, 12*(1), 53-57.

Van Gomple, G., Van Slambrouck, K., Defrise, M., Batenburg, K. J., de Mey, J., Sijbers, J., & Nuyts, J. (2011). Iterative correction of beam hardening artifacts in CT. *Med Phys, 36*(1).

Vogeler, F., Verheecke, W., Voet, A., Kruth, J. P., & Dewulf, W. (2011). *Positional Stability of 2D X-ray Images for CT.* International Symposium on Digital Industrial Radiology and Computed Tomography.

Warren, A., Nylund, A., & Olefjord, I. (1996). Oxidation of tungsten and tungsten carbide in dry and humid atmospheres. *International Journal of Refractory Metals and Hard Materials*, 345-353.

Wells, J. (2009). On Continuing the Evolution of XCT Engineering Capabilities for Impact Damage Diagnostics. *Advances in Ceramic Armor III: Ceramic and Engineering Science Proceedings, 28*(5), 203-211.

Wells, J. M. (2007). QUANTITATIVE XCT EVALUATION OF POROSITY IN AN ALUMINUM ALLOY CASTING. Shape Casting: 2nd International Symposium .

Wevers, M. (2012). X-ray Computed Tomography for Non-Destructive Testing. *Non-Destructive Testing*, 13-29.

Yaffe, M., & Rowlands, J. (1997). X-ray detectors for digital radiography. *Physics in Medicine & Biology, 42*(1), 1-39.

Zhang, L., Gao, H., Li, S., Chen, Z., & Xing, Y. (2006). Cupping artifacts analysis and correction for a FPD-based cone-beam CT. *Electronic Imaging, 6065*.

8.2. Nomenclature of Surface parameters

Nomenclature (International Organization for Standardization, 2012)	
Parameter	Definition
AMPLITUDE PARAMETERS	
Sa	Arithmetic mean of the absolute of the ordinate values within a definition area
Sq(um)	Root mean square value of the ordinate values within a definition area
Ssk	Quotient of the mean cube value of the ordinate values and the cube of Sq within a definition area
Sku	Quotient of the mean quartic value of the ordinate values and the fourth power of Sq within a definition area (A)
Sp(um)	Largest peak height value within a definition area
Sv(um)	Minus the smallest pit height value within a definition area
Sz(um)	Sum of the maximum peak height value and the maximum pit height value within a definition area
SPACING PARAMETERS	
Str	Ratio of the horizontal distance of the f ACF(t x,t y) which has the fastest decay to a specified value s to the horizontal distance of the f ACF(t x,t y) which has the slowest decay to s, with $0 \leq s < 1$
Sal(mm)	Horizontal distance of the f ACF(t x,t y) which has the fastest decay to a specified value s, with $0 \leq s < 1$
HYBRID PARAMETERS	
Sdq	Root mean square of the surface gradient within the definition area (A) of a scale-limited surface
Sdr(%)	Ratio of the increment of the interfacial area of the scale-limited surface within the definition area (A) over the definition area
SK FAMILY	
Spk(um)	Average height of the protruding peaks above the core surface
Sk(um)	Distance between the highest and lowest level of the core surface